

学位論文

An improvement of a single-moment bulk
microphysics scheme for mesoscale
convective systems using a satellite simulator

(メソ対流システムを対象とした
人工衛星シミュレーターを利用した
シングルバルク雲微物理スキームの改良)

平成26年5月 博士（理学）申請

東京大学大学院理学系研究科

地球惑星科学専攻

盧 孟燮

Abstract

Clouds and precipitations in the tropics are important because of the energy budget of atmosphere and the amounts of precipitation to about two-thirds of the global precipitation. It is important to improve cloud statistics reproduced by numerical simulations due to lack of observations and also to uncertainties in retrieved physical parameters such as ice water content and effective radius. The purpose of this study is to improve the simulation of clouds and precipitation by a cloud system resolving model using the Tropical Rainfall Measuring Mission (TRMM) data with a satellite simulator. This study is the comprehensive evaluation of the model performance using a variety of dataset and the identification of an efficient method by a single-moment bulk scheme to improve it.

Deep convective systems over the tropical open ocean are evaluated based on the joint histogram of cloud-top temperature and precipitation echo-top heights, which were simulated by a nonhydrostatic model using a satellite simulator. The control experiment shows systematic discrepancies compared to the TRMM data, which are due to underestimation of stratiform precipitation and a higher frequency of precipitating deep clouds whose top height is higher than 12 km. Nevertheless, it shows good agreement with the data with regard to the horizontal distribution and statistical cloud size distributions of deep convective systems. The biases in the joint histogram can be improved by modifying the cloud microphysics parameters in the framework of a single-moment bulk microphysics scheme. Specifically, the effects of the size distribution of precipitating hydrometeors are examined in detail. It is found that the size distribution of precipitating hydrometeors improved the probability distributions of the joint histogram and contoured frequency by altitude diagrams (CFADs) of the convective precipitation clouds.

Simulations of global clouds and precipitations by a global cloud system resolving model

with a 3.5 km horizontal resolution are performed and evaluated using the TRMM and CloudSat data. The characteristics of vertical cloud structures among different regions are investigated. The simulation with the modified microphysics improves the joint histogram patterns related to stratiform precipitation. The cross-section of the tropical cyclone Fengshen is investigated. The regional differences of the joint histograms are examined over the tropics. It is found that the improved microphysics in the regional scale is capable to advance the results of global cloud simulations.

Additional evaluations are performed using 85-GHz microwave channel, OLR, and effective radius. We find small effects of the modified simulations on the cumulative probability distribution of polarization corrected 85-GHz brightness temperatures in mesoscale convective systems. The modified simulation generally improves the OLR but tends to underestimate the observation. The vertical structure of retrieved effective radius is improved from the other active sensor satellite data. However, the OLR and the simulated 85 GHz brightness temperatures remained to improve in this study.

In summary, the improvement of cloud/precipitation microphysics can successfully reproduce the OLR and accumulated precipitation over the tropical ocean. The improvement of microphysics in a regional scale model would be directly applicable to the analysis of cloud statistics based on TRMM and CloudSat. We believe the better performance of cloud statistic simulation would give more promising results for prediction of climate change and understanding of cloud and precipitation systems.

Acknowledgements

I am grateful to Prof. Masaki Satoh of the Atmosphere and Ocean Research Institute, the University of Tokyo for giving helpful advices, discussion, and continuous encouragements to whole of my researches, as a mentor throughout my graduate years. I appreciate the Prof. Nakajima for his kind encouragement and consideration. I appreciate Prof. Masunaga of the Nagoya University, who developed SDSU and discussed about a satellite simulator. I also appreciate Dr. Hashino for many instructive comments about microphysics and the analysis method. I would like to appreciate Dr. Matsui in NASA to invent T3EF methods. I have also received considerable support from Mr. Arakane, Mr. Ohno, Mr. Yamada, and Mr. Nishikawa in Satoh's lab. I got many helpful insights on bulk microphysics from Dr. Seiki. I learned good information of TTL and topical dynamics from Dr. Kubokawa.

Finally, I thank my wife Jin-young, for her love and, support, and for keeping me happy and healthy.

Contents

1. General introduction	1
1.1 Tropical mesoscale convective systems.	1
1.2 Cloud system resolving modeling	1
1.3 Microphysics.....	3
1.4 Evaluation of microphysics	6
1.5 The goal of this study	9
2 Evaluation of a stretched NICAM using a geostationary satellite and TRMM PR in the tropical open ocean	10
2.1 Introduction.....	10
2.2 Control experiments and evaluations	11
2.3 Modifications of microphysics scheme	20
2.4 Results of sensitivity experiments	29
2.5 Discussion and Conclusion.....	41
3 Analysis of a global simulation	45
3.1 Introduction.....	45
3.2 Experimental designs and data	46

3.3 Horizontal distributions of the TBB and accumulated precipitations	47
3.4 A case study of the tropical cyclone Fengshen	50
3.5 T3EF analysis of the global domain	53
3.6 Comparisons with CloudSat	64
3.7 Summary and conclusion.....	66
4 Remaining Issues	68
4.1 Introduction.....	68
4.2 Data.....	70
4.3 The cumulative probability distributions of PCT85	71
4.4 OLR	73
4.5 Evaluations of effective radius	75
4.6 Summary and conclusion.....	77
5 General conclusion	78

1. General introduction

1.1 Tropical mesoscale convective systems

Tropical precipitation systems make important contributions to the global energy budget and play a key role in climate and weather modeling. Mesoscale convective systems (MCS) are one of big sources of the tropical precipitation systems, and defined as forms of a cumulonimbus cloud system that produces a contiguous precipitation area ~ 100 km or more at least in one direction (Houze 1994). MCSs have convective and stratiform precipitation region generally distinguished by radar echoes. It is known that MCSs give a connection between atmospheric convection and the larger-scale atmospheric circulation. They occur in the condition associated with larger-scale wave motions (e.g., Houze et al. 2000; Carbone et al. 2002).

The large scale numerical simulations are needed for understanding MCSs. Although representations of MCSs by high-resolution nonhydrostatic models such as cloud-system-resolving models (CSRMs) without cumulus parameterization have successfully reproduced realistic structures of cloud systems associated with precipitation.

1.2 Cloud system resolving models

CSRMs are generally defined to be models with horizontal grid spacing low enough to be able to explicitly simulate individual clouds and cloud systems, CSRMs could represent more sophisticated and realistic cloud microphysical processes, and they can resolve the time evolution, structure, and life cycles of cloud and cloud systems. The suitable horizontal resolutions for cloud resolving modeling have been argued because of various cloud systems and turbulence aspects. The typical range of horizontal grid spacing considered to be 4 km or less to reproduce mesoscale convective system without the cumulus parameterization (Cheng

and Cotton 2004; Guichard et al. 2004).

In recent years, increasing computer speed and resource has expended CSRMs's integration time and horizontal domain size, and it is possible to be the next generation climate and global circulation model to reproduce multi-scale interactions of cloud and precipitation systems. The aqua planet experiments using a global cloud system resolving model (GCSRMs) reproduce the multi scale convective structure and the diurnal cycle of convective precipitation without cumulus parameterization (Tomita et al. 2005). The Miura et al. (2007) succeeded to reproduce a realistic Madden-Julian Oscillation event such as large scale cloud organizations and their eastward propagation using a GCSRMs.

A GCSRMs reproduces a realistic behavior of the three dimensional cloud distributions. Inoue et al. (2008) analyzed cloud horizontal size distributions of cloud clusters using a geostationary satellite and they found high resolution experiment shows the closer cloud size distribution than a coarse resolution experiment. Ham et al. (2013) analyzed vertical profiles of precipitating and non-precipitating clouds using the CloudSat and CALIPSO data and showed the similar vertical patterns in a 3.5 km GCSRMs simulation.

The cloud microphysics plays important roles on the distribution of clouds and precipitations in CSRMs. Satoh and Matsuda (2009) investigated statistics on high clouds depending on various resolutions and microphysical parameters under an idealized radiative convective equilibrium condition. Kodama et al. (2012) showed the sensitivities of high thin cirrus and higher cloud top, and found high clouds were very sensitive to the microphysical parameters. Iga et al. (2011) found that the upper cloud coverage changed by the sensitivity test using various physical parameters, and high clouds affected the total precipitation and the intensity of the Hadley circulation.

1.3 Microphysics

The microphysics schemes have been developed and used in two different methods to express size distributions: “bulk” schemes and “bin” schemes. The bulk microphysics schemes represent the hydrometeor size for each class with a distribution function, such as an exponential function or a gamma type. The bin microphysics schemes could represent the actual size spectra of CCN as well as different hydrometeor particles where the size distribution consists of many bins of a mass or number concentration. The first version of bin schemes was developed with only water phase microphysics in relatively simple dynamics (e.g., Clark 1973; Soong 1974; Takahashi 1975). And several bin schemes have been developed with both water and ice phase microphysics (e.g., Lynn et al. 2005; Hashino and Tripoli, 2007; Iguchi et al. 2008; Khain and Lynn 2009; Suzuki et al. 2010). Bin microphysics schemes have been used to study detailed dynamics and microphysics interactions, such as aerosol indirect effects (e.g., Khain et al. 2005; Tao et al. 2007). However, bin schemes required more computational resources for calculations, so they have been used mainly for idealized or small-domain experiments instead of realistic configurations. Bulk microphysics schemes have been used to simulate precipitation systems for practical applications.

A bulk microphysics is divided into the single moment and double moment scheme. The single-moment schemes that calculate only the mass concentrations of hydrometeors (e.g., Lin et al. 1983; Rutledge and Hobbs 1983) have been widely used for large-scale experiments and long-term CSRM simulations because they are simple and computationally efficient.

The ice phase microphysics is one of issues in improvements of a single moment microphysics. Hong et al. (2004) introduced the revised approaches of microphysical processes such as ice nucleation, ice deposition process, the snow size distribution based on Houze et al. (1979) and so on. They tested the revised microphysics in an idealized thunderstorm simulation and found the distribution of simulated clouds and precipitation was sensitive to the assumption of microphysical processes. Thompson et al. (2008) implemented the snow size parameterization based on Field et al. (2005) and employed changes of many

microphysical processes based on the bin scheme. Lin and Colle (2011) introduced the effect of partially rimed particles using a diagnostic riming intensity, and the mass dimension relationship, velocity diameter relationship.

Double-moment schemes prognostically calculate both the mass concentrations and number concentrations of hydrometeors (Morrison et al. 2005; Seifert and Beheng 2006; Lim and Hong 2010; Seiki and Nakajima 2013). The double-moment approach for the bulk microphysics scheme, which allows more flexibility of the size distribution enabling the mean diameter to evolve in contrast to the single-moment approach, has become a promising method to improve the microphysical processes in the mesoscale modeling area; even though it requires more computational time than the single-moment approach. Double-moment schemes predict changes in the number concentration of hydrometeors and enable explicit calculation of nucleation processes related to indirect aerosol effects and potentially more consistent treatment of the radiation effects of cloud particles (Seiki et al. 2014). Double-moment schemes are known to exhibit different characteristics in comparison with single-moment bulk microphysics schemes; a widespread trailing, stratiform precipitation region, and different rain evaporation rates are obtained by using a double-moment scheme in idealized cases (Morrison et al. 2009).

However, there are enough uncertainties and nonlinearities that more sophisticated schemes do not always perform better than simpler single moment bulk schemes (Wang et al. 2009; Varble et al. 2011). Besides the extra degrees of freedom that are required to behave in a realistic manner, larger errors in a more dominant process can overwhelm potential gains elsewhere. For examples, Van Weverberg et al. (2013) evaluated MCS simulations using three different bulk microphysics schemes over the tropical western Pacific and found that the performances of complex two-moment schemes were not superior to the simpler single-moment schemes.

Some evaluation studies found excessively high radiative scattering properties such as radar reflectivities in the upper troposphere of CRM simulations with excessive amounts or sizes of precipitating ice hydrometeors produced by a single moment microphysics (Lang et

al. 2007; Blossey et al. 2007; Zhou et al. 2007; Li et al. 2008; Matsui et al. 2009). The problem is associated with graupel (Lang et al. 2007; Li et al. 2008; Matsui et al. 2009) and snow (Masunaga et al. 2008; Ham et al. 2013). Varble et al. (2011) noted radar reflectivity overestimated. Graupel is the cause in single moment microphysics schemes whereas snow is the cause in double moment microphysics schemes for excessively high reflectivities. Lang et al. (2007, 2011) reduced the biases of the single-moment bulk scheme for simulated radar reflectivities by improving the microphysical process and the size distributions of graupel and snow. Even though there are some previous studies of improvement in microphysics, there are enough inherent biases of cloud and precipitations that microphysics schemes in general require and continue to undergo refinement.

Effects of the microphysics on the storm dynamics are found by several studies (Cohen and McCaul 2006; van den Heever and Cotton 2004; van Weverberg et al. 2011). Van Weverberg et al. (2011) found that the rainfall was spread over a larger area, and stronger near surface downdrafts and enhanced low level cooling occurred when the size of hail stones was decreased.

The microphysics schemes have been developed to represent the realistic cloud physical process and cloud properties. Several evaluation studies showed single moment microphysics schemes had better performances to reproduce the ice phase clouds than other more comprehensive schemes. In this study, a single bulk microphysics scheme is evaluated using the cloud statistics in the point of satellite's view.

1.4 Evaluation of microphysics with the satellite data

Many efforts toward evaluation and improvement of microphysics schemes based on in-situ aircraft observation data and ground radar observations have been made (e.g., Milbrandt et al. 2008; Hong et al. 2010; Molthan et al. 2010). However, ground radar observations and aircraft data have spatial and sampling limitations.

The satellite data could detect the cloud and precipitation properties from radiance measurements. The satellite data records are now long enough to analyze meaningful climatologies of cloud and precipitation properties. The satellite sensors are divided into passive and active sensor. Passive sensors measure radiances that are the end product of the integrated effects of electromagnetic absorption–emission and scattering through the precipitating cloud along the sensor view path. The electromagnetic properties of cloud and precipitation particles depend on the frequency of the passive radiometers. On the other hand, active sensors (e.g. radars) provide specific height information based upon the time delay of the backscattered return power. The active sensor could detect the vertical distribution of clouds and precipitations.

The Tropical Rainfall Measuring Mission (TRMM) satellite has operated continuously for over a decade, providing numerous, valuable observations of precipitating tropical cloud systems from its sensors: the Visible/Infrared Scanner (VIRS), the TRMM Microwave Imager (TMI), and the Precipitation Radar (PR; Kummerow et al. 1998). The combination of satellite-borne passive and active sensors to be deployed in the upcoming TRMM promises to provide critical information regarding the three dimensional distributions of precipitation and heating in the Tropics (Simpson et al. 1996). The VIRS on TRMM adds cloud-top temperatures and structures to complement the description of the two microwave sensors. While direct precipitation information from VIRS is less reliable than that obtained by the microwave sensors, VIRS serves an important role as a bridge between the high quality but infrequent observations from TMI and PR with the more available data and longer time series data available from the geostationary VIS/IR satellite platforms.

The TRMM data is useful to evaluate the microphysics in precipitating clouds. Zhou et al. (2007) compared simulated cloud and rain systems such as the surface rain rate, convective/stratiform percentage, rain profiles, cloud properties, and precipitation efficiency using TRMM data. They found the simulation with a single moment scheme showed more compact areas of intense convection and less anvil cloud, which was consistent with a smaller total cloud fraction and larger domain-averaged outgoing long wave radiation. Eitzen and Xu (2005) evaluated simulations of two different microphysics using the probability density functions of several observed and retrieved fields from the CERES SSF data product. They found the improved microphysics scheme produced more realistic distributions of albedo, outgoing longwave radiation, cloud top temperature, and cloud height than the control simulations.

The CALIPSO (Cloud-Aerosol Lidar and Infrared Pathfinder Satellite Observation) (Winker et al. 2003) and CloudSat (Stephens et al. 2002) satellites data are available to analyze the vertical structure of clouds. TRMM has quantified how much precipitating particles falls in the tropical atmosphere and it is insensitive to water and ice clouds. CloudSat employed the millimeter wavelength radar to observe vertical profiles of most of the cloud condensate and precipitation within its nadir field of view. The CALIPSO lidar is sensitive to subvisible cirrus clouds.

The CALIPSO and CloudSat data have narrow field of view. Many studies have been carried out in order to compare cloud properties with global atmospheric models than regional models. CALIPSO (Chepfer et al. 2008, 2010), CloudSat (Bodas-Salcedo et al. 2008; Li et al. 2008; Masunaga et al. 2008), and both CALIPSO and CloudSat (Satoh et al. 2010; Inoue et al. 2010; Zhang et al. 2010; Kodama et al. 2012; Hashino et al. 2013) are used to evaluate vertical structure of clouds and the horizontal distribution of high clouds in global models. Masunaga et al. (2008) found a GCRM CFADs qualitatively reproduces TRMM and CloudSat CFADs, except that the GCRM tends to overly produce snow in deep convection. Satoh et al. (2010) evaluated the CFADs of CALIPSO and CloudSat. And they found the cloud microphysics scheme with a graupel category improved the bias of CFADs.

There are two approaches to evaluate CSRMs using satellite data for the spatial and vertical distributions of cloud systems. One is to directly compare the output data of CSRMs and retrieve physical parameters from satellite data, and the other is to compare the radiances in satellite data and the simulated radiances from CSRMs output data using satellite simulators (e.g. Masunaga et al. 2010; Bodas-Salcedo et al. 2011; Hashino et al. 2013). The latter cases are more consistent because we can establish the same microphysical assumptions about hydrometeors, such as their size distributions and density, in the model and the simulators.

Discrepancies between observations and numerical simulations generally arise from both dynamical and physical processes. In this study, we focus on the microphysics, especially on the size distributions in single-moment bulk microphysics. Microphysical size distributions are not only related to microphysical processes such as collection and deposition/evaporations, but also have impacts on cloud properties and hence radiative transfer, latent heating and surface precipitation (Li et al. 2008; Luo et al. 2010; Varble et al. 2011). Several studies and sensitivity tests of precipitation systems have been made using a single-moment microphysics scheme (Gilmore et al. 2004; Satoh and Matsuda 2009; Van Weverberg et al. 2011; Lang et al. 2011). We investigate and evaluate the parameterization in comparison with satellite observation data from TRMM. We investigate the effects on the simulated radiances by changing the size distribution assumptions and mass–diameter (M – D) relationship.

1.5 The goal of this study

The most of studies about evaluations with satellite data is comparison with different microphysics (Masunaga et al. 2008, 2010; Matsui et al. 2009; Lang et al. 2011; Varble et al. 2011). The different microphysics schemes have their own assumptions of size distribution and physical processes, and it is hard to interpret the results. It is important to interpret the results, why the results are better than previous results. There are a few researches about the effects of the size distribution of hydrometers in point of satellite view about in MCSs over the tropics. In this study, the effects of size distribution in microphysics are examined on the horizontal and vertical properties of clouds and precipitation with a regional CSRM. The microphysics schemes are evaluated and improved based on the sensitivity tests using satellite data with a satellite simulator.

The cloud properties such as horizontal cloud size distributions and precipitation cloud statistics are evaluated and improved over the tropical ocean using a regional CSRM in chapter 2. Changes of other physical results such as precipitation, OLR and dynamics are investigated through sensitivities to microphysics schemes. The improved microphysics with a regional model is examined for a global CSRM with a several km horizontal mesh in chapter 3. The remaining issues are discussed about the microwave data, retrieved effective radius, and OLR data in chapter 4.

2 Evaluation of a stretched NICAM using a geostationary satellite and TRMM PR in the tropical open ocean

W. Roh and M. Satoh

(Published in *Journal of the Atmospheric Sciences*, doi:10.1175/JAS-D-13-0252.1)

© American Meteorological Society. Used with permission.

2.1 Introduction

There are several studies about the role of microphysics parameterizations in tropical convective systems. Powell et al. (2012) evaluated properties of the continental tropical anvil clouds using six different microphysics schemes: Goddard (Tao et al. 1989; Lang et al. 2007); SBU-YLIN (Lin and Colle 2011); WDM6 (Lim and Hong 2010); Thompson (Thompson et al. 2008); Morrison (Morrison et al. 2009); Milbrandt (Milbrandt and Yau 2005). Caine et al. (2013) compared results of numerical simulations to radar observations using two different microphysics schemes: Purdue-Lin (Lin et al. 1983; Rutledge and Hobbs 1984); Thompson (Thompson et al. 2008) by a cell-tracking algorithm, and found overestimation of storm heights of convective systems over the tropical ocean. Single bulk microphysics results correspond to previous studies like less anvil clouds related to larger domain averaged outgoing longwave radiation (OLR) (Blossey et al. 2007; Zhou et al. 2007), and overestimation of radar reflectivity (Li et al. 2008; Varble et al. 2011). These studies focused on the comparisons and evaluations using different microphysics schemes. Since different microphysics schemes are based on different approaches of microphysical processes and size distribution assumptions, it is difficult to interpret why the results are better in general. In this study, we focus effects of the size distribution parameterizations of precipitating hydrometeors on the joint histograms and CFADs of TRMM. We investigate how the results are improved using more realistic size distributions of microphysics.

In this chapter, we focus on mesoscale convective systems over the tropical central Pacific ocean region and evaluate numerical simulations with a satellite simulator. We investigate the

horizontal distribution of cloud sizes, the joint probability distributions of cloud-top temperature, precipitation-top height (PTH), and CFADs for each category using the TRMM precipitation radar (PR) and infrared scanner following the approach proposed by Masunaga and Kummerow (2006) and Matsui et al. (2009).

In section 2.2, the experimental design and observational data used in this study are described, and a result from the control experiment are introduced and evaluated. The original microphysics scheme used in section 2.2 is the Lin-type scheme (Lin et al. 1983) with modification by Tomita (2008). A simple size distribution with constant intercept parameters N_0 are used. First, after analyzing the horizontal distributions of cloud systems using the probability distribution of cloud sizes (Inoue et al. 2008), we apply the TRMM Triple-Sensor Three-Step Evaluation Framework (T3EF) method (Masunaga et al. 2008; Matsui et al. 2010) to evaluate the vertical distributions of hydrometeors to show a clear bias of the original scheme. In section 2.3, we propose several modifications in the size distributions of hydrometeors to improve the results in section 2.2. In section 2.4, the results of sensitivity tests using the modification proposed in section 2.3 are presented. Discussion and conclusions are given in section 2.5.

2.2 Control experiments and evaluations

2.2.1 Experimental design

We use the stretched version of the Nonhydrostatic Icosahedral Atmospheric Model (NICAM: Tomita and Satoh 2004; Satoh et al. 2008) to simulate mesoscale convective systems on the tropical central Pacific. NICAM is a global nonhydrostatic model and can also be used as a regional model by transforming the horizontal grid system so as to focus on a region of interest (the stretched NICAM: Tomita 2008b). Because the same dynamics and physics schemes are used in the global NICAM and the stretched NICAM, any improvements tested in the stretched NICAM can be directly applied to the global NICAM. This approach is proposed by Satoh et al. (2010), and we employ this methodology to use the stretched NICAM to obtain improved simulations over the global domain with high resolution. The

target area of this study is over the tropical open ocean in the central Pacific. The central point of the target area is at longitude 180E on the equator, and the analysis domain is between latitudes 10S and 10N and longitudes 170E and 170W. The minimum horizontal grid size is 2.4 km near the central point. The average grid size of the analysis domain is about 3.3 km and most of grid size is under 5 km. We used the National Centers for Environmental Prediction Global Data Assimilation System analysis data for the initial data and the boundary condition of the sea surface temperature (NCEP 2000). The sea surface temperature is fixed during the integration. The microphysics scheme in this study is the six-water-categories single-moment bulk scheme including vapor, cloud water, rain, cloud ice, snow, and graupel as hydrometeors (NSW6: Tomita 2008a), which is based on the scheme of Lin et al. (1983). The vertical grid number is 40, and it covers from the surface to 40 km; the vertical resolutions become coarser toward the upper levels. The integration time starts at 00 UTC 1 January and terminates at 00 UTC 1 February 2007. The actual analysis was made for the period of from 06 UTC 1 January to 00 UTC 1 February; thus, the 6 h before this analysis can be regarded as the time for the spin-up process. We use about one month's data to obtain more statistical results for mesoscale convective systems for the control experiment (Section 2c). We simply perform a free run without nudging and do not apply the boundary conditions from realistic observations. We obtain mesoscale convective systems in the target area throughout the simulation. Synoptic-scale waves and intraseasonal oscillations are also realistically reproduced in the simulation even after a few days, similarly to Miura et al. (2007). As shown later (Section 5), sensitivity experiments will be performed for the first seven days of the integration. The output data are interpolated to 0.0315° (~ 3.5 km) for comparison with the observation data at the same horizontal grid spacing.

In NSW6, the size distributions of precipitating hydrometeors are represented by the simple negative exponential distributions relation

$$n_{[r,s,g]}(D) = N_{0[r,s,g]}\exp(-\lambda_{[r,s,g]}D), \quad (2.1)$$

where $n(D)$ is the number concentration per unit volume per unit size range, N_0 is an

intercept parameter, D is the diameter, and λ is a slope parameter. The subscripts r, s, and g denote rain, snow, and graupel, respectively. N_0 is constant in NSW6. The number-concentration-weighted mean diameter (the inverse of λ in the exponential distribution, hereafter mean diameter) is a function of the mass concentration of hydrometeors for a fixed N_0 . The mass–diameter relationship for a spherical shape is given by

$$m(D) \text{ (kg)} = \frac{\pi \rho_{[r,s,g]}}{6} D^3, \quad (2.2)$$

where m is the mass of particles per unit volume per unit size range, and $\rho_{[r,s,g]}$ is the hydrometeor density. The slope parameter is expressed as

$$\lambda_{[r,s,g]} = \left(\frac{\pi \rho_{[r,s,g]} N_{0[r,s,g]}}{\rho_{air} q_{[r,s,g]}} \right)^{0.25}, \quad (2.3)$$

where $q_{[r,s,g]}$ is the hydrometeor mass concentration, and ρ_{air} is the air density.

2.2.2 Observational data and satellite forward operators

The infrared equivalent blackbody temperature (TBB) of the MTSAT geostationary satellite from the 11 μm infrared channels with 0.04° resolution are used to investigate the cloud-top temperature and the horizontal distribution of cloud systems (Global-IR: Janowiak et al. 2001). The infrared 11 μm TBB from the TRMM 1B01 product and the 13.8 GHz reflectivity and orbital precipitation from TRMM 2A25 are used for the T3EF method. T3EF has three steps: obtaining the joint histograms of TBB and PTH, the CFADs of the PR reflectivities, and the cumulative probability distribution of the TRMM Microwave Imager (TMI) 85 GHz brightness temperatures (Masunaga and Kummerow 2006; Matsui et al. 2009). The PTH is identified as the highest altitude of the layer above 17 dBZ of PR reflectivity. The TBB on the PR instantaneous field of view is used, and every data point is interpolated to 0.0315° (~ 3.5 km) of horizontal spacing for comparison with the NICAM data.

We use the Satellite Data Simulator Unit (SDSU; Masunaga et al. 2010), version 2.1.4, to compare the radiances of the observation data with those of the NICAM data. In SDSU, the extinction and scattering properties of hydrometeors are calculated based on the Mie theory.

These radiative properties are used for calculation of satellite radiances by microwave, radar, and Vis/IR simulators. Especially, snow and graupel are assumed as a soft mixture of air and ice by Maxwell Garnet approach (Maxwell-Garnett 1904) which was generalized by Bohren and Battan (1982) . The effective dielectric constant of the solid precipitating hydrometer is like

$$\epsilon_{[s,g]} = \frac{(1 - f)\epsilon_{ice} + f\gamma\epsilon_{air}}{1 - f + f\gamma}, \quad (2.4)$$

$$\gamma = \left(\frac{2\epsilon_{ice}}{\epsilon_{air} - \epsilon_{ice}} \right) \left[\left(\frac{\epsilon_{air}}{\epsilon_{air} - \epsilon_{ice}} \right) \ln \left(\frac{\epsilon_{air}}{\epsilon_{ice}} \right) - 1 \right], \quad (2.5)$$

$$f = 1 - \frac{\rho_{[s,g]}}{\rho_{ice}}, \quad (2.6)$$

where $\epsilon_{[s,g]}$, ϵ_{ice} , and ϵ_{air} is the complex dielectric constant of the hydrometer, pure ice, and air. f is volume fraction of ice and air.

We use the same assumed size distributions for rain, snow, and graupel in NICAM and the SDSU. For cloud water and cloud ice, we use the size distributions used in the SDSU because NSW6 has no assumption about the size distributions of cloud ice and cloud water; that is, we set 30 μm as the effective radius of cloud ice and a log normal distribution of cloud water (the median diameter is 20 μm and the dispersion is 0.35) in the radar simulator and the visible/infrared channel simulator of the SDSU.

2.2.3 Results of the control experiment

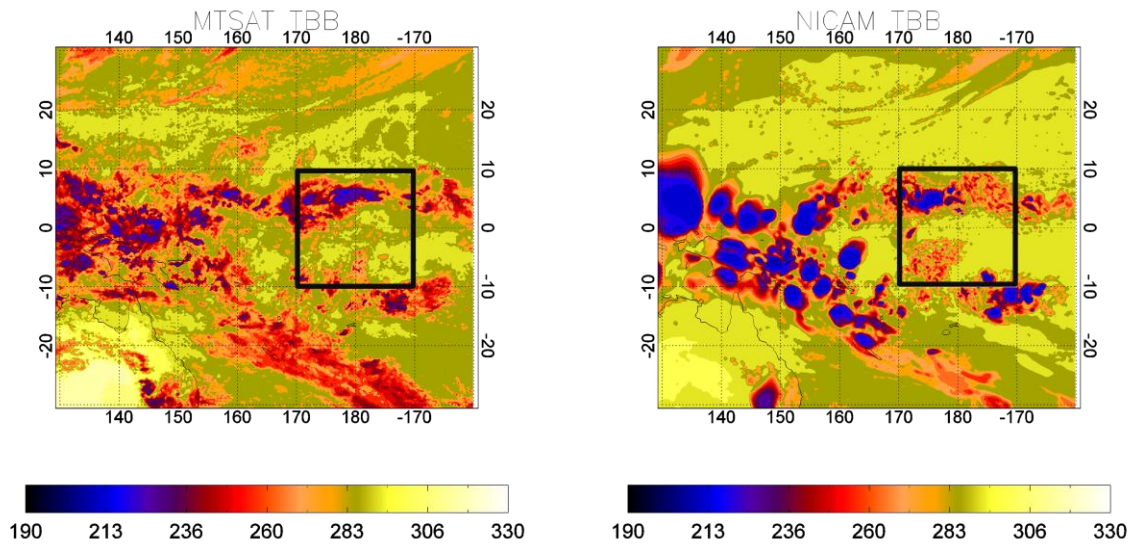


Fig. 2.1: Comparison of horizontal distribution of TBB from MTSAT (left) and the control experiment by NICAM (right) at 6 UTC 2 January 2007. Black box is the analysis domain.

Figure 2.1 shows the horizontal distribution of TBB observed by MTSAT and simulated by the stretched NICAM over 30S–30N and 130E–160W at 6 UTC 2 January 2007. Two convective bands over the analysis domain (enclosed by the rectangle in Fig. 2.1) are reproduced well at almost the same location as in MTSAT. One convective system is in the northern hemisphere about 5N latitude, and the other is in the relatively cloud-populated areas in the southwestern domain (5S–10S, 170E–180E). In the region outside the rectangle, the horizontal resolutions are coarser than that of the analysis domain, so the simulated TBB is lower than the observations. The cloud sizes of convective systems seem to be overestimated in the area of coarse resolution, but we do not use the coarser resolution region for the analysis.

First, to show the statistical behaviors of clouds in the analysis domain, we analyze the size distributions of the upper clouds using the two threshold values of the TBB, 208 K and 253 K, following Inoue et al. (2008). We calculated the 11 μm TBB from vertical profiles of the

NICAM simulation snapshot data using the infrared satellite simulator embedded in the SDSU and directly compared the observed and simulated 11 μm TBBs. This is in contrast to the work of Inoue et al. (2008), who compared the observed TBB and the OLR of the NICAM simulations using their respective threshold values. Figure 2.2a shows that the simulated cold clouds having a threshold of 253 K are similar to those of the observation. The cloud size probability distribution of the deep convective core (208 K) shows that the simulation has larger convective core fraction than the observation (Fig. 2.2b). These results are compatible with those of the global NICAM with a 3.5 km horizontal mesh shown by Inoue et al. (2008).

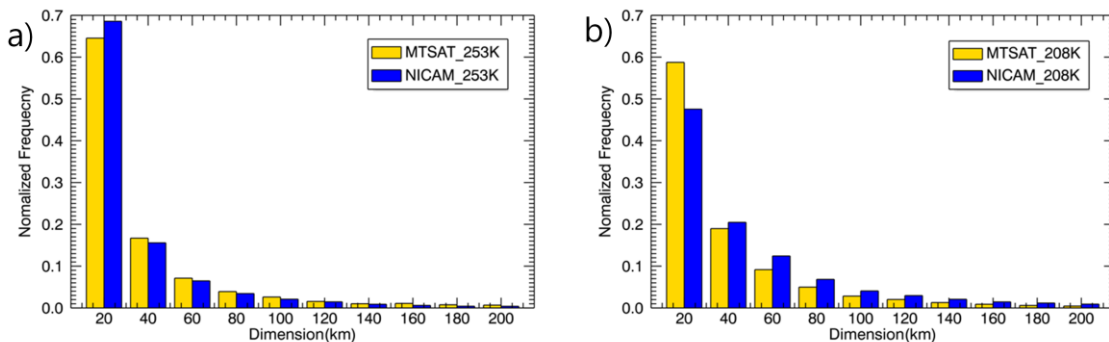


Fig. 2.2: Histogram of cloud size of TBB defined by the threshold values of 208 K (a) and 253 K (b). Size on abscissa is defined as the square root of the area.

Next, we analyze the vertical properties of precipitating clouds using the T3EF method. In this study, we focus on the joint histograms and CFADs. Matsui et al. (2009) classified cloud types into four categories according to the domain within the joint histogram: shallow, congestus, mid-cold, and deep clouds (Table 2.1). Because the different cloud types have different dynamical processes and environmental conditions, it is important to evaluate the quantitative properties of clouds by classifying them into different types. This type of classification method is advantageous in comparison of observations and CSRMs output.

Table 2.1. Categorization of cloud types based on the T3EF method of Matsui et al. (2009).

	Shallow	Congestus	Mid-cold	Deep
TBB	Above 260 K	Above 245 K	Under 245 K	Under 245 K
PTH	Under 4 km	Between 4 and 7 km	Between 4 and 7 km	Above 7 km

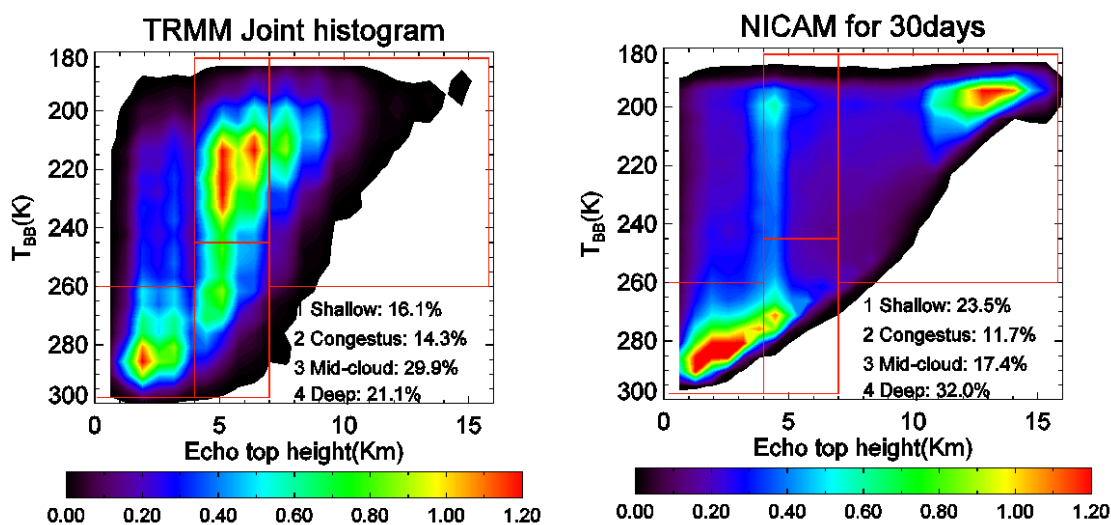


Fig. 2.3: Joint histograms of PTH and TBB from TRMM (left) and the control experiment (right) for 30 days on January 2007. The unit of the color bar is $\% \text{ km}^{-1} \text{ K}^{-1}$.

Figure 2.3 shows the joint TBB and PTH histograms from both the simulation and the TRMM observation. Following Masunaga and Kummerow (2006) and Matsui et al. (2009), we use the joint TBB and PTH histograms to classify the cloud types into the four categories given above. In this study, the simulation is targeted on the region of active deep clouds in the tropics, and the populations of deep and mid-cold clouds are higher; this characteristic is similar to the KWAJEX case shown by Matsui et al. (2009; their Fig. 2a). For the observation, the percentages of each cloud type are 16.1 %, 14.3 %, 29.9 %, and 21.1 % for shallow, congestus, mid-cold, and deep clouds, respectively. In this case, the mid-cold clouds are the

most populated category, and deep clouds are the second. Deep clouds represent both mesoscale deep convective systems and stratiform clouds. The mid-cold clouds are related mainly to the stratiform precipitation systems, and cirrus partially overlapped congestus according to the TRMM PR convective–stratiform classification data.

For the simulation shown in the right panel of Fig. 2.3, the percentages of each cloud type are 23.5 %, 11.7 %, 17.4 %, and 32.0 % for shallow, congestus, mid-cold, and deep clouds, respectively. It is clear that the simulation produces too many deep clouds and does not represent sufficient stratiform clouds (mid-cold). This cannot be inferred from the upper cloud size statistics shown in Fig. 2.2, so we need to analyze the vertical structures of the clouds in more detail using the T3EF method as adopted here. The shallow precipitation is overestimated in comparison with the observation. This means that the control result underestimates stratiform precipitation systems compared with convective precipitation systems.

Figure 2.3 shows a clear discrepancy in the simulation, that is, high frequencies of PTH near 14 km and low frequencies of PTH between 5 and 10 km. Three discrete distributions appear in the joint histogram of the numerical results at low, medium, and high PTH. From switching off the contribution of each category of hydrometeors in the SDSU, we found that the heavier population near 14 km in PTH is related to the radar reflectivities of the snow category (not shown). The radar reflectivity is calculated from the hydrometeor content and the size distribution assumption in the single-moment bulk microphysics. Thus, one possible reason is overestimation of the mass concentration of snow, and the other is excessively large snow particles over the upper part of the troposphere. We speculate that these discrepancies arise from the incorrect size distributions of precipitating hydrometeors; two hypotheses will be further investigated in the next section.

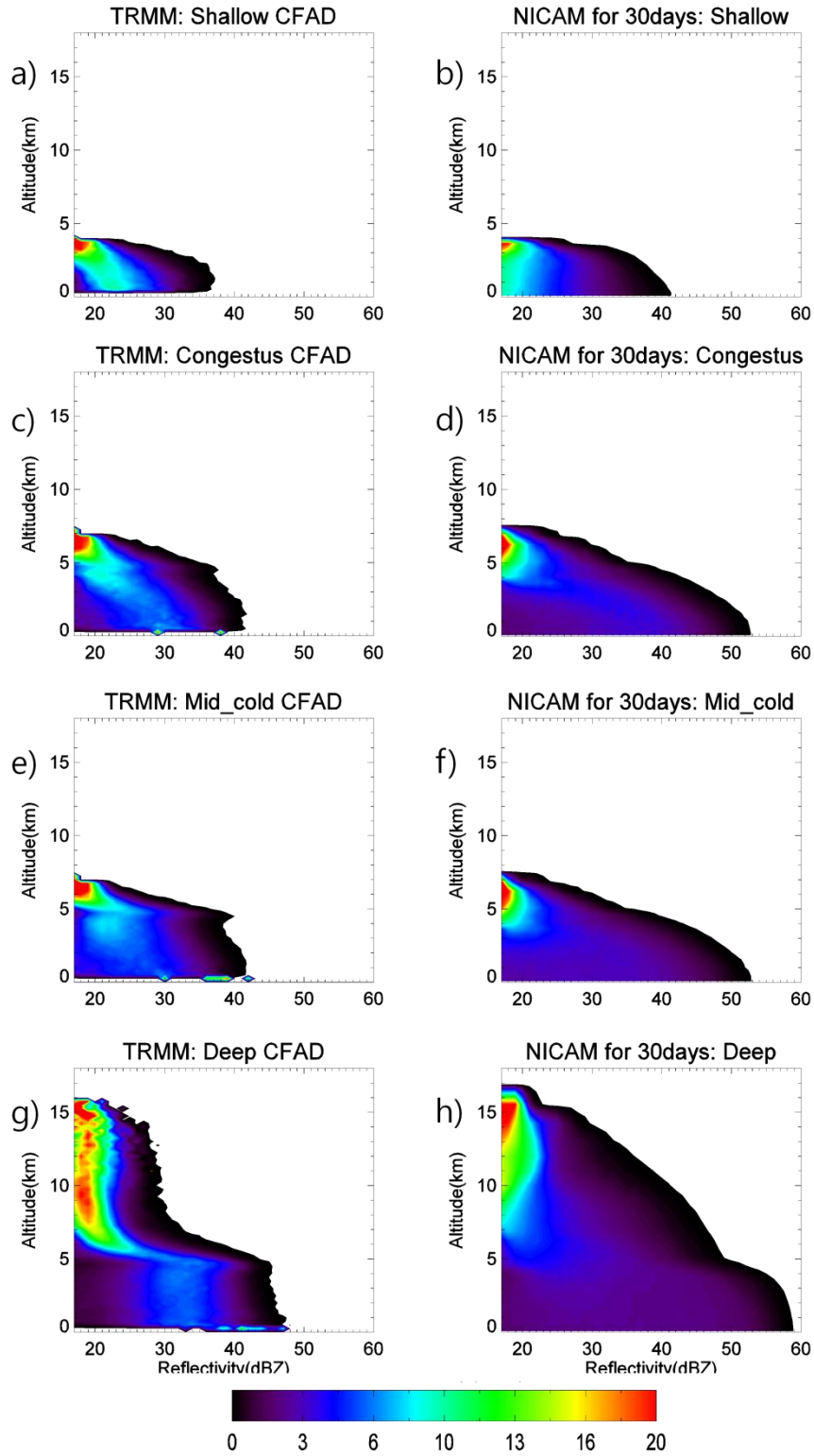


Fig. 2.4: CFADs for cloud categories of shallow (a, b), congestus (c, d), mid-cold (e, f), and deep clouds (g, h) for TRMM observation (left) and control experiment (right). The unit of the color bar is $\% \text{ km}^{-1} \text{ dBZ}^{-1}$.

Figure 2.4 shows the CFADs of radar reflectivities of the four cloud types in the T3EF for 30 days in the tropical central Pacific. In the shallow and congestus clouds, the observed average reflectivity in CFADs increases from upper altitudes to the surface, and the reflectivity is broadly distributed down to the surface (Figs. 2.4a, c). The CFADs of the simulated congestus and mid-cold clouds are somewhat similar to those of the observed clouds (Figs. 2.4c, d, e, f), although they show overestimation of radar reflectivity below 5 km altitude. The modal radar reflectivity in the simulated shallow precipitation does not increase to the surface and is slightly underestimated compared to the observation (Fig. 2.4b). The simulated congestus precipitation is similar to the observed pattern, and the average radar reflectivity in the CFADs increases (Fig. 2.4d). The mid-cold clouds have a clear bright band near the melting layer (5 km), where the radar reflectivity increases slightly in the observation (Fig. 2.4e). However, the simulation does not have a clear signal near the melting layer (Fig. 2.4f), so the bright band option of the SDSU is not used in this simulation. The CFADs of deep clouds from 10 km to 15 km appear similar in the observation and the simulation (Figs. 2.4g, h); however, they differ from the surface to 10 km, and the radar reflectivities distribution is broader in the simulations than in the observations. Graupel is found to dominate from 5 to 10 km in the simulation, which produces stronger signals from deep clouds (Fig. 2.4h).

2.3 Modifications of microphysics scheme

In the previous section, we showed the biases of the control experiment using the T3EF analysis of the joint histogram and CFADs, especially for deep clouds. We try to improve these results by modifying the cloud microphysics scheme, and focusing on the size distributions of hydrometeors. We used the single-moment bulk scheme NSW6 (Tomita 2008a) in Section 2c. In this study, we stick to the single-moment scheme and examine whether the biases are reduced if the available diagnostic relations are applied to the size distributions of hydrometeors. We describe modifications of the size distributions of snow,

graupel, and rain in Sections 3a, b, and c, respectively. In next section, sensitivity experiments of these modifications will be subsequently shown in Sections 4a, b, and c, respectively.

Before going into the modifications of the size distributions, we introduce common modifications applied to the original NSW6. One of the well-known problems in single-moment bulk microphysics schemes is overestimation of high-density ice such as graupel or hail in mesoscale convective systems compared with observations (Lang et al. 2007; Stith et al. 2002). As the first change in the original scheme, following Lang et al. (2007), we turn off the accretion of snow and cloud ice by graupel (PGACS and PGACI in Tomita 2008b) to reduce the unrealistic presence of high-density ice in the anvil and stratiform portions of clouds. As the second change, we explicitly calculate the ice nucleation and ice deposition processes following Hong et al. (2004) instead of the saturation adjustment of the original NSW6 scheme; when we used the saturation adjustment for sensitivity tests of snow and graupel having large $N_{0[s, g]}$, the amount of cloud ice was significantly reduced in the convective core by depositional processes of snow and graupel.

Table 2.2. List of sensitivity experiments.

	Exp name	Description	periods	Section
	Control	NSW6	30 days	2
	CON	NSW6	7 days	
		PGACI and PGACS are turned off (Lange et al 2007)		3
	CON2	Ice nucleation, ice deposition (Hong et al. 2004)	"	4a
Snow	Fixed_N0S	$N_{0s}=3.0 \times 10^6 \text{ m}^{-4}$, $\rho_s=100 \text{ kg m}^{-3}$		
	HZ79_M3	$N_{0s}=2.0 \times 10^6 \exp(-0.12 \times (T-T_0)) \text{ m}^{-4}$ $\rho_s=100 \text{ kg m}^{-3}$	7 days	3a
	HZ79_M2	$N_{0s}=2.0 \times 10^6 \exp(-0.12 \times (T-T_0)) \text{ m}^{-4}$ $\rho_g=0.15 \text{ D}^{-1} \text{ kg m}^{-3}$		4a
	FS05_M2	Bimodal size distribution $\rho_g=0.15 \text{ D}^{-1} \text{ kg m}^{-3}$		
Graupel	G1	$N_{0g}=4.0 \times 10^6 \text{ m}^{-4}$, $\rho_g=400 \text{ kg m}^{-3}$		3b
	G100	$N_{0g}=4.0 \times 10^8 \text{ m}^{-4}$, $\rho_g=400 \text{ kg m}^{-3}$	7 days	
	LG1	$N_{0g}=4.0 \times 10^6 \text{ m}^{-4}$, $\rho_g=33.7 \text{ D}^{-0.3} \text{ kg m}^{-3}$		4b
	LG100	$N_{0g}=4.0 \times 10^8 \text{ m}^{-4}$, $\rho_g=33.7 \text{ D}^{-0.3} \text{ kg m}^{-3}$		
Rain	MP	$N_{0r}=8.0 \times 10^6 \text{ m}^{-4}$		
	ZH08	$N_{0r}=7.106 \times 10^7 (10^3 \times \text{LWC})^{0.648} \text{ m}^{-4}$		3c
	Combined	1) over 0.001 g m^{-3} of IWC of snow and graupel in melting layer (highest vertical grid over $0 \text{ }^\circ\text{C}$) and below 1 m s^{-1} of vertical wind of each grid: $N_{0r}=7.106 \times 10^7 (10^3 \times \text{LWC})^{0.648} \text{ m}^{-4}$ 2) the other conditions: $8.0 \times 10^6 \text{ m}^{-4}$	7 days	4c

2.3.1 Snow

The high frequency of signals above 12 km in PTH in the simulation (Fig. 2.3) is related to the snow category of the control experiment. We focus on the dependency on the size distribution of snow and examine the changes in the PTH bias with the same size distributions of the other hydrometeors. For the default setting of NSW6, the intercept parameter of snow is set at a constant value, $N_{0s} = 3.0 \times 10^6 \text{ m}^{-4}$, which is based on a ground observation (Gunn and Marshall 1958). However, the intercept parameter in the upper troposphere is much larger according to airplane observations, for example, Heymsfield et al. (2008) suggest a value of $1.0 \times 10^8 \text{ m}^{-4}$ based on upper tropospheric aircraft observations.

The size distribution of snow is known to depend on the temperature and result from aggregation and depositional growth processes. Houze et al. (1979, hereafter HZ79) found that N_{0s} depends on the temperature. Some parameterizations used the following temperature dependence for N_{0s} (Hong et al. 2004):

$$N_{0s} (\text{m}^{-4}) = 2.0 \times 10^6 \exp(-0.12 \times (T - T_0)), \quad (2.7)$$

where $T_0 = 273.15 \text{ K}$, and T is the ambient temperature (K).

Field et al. (2005, hereafter FS05) introduced a parameterization about the moments of the snow size distribution using a second moment and the temperature based on aircraft observation data. Thompson et al. (2008) implemented this approach in their microphysics scheme and tested it for an idealized case. This parameterization employs the bimodal size distribution using a combination of exponential and gamma distributions:

$$N(D) = M_i^{(j+1)/(j-i)} M_j^{(i+1)/(i-j)} \phi_{ij}(x), \quad (2.8)$$

where

$$x = D(M_i/M_j)^{1/(j-i)}, \quad (2.9)$$

$$M_n = \int_0^\infty D^n N(D) dD, \quad (2.10)$$

using the second ($i = 2$) and third ($j = 3$) moments in Table 2.2 of FS05,

$$\phi_{2,3}(x) = 490.6 \exp(-20.78x) + 17.46x^{0.6357} \times \exp(-3.290x). \quad (2.11)$$

After inserting equations (2.9), (2.10), and (2.11) into (2.8), the final form of the size

distribution is given by

$$N(D) = \frac{M_2^4}{M_3^3} 490.6 \exp(-20.78x_{23}) + 17.46x_{23}^{0.6357} \times \exp(-3.290x_{23}), \quad (2.12)$$

where

$$x_{23} = D \frac{M_2}{M_3}. \quad (2.13)$$

Snow is generally less dense than bulk ice in observations and model assumptions because of the open shapes of snowflakes. The density of snow is known to affect the radar reflectivity (Matrosov 1992).

In the default assumption, the density of snow is constant, and the M - D relationship is proportional to the third power of the diameter D . Observational studies show that the exponent is closer to 2 than to 3 (Locatelli and Hobbs 1974). The density of snow is inversely proportional to the diameter in several observations. In this study, we adopt the size-density relationship of the spherical shape assumption corresponding to the M - D relationship. Thompson et al. (2008) has a similar experiment using an M - D relationship (their EXP1 in Thompson et al. 2008): $m(D)=0.069 D^2$ and $\rho_s=0.13 D^{-1}$. We use the empirical equation of Fabry and Szyrmer (1999), given by

$$\rho_s \text{ (} k \text{ gm}^{-3}\text{)} = 0.15D^{-1}. \quad (2.14)$$

We obtain an M - D relationship similar to the observations when we insert (2.14) into (2.2):

$$m(D) \text{ (} kg\text{)} = 0.0785D^2. \quad (2.15)$$

FS05 also used $m(D)=0.069 D^2$ for the second moment of the size distributions in their parameterization. In this study, we used equation (2.15) for FS05 for the sensitivity test.

The effective density is related to the shape of the snow. Larger particles have lower density because they tend to have a two-dimensional planar shape. Smaller precipitation particles have higher densities with a three-dimensional shape.

The default snow size distribution of NSW6 is based on ground observations and does not consider the effect of snow aggregation in the upper troposphere. Thus, it generally overestimates the radar reflectivities of snow. There are several parameterizations of the bulk

size distribution of snow such as HZ79 and FS05. In the control run, the snow mass is proportional to the third order of the mean diameter, whereas it is proportional to almost the second order in the observations. In Section 4a, we test the effects of several parameterizations of the snow size distribution and the M - D relationship of snow on the joint histogram and CFADs of mesoscale convective systems.

2.3.2 Graupel

There are fewer observations of the size distributions of graupel than that of snow. The duration of precipitation is known to increase as the intercept parameter of graupel (N_{0g}) increases (Gilmore et al. 2004; Van Weverberg et al. 2011).

There are large variances in the density of graupel and N_{0g} . We tested an M - D relationship for lump graupel in Locatelli and Hobbs (1974):

$$m(D) \text{ (kg)} = 17.6D^{2.7}. \quad (2.16)$$

We will perform sensitivity tests of N_{0g} following Van Weverberg et al. (2011) using equation (2.16) and a higher N_{0g} .

2.3.3 Rain

The size distributions of rain in observed convective and stratiform precipitation are known to differ (e.g., Tokay and Short 1996; Maki et al. 2001; Rao et al. 2001). The dominant physical processes related to the size distributions of rain are autoconversion, coalescence, and break-up by positive buoyancy and convergence in convective precipitation, whereas rain originating from the melting of snow or graupel and the evaporation process are more important in stratiform precipitation because the relative humidity is lower than convective core. The modal diameters of rain in convective precipitation are smaller than those in stratiform precipitation for the same liquid water content (LWC) (Tokay and Short 1996). Tokay and Short (1996) found that the linear relationship between the LWC and radar reflectivity is different in convective and stratiform precipitation (Fig. 2.5). In the original NSW6 scheme, the default value of the intercept parameter of rain is fixed at $N_{0r} = 8.0 \times 10^6$

m^{-4} . Zhang et al. (2008, hereafter ZH08) introduced the intercept parameter as a function of the LWC based on video disdrometer observations:

$$N_{0r} (m^{-4}) = 7.106 \times 10^6 (10^3 \times LWC)^{0.648}. \quad (2.17)$$

N_{0r} affects other physical processes such as deposition/evaporation and collection.

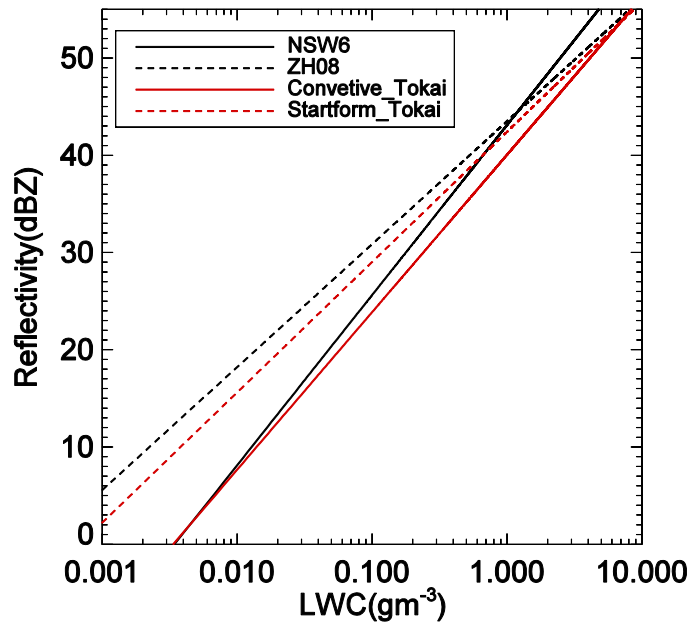


Fig. 2.5: Relationship between radar reflectivity and LWC for NSW6, ZH08, and observations of convective and stratiform systems from Tokay and Short (1996).

Figure 2.5 compares the relations between the radar reflectivity and LWC calculated from the size distributions used by NSW6 and ZH08 and the corresponding linear experimental fittings for convective and stratiform precipitation derived from the observation of Tokay and Short (1996). The ZH08 parameterization is closer to the observed relationship for stratiform precipitation. The MP relation is similar to that observed for convective precipitation.

One of the dominant processes related to rain in stratiform precipitation is evaporation. The MP relation is known to lead to overestimation of evaporation in stratiform precipitation because the evaporation process is more active for smaller particles and is sensitive to the

particle size of rain (Morrison et al. 2009; Xiaowen et al. 2009).

We introduce a simple box model to check how the size distributions of rain change because of evaporation. We compare three bulk methods and one bin method: the three bulk methods are based on the assumed exponential size distribution of NSW6, ZH08, and a double-moment method of Khairoutdinov and Kogan (2000); in the bin method, we divide rain particles in the box into 50 bins and trace the changes in the number and mass of rain in each bin during evaporation. The minimum radius of rain is set to 10 μm . When the radius of rain particles reaches the minimum size, they are removed from the box model. We set up the same initial conditions for sensitivity tests in an exponential distribution with an LWC of 1 g m^{-3} and 80 % relative humidity.

In this box model, the changes in the mass and number concentration in the bin method are given as follows. For evaporation, we use the same evaporation equation as NSW6 (Tomita 2008a):

$$\frac{dm}{dt} = \frac{4\pi D}{\beta} (S_w - 1) F G_w(T), \quad (2.18)$$

where m is the mass of a single particle, $\beta = 2$ for a sphere, and S_w is the supersaturation ratio. The thermodynamic function G_w is given as

$$G_w(T) = \left[\frac{L_v}{K_a T} \left(\frac{L_v}{R_v T} - 1 \right) + \frac{R_v T}{K_d e_w(T)} \right]^{-1}, \quad (2.19)$$

where $K_a = 2.26 \times 10^{-5} \text{ J m}^{-1} \text{ s}^{-1} \text{ K}^{-1}$ is the thermal diffusion coefficient, $K_d = 2.43 \times 10^{-2} \text{ J m}^2 \text{ s}^{-1} \text{ K}^{-1}$ is the diffusion coefficient of water vapor in air, and L_v is the latent heat of liquid water. F is the ventilation factor, given by

$$F = f_{1r} + f_{2r} Re^{1/2} = f_{1r} + f_{2r} c_r^{1/2} \left(\frac{\rho_0}{\rho} \right)^{1/4} \frac{D^{(1+d)/2}}{\nu^{1/2}}, \quad (2.20)$$

where $f_{1r} = 0.78$, $f_{2r} = 0.27$, Re is the Reynolds number, $c_r = 0.5$, $d = 0.5$, and ν is the kinematic viscosity of air. The number concentration is obtained by

$$\frac{\Delta N_r}{N_r} = \left(\frac{\Delta q_r}{q_r} \right)^{\nu_r}, \quad (2.21)$$

where N_r is the number concentration, q_r is the mass concentration of rain, and $\nu_r = 1$. For

comparison with exponential distributions, the slopes λ_{exp} and $N_{0\text{exp}}$ of the bin method are calculated using two points, $D_1 = 0.5$ mm and $D_2 = 2$ mm, by $\lambda_{\text{exp}} = \frac{\log(N(D_1)) - \log(N(D_2))}{D_2 - D_1}$.

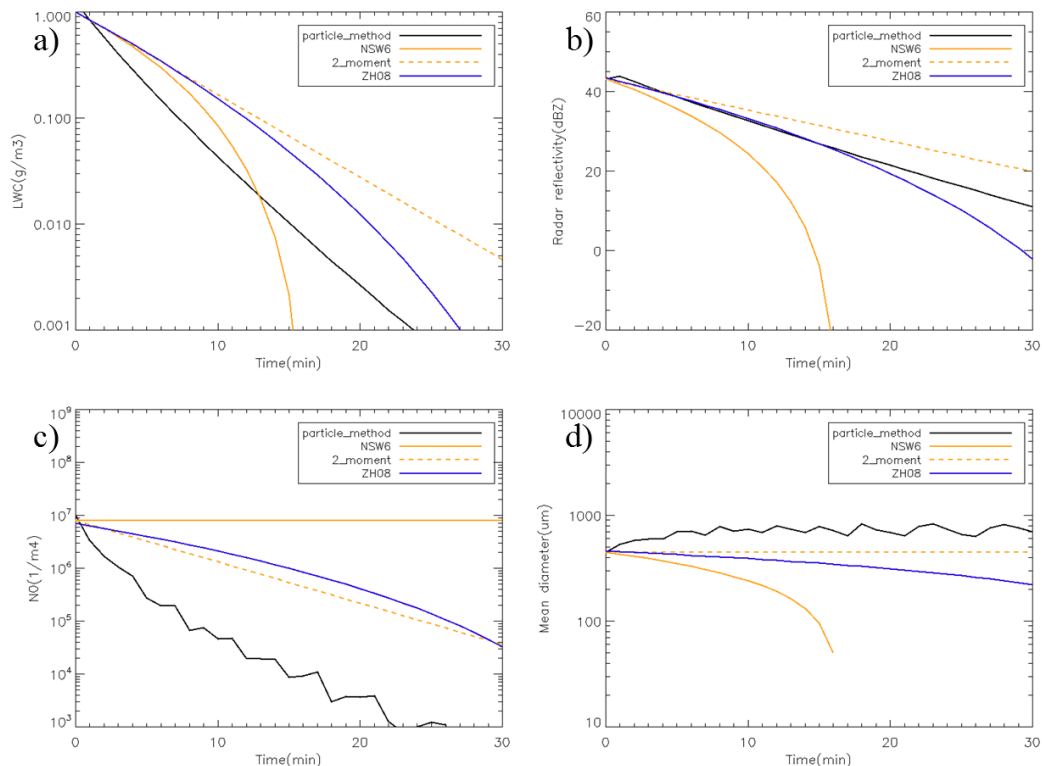


Fig. 2.6: Comparison of temporal variations in LWC, radar reflectivity, N_{0r} , and mean diameter during evaporation of rain for the bin method (black solid curve), NSW6 (red solid curve), the double-moment approach (red dashed curve), and ZH08 (blue solid curve).

Figure 2.6 compares the time evolution of the LWC, radar reflectivity, N_{0r} , and mean diameter among the bin method, NSW6, double-moment scheme, and ZH08 during the evaporation process in the box model. The LWC of NSW6 shows a rapid decrease with time, similar to the bin method. During evaporation, the mean diameter increases slightly in the bin method, and N_{0r} decreases rapidly. For NSW6, because N_{0r} stays constant, the mean diameter decreases during evaporation. Thus, NSW6 overestimates N_{0r} and underestimates the mean diameters compared to the other methods. For the bin method, the mean diameter does not change significantly. The radar reflectivity and mean diameter of the double-moment method

and ZH08 reproduce their evolution and show better agreement with those of the bin method than NSW6. NSW6 underestimates the radar reflectivity relative to the bin method because of the decrease in the mean diameter (Li et al. 2009). If we use the diagnostic relation (4) of ZH08, the radar reflectivity will increase, which increases the frequency of PTH in stratiform precipitation.

The bulk size distributions of rain in convective and stratiform precipitation are different. The MP relation holds well for convective precipitation, whereas the diagnostic relation of ZH08 performs better for stratiform precipitation when we compare it with the observation of Tokay and Short (1996). One reason is that the MP relation with fixed N_{0r} does not represent the change in mean diameter during evaporation.

2.4 Results of sensitivity experiments

2.4.1 Sensitivity experiments setup

We perform numerical experiments to examine the sensitivity of the statistics of clouds and precipitation. In this section, the integration time is limited to 7 days, from 18 UTC 1 January to 18 UTC 8 January. This is because we found that the statistics of 7 days integration exhibit a joint histogram and CFADs similar to those of 1 month integration, however the shallow precipitation is more dominant in this experiment (Fig. 2.7). Hereafter, we refer to the 7 days integration with the original scheme as CON.

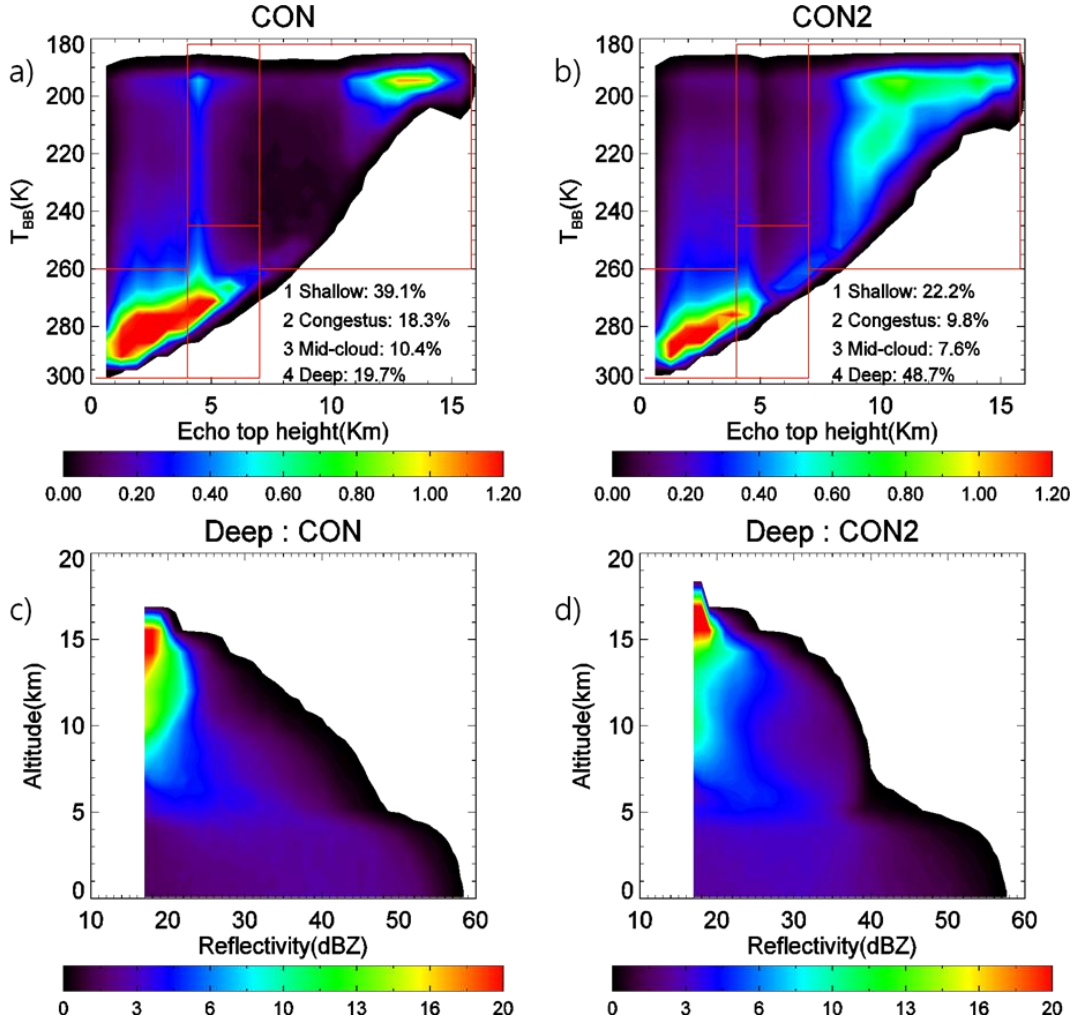


Fig. 2.7: The joint histogram of PTH and TBB (a) and CFADs of deep clouds (c) in the control experiment for the 7 day simulation, and the joint histogram (b) and CFADs of deep clouds (d) for the experiment that applied the two modifications to turn off accretion of graupel with snow and ice and use ice nucleation and ice deposition following Hong et al. (2004) instead of the saturation adjustment.

We investigate the impact of various size distribution parameterizations of precipitating hydrometeors on the joint histogram of TBB and PTH. Before presenting the sensitivities of the size distribution parameterizations of rain, snow, and graupel presented in the previous section, we introduce two changes in the original NSW6 scheme, which are used in all of the following experiments. This experiment is referred to as CON2.

The structure of the joint histogram when these two modifications are applied is similar to the biases of CON. There are high frequency above the 12 km altitude and underestimation of the mid-cold clouds. The ratio of deep clouds is slightly increased to more than 30% compared to CON (Fig. 2.7). The average radar reflectivity of CON2 in CFADs is larger above the 10 km altitude and smaller between 5 and 10 km altitudes than CON. The maximum radar reflectivities of CON2 are slightly reduced than CON.

For the modifications of the size distributions, we first examine the size distribution of snow (Section 4a), then test that of graupel (Section 4b), and finally examine that of rain (Section 4c). The following experiments adopt the same microphysical framework introduced to CON2. We summarize all the experiments in Table 2.2 for the sensitivity tests.

2.4.2 Sensitivity to snow size distributions

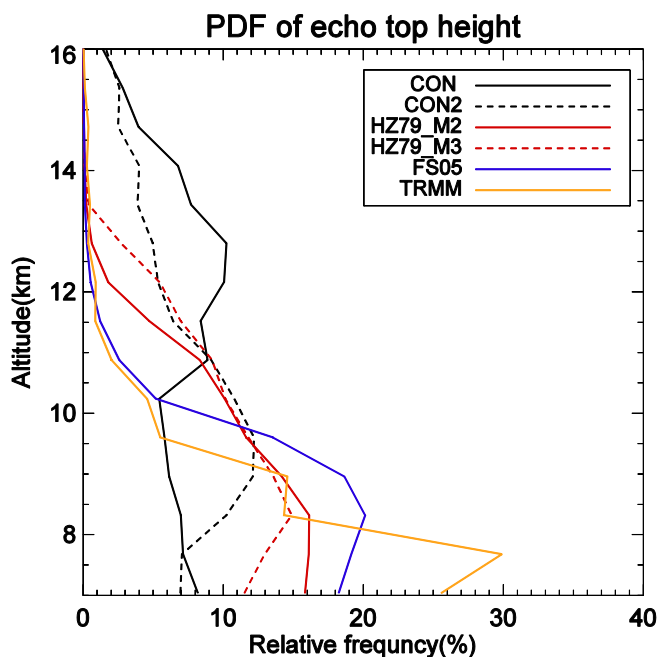


Fig. 2.8: Comparison of vertical distributions of PTH for parameterizations of the snow size distribution (Size distribution assumptions of other precipitating hydrometers are same in NSW6).

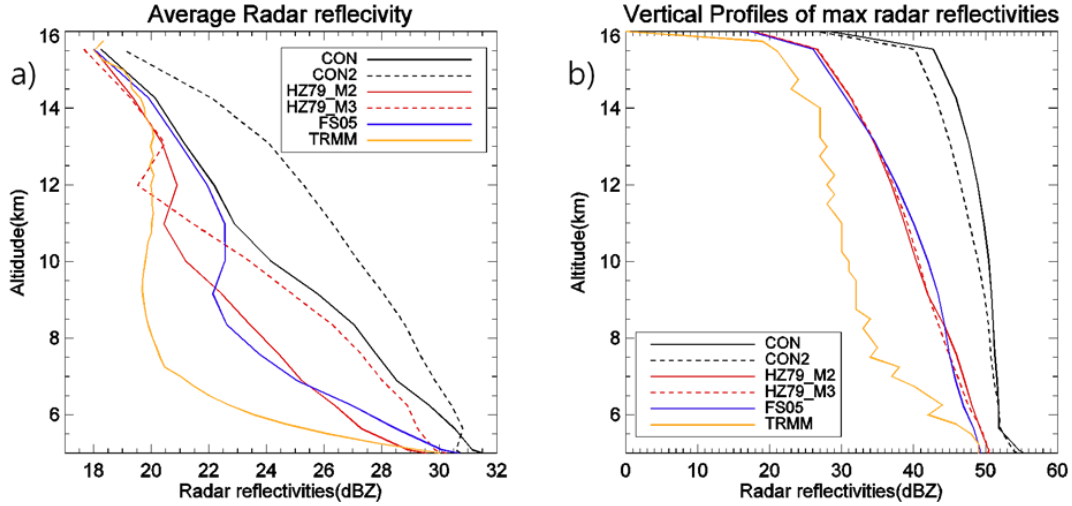


Fig. 2.9: Comparison of average (left) and maximum (right) radar reflectivity profiles for the parameterizations of the snow size distribution (Size distribution assumptions of other precipitating hydrometers are same in NSW6).

Figure 2.8 shows the probability distribution of PTH in deep clouds at altitudes between 7 and 16 km. A peak appears above the height of 10 km in the CON and the CON2, whereas the observed peak is located around the height of 8 km in the TRMM, which is consistent with Fig. 2.3 and Fig 2.7. The parameterizations of the snow size distribution introduced in Section 3a reproduce the PTH profiles better than CON. The peak is located near 9 km for both the HZ79 and FS05 parameterizations, whereas FS05 has a peak at around 8 km. FS05 show a rapid decrease in the ratio above 10 km, similar to the observation. HZ79 overestimates the frequencies of PTH above 10 km. The $M-D$ relationship is less sensitive to the PTH distribution.

Figure 2.9 compares the vertical profiles of the average and maximum radar reflectivity in deep clouds for the sensitivity experiments with each size distribution of snow. The $M-D$ relationship affects the average radar reflectivity profile; the second order of the $M-D$ relationship ($\sim D^2$) using equation (18) in the experiments (HZ79_M2) shows lower radar reflectivities than the third order of the $M-D$ relationship ($\sim D^3$) using a fixed density (HZ79_M3). The observed mean radar reflectivity increases sharply from the altitude of 8 km

down to 5 km. FS05 reproduces vertical profiles similar to the observed profile. The radar reflectivity of HZ79 is higher than the observed values below 11 km, and it increases from 12 km to 5 km. Thus, FS05 shows better results than HZ79 for the joint histogram and the CFADs of deep clouds.

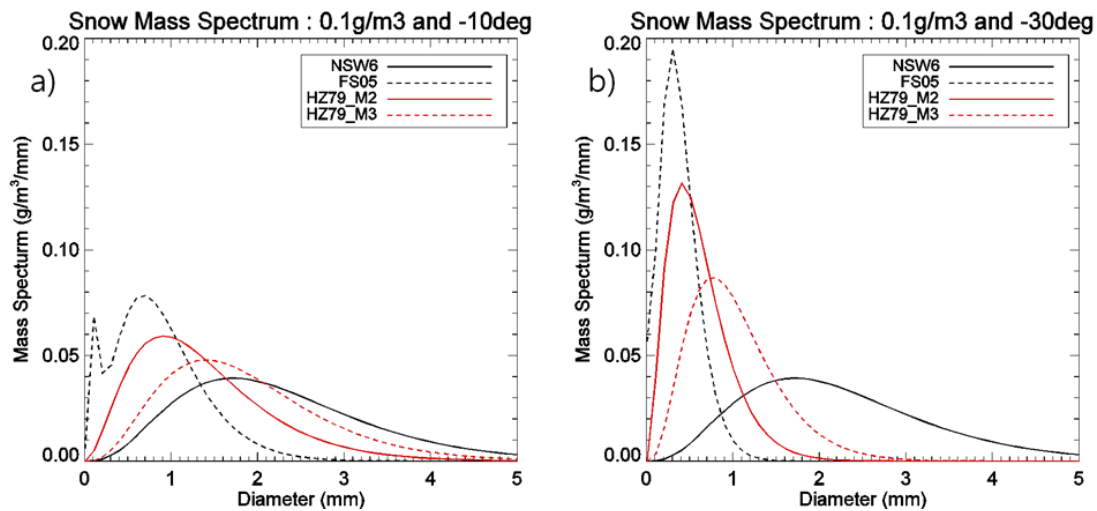


Fig. 2.10: Snow mass spectrum for the parameterizations of the snow size distributions. The ice water content of snow is 0.1 g m^{-3} . Air temperatures are -10°C (left) and -30°C (right).

Figure 2.10 shows snow mass spectrum for the mass concentration of snow 0.1 g m^{-3} at temperature -10°C and -30°C . HZ79 and FS05 show the change of the size distribution depends on the temperature even for with the same ice water content. It reduces the frequency above the 12 km in the joint histograms. HZ79_M2 has smaller diameters and radar reflectivity than the HZ79_M3. FS05 has the bimodal size distribution and the second order of the M-D relationship. These two effects make more realistic joint histogram and CFADs of deep clouds than the H79_M3.

These results correspond to the previous researches. Thompson et al. (2008) using FS05

reproduced the more realistic storm height distributions than the Lin-type microphysics scheme. Van Weverberg et al. (2013) have also shown that MCS cloud properties were better captured using the Thompson parameterization.

In conclusion, among the above parameterizations, FS05 performed the best; therefore, we will use the parameterization of FS05 for the snow size distribution in the following experiments.

2.4.3 Sensitivity to graupel size distribution

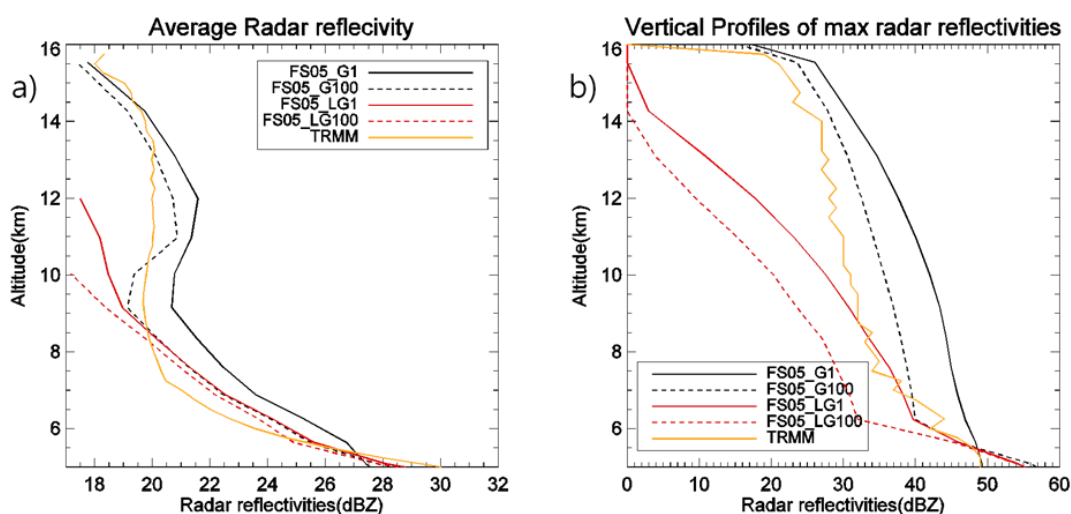


Fig. 2.11: Comparison of average (left) and maximum (right) radar reflectivity profiles for the parameterizations of the graupel size distribution (the snow size distribution is FS05, and other size distribution assumptions are same in NSW6).

We examine the sensitivity of the graupel size distribution to the snow size distribution specified as in FS05. Table 2.2 lists the sensitivity experiments on the size distribution of graupel. We test the sensitivity of N_{0g} and the $M-D$ relationship. First, we increase N_{0g} from the default value $N_{0g} = 4.0 \times 10^6 \text{ m}^{-4}$ (G1) to $N_{0g} = 4.0 \times 10^8 \text{ m}^{-4}$ (G100) based on Knight et al. (1982). We also test the $M-D$ relationships for lump graupel in Locatelli and Hobbs (1974) introduced in section 2.3.2 with $N_{0g} = 4.0 \times 10^6 \text{ m}^{-4}$ (LG1). Finally, we test

the M – D relationship of lump graupel with the increased $N_{0g} = 4.0 \times 10^8 \text{ m}^{-4}$ (LG100). The results show only a small sensitivity of the PTH distribution to the graupel size distribution (not shown). However, we found that the graupel size distribution greatly affects the average and maximum radar reflectivity of the CFADs above the melting layer (Fig. 2.11). The sensitivity test using high values of N_{0g} exhibits a reduced maximum radar reflectivity. The M – D relationship affects the vertical profiles of the maximum radar reflectivity. Sensitivity tests for lump graupel in Locatelli and Hobbs (1974) underestimates the average and maximum radar reflectivity above an altitude of 9 km (LG1 and LG100). The third order of the M – D relationship of graupel has a similar vertical profile of the radar reflectivity in this case (G100). The small size of graupel improves vertical profiles of radar reflectivity, whereas the lump graupel assumption reproduces weaker radar reflectivity with lower density than a constant density assumption over the upper altitude in the convective core.

2.4.4 Sensitivity to rain size distribution

The sensitivities to the rain size distributions are examined with the snow size distribution fixed as in FS05 and the graupel size distribution as in G100. We test three parameterizations of the rain size distributions: the MP relation with fixed N_{0r} , ZH08, and a combination of the MP relation and ZH08 (Combined). The combined method (Combined) is introduced in this study as follows: 1) We classify the stratiform precipitation region as the region that satisfies the conditions $IWC > 0.001 \text{ g m}^{-3}$ in the melting layer (the highest vertical grid above $0 \text{ }^\circ\text{C}$) and vertical velocity $< 1 \text{ m s}^{-1}$; 2) the ZH08 method is used to obtain the rain size distribution in the stratiform precipitation region, and the MP relation is used in the convective precipitation region.

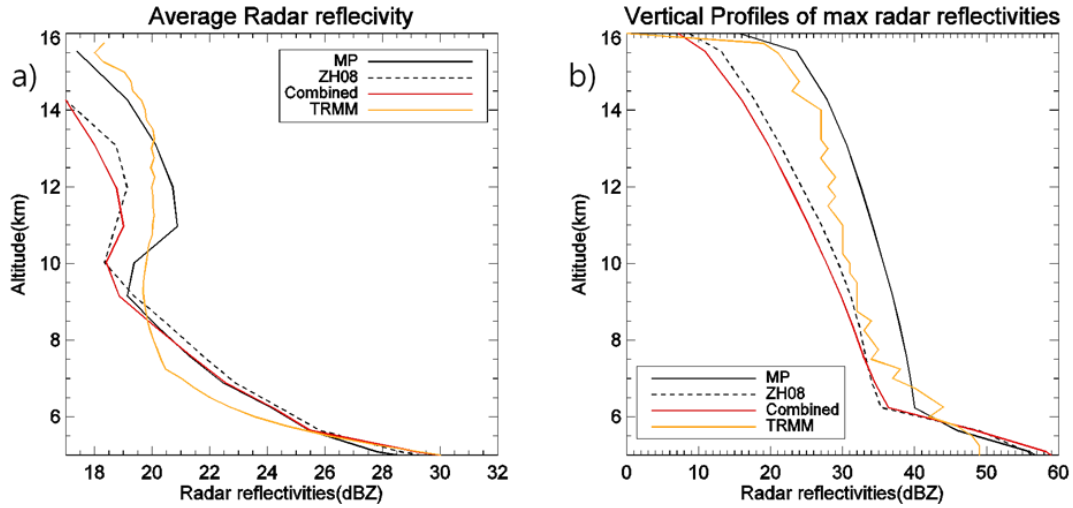


Fig. 2.12: Comparison of average (left) and maximum (right) radar reflectivity profiles for the parameterizations of the rain size distribution (the snow size distribution is FS05, the graupel is G100).

Table 2.3. Frequencies of cloud types for sensitivity experiments on rain size distribution.

Experiment	Shallow (%)	Congestus (%)	Mid-cold (%)	Deep (%)
TRMM	16.1	14.3	29.9	21.1
CON	37.0	17.7	11.2	21.0
CON2	20.5	9.4	7.8	50.8
FS05_G100_MP	30.7	14.1	16.7	23.8
FS05_G100_ZH08	38.5	12.4	14.3	16.1
FS05_G100_Combined	25.2	16.4	22.9	18.8

We examine the contribution of each cloud type in the joint histogram as classified in Table 2.1 as the effects of the rain distribution. The results of the sensitivity experiments are summarized in Table 2.3, which shows the ratio of the four categories of cloud types. MP underestimates the mid-cold clouds compared to the TRMM observation. ZH08 overestimates the shallow clouds and underestimates the deep clouds. Combined increases

the mid-cold clouds compared to MP and decreases the shallow clouds compared to ZH08. The percentage of mid-cold clouds increases from 7.8 % to 22.9 % and the percentage of deep clouds decreases from 50.8 % to 18.8 % from CON to Combined. These values are close to the 29.9 % of mid-cold clouds and 21.1 % of deep clouds in the TRMM observation. Because the rain size of stratiform precipitations is underestimated in the model than observation. When the different approach of rain size distribution, it would increase radar reflectivity in the mid-cold clouds.

Average and maximum radar reflectivities above 10 km are reduced (Fig. 2.12). The rain size distribution affects the reduction of graupel and upper mass flux of rain. It is related to lower evaporation term of ZH08 near the surface than MP to make weaker convection than MP (Xiaowen et al 2009).

2.4.5 Summary of total modifications

We examined how to the modifications of the size distributions of snow, graupel, and rain affect the joint histograms and CFADs of deep clouds. The control experiment (CON) with the original scheme NSW6 overestimated radar reflectivity because temperature dependency of aggregation and depositional growth of snow is not considered. FS05 improves the joint histogram's bias and CFADs of deep clouds by introducing temperature dependency of the intercept parameter, the bimodal size distribution, and the second order of the $M-D$ relationship ($\sim D^2$). For graupel, the intercept parameter N_{og} and the $M-D$ relationship affect the average and maximum radar reflectivities. When the high N_{og} is introduced based on Knight et al. (1982), better CFADs profiles are reproduced because of reduction of radar reflectivities in the convective core. The different approach of rain size distribution reproduces realistic fraction of mid-cold clouds due to increase of the radar reflectivities in the stratiform precipitation.

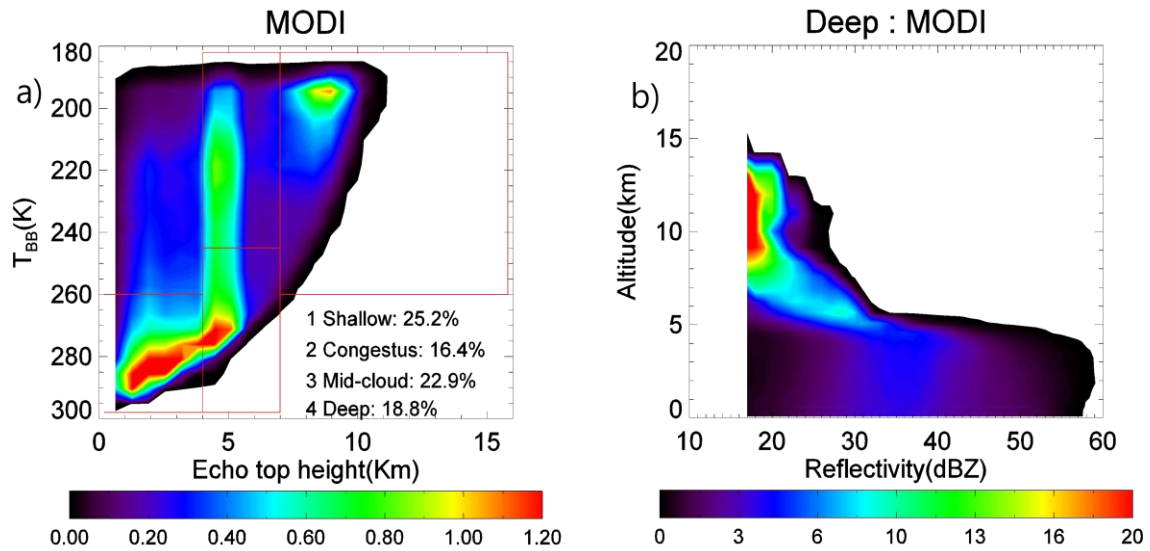


Fig. 2.13: Joint histograms of PTH and TBB (left) and CFADs of deep clouds (right) of MODI.

We compare the joint histograms of the control experiment (CON) and the experiment with the modified size distributions of the three precipitating hydrometeors. It is referred to “Combine” in Section 4d; this experiment is based on FS05 for snow, and G100 for graupel. We think that these choices of the size distributions give the best experiments in terms of the joint histograms and CFADs. Hereafter we referred to this set of the size distributions as MODI. As shown by Fig. 2.13, MODI exhibits a reduced PTH height of high frequencies of deep clouds. The ratio of mid-cold clouds is increased near the melting layer. The mean radar reflectivity and maximum radar reflectivity in the CFADs of deep clouds are similar to those of the TRMM observations (Fig. 2.3 and Fig. 2.13). PTH is reduced in the layers between 5 and 10 km.

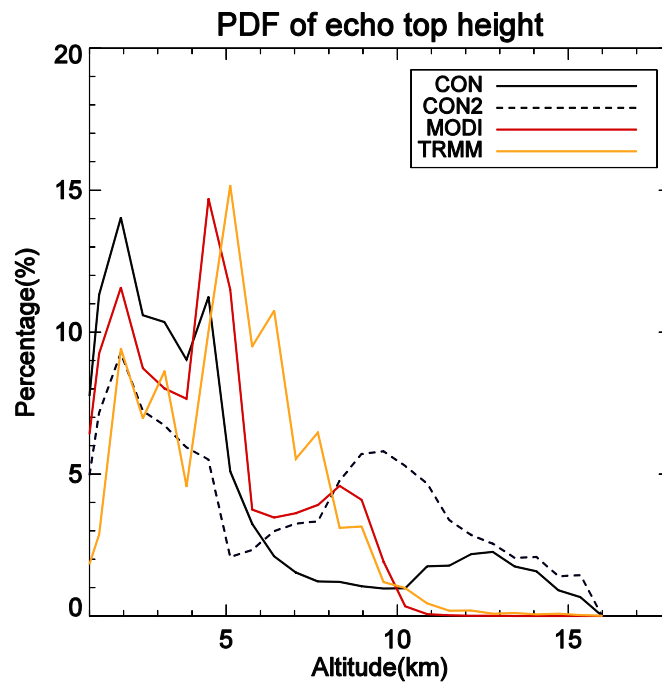


Fig 2.14: Comparison of the probability of PTH for the TRMM observation, CON, CON2, and MODI.

The radar reflectivities below the melting level (5 km) is still overestimated, similar to CON. This means that the numerical simulation overestimates precipitation, or the MP relation and ZH08 overestimate the radar reflectivity of rain compared with the observations in Tokay and Short (1996) (Fig. 2.5). Figure 2.14 corresponds to Fig. 2.13a, and it shows that modified size distributions decrease high frequency of PTH over 10 km and increase the frequency near 5 km; the result of MODI is better than that of CON2 for deep clouds and mid-cold clouds. However, the frequency of PTH is still underestimated between altitudes of 5 and 7 km in the modified run.

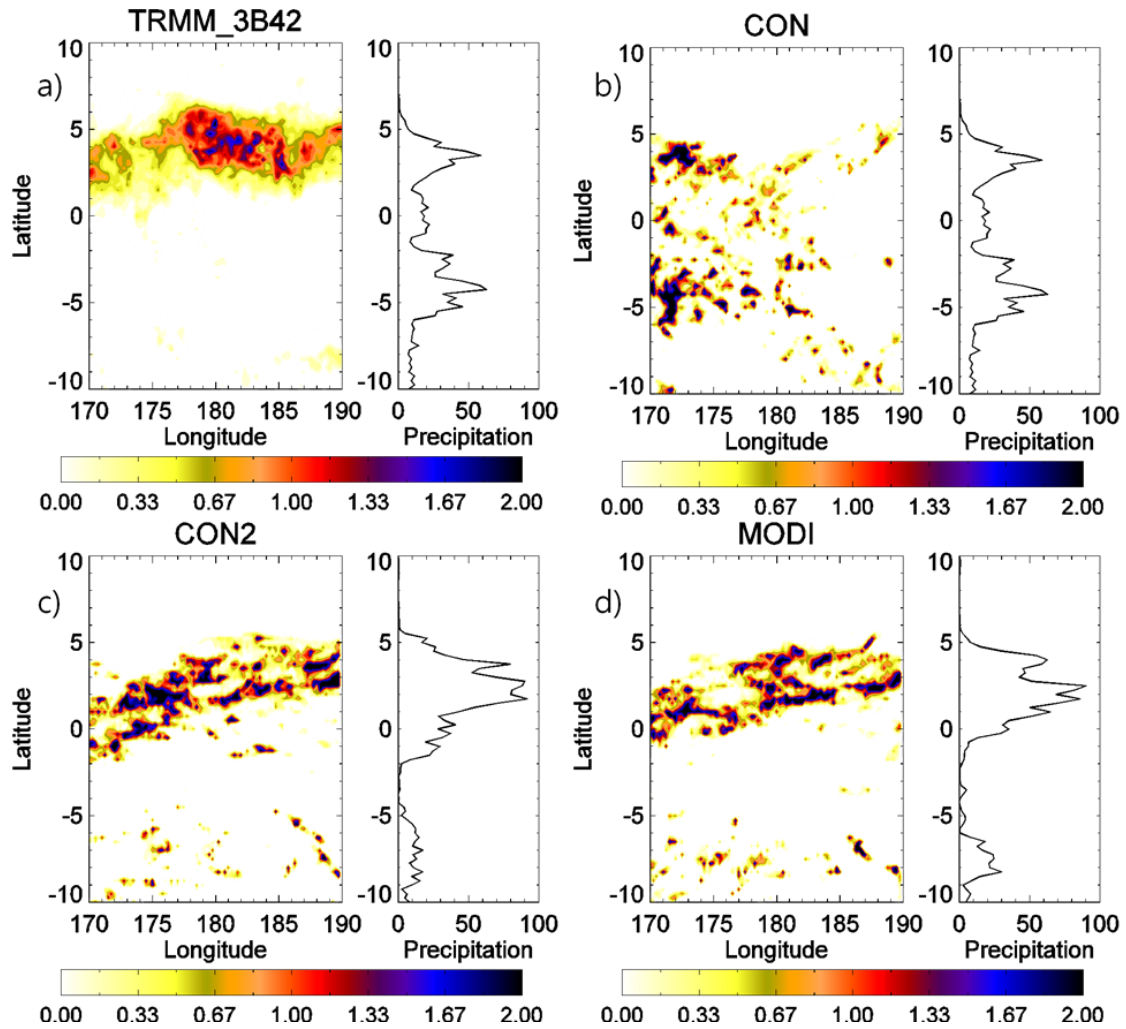


Fig. 2.15: Comparison of accumulated precipitation of a) TRMM 3B42, b) CON, c) CON2, and d) MODI over the domain.

Figure 2.15 shows the accumulated precipitation among TRMM 3B42, CON, CON2, and MODI. The precipitation is concentrated near 5° latitude in TRMM 3B42 observation, but CON did not capture the precipitation distribution. CON2 and MODI reproduce the similar precipitation pattern. It means the different precipitating hydrometeor's size distributions do not affect the accumulated precipitation distribution comparing CON2.

2.5 Discussion and Conclusion

In this study, we evaluated the cloud and precipitation properties of numerical simulations of NICAM for a single-moment bulk microphysics scheme using the TRMM PR and TBB with a satellite simulator. We investigated the effect of modifications of the size distributions of precipitating hydrometeors on the joint histogram of TBB and PTH from the TRMM PR for mesoscale convective systems over the tropical open ocean. Cloud-system-resolving simulations reproduced a horizontal cloud size distribution similar to those observed by geostationary satellites. We found that the control experiment with the defaults parameters of NSW6 leads to an overestimated frequency of deep clouds that is, in the joint histogram analysis the frequency of the deep cloud category is overestimated and PTH is overestimated above 12 km in the control run. It is due to the number concentrations of large snow particles resulted from the long tail negative exponential size distribution assumption over high altitude. The default assumption does not consider the mean size with height. Numerous studies have documented the exponential variation of the slope or characteristic size with height (Houze et al. 1979; Mitchell 1988; Westbrook et al. 2007). It has been suggested that this observed relationship is due to aggregation increasing of the mean size of the distribution. The control run also underestimates the frequency of mid-cold clouds. The negative bias of the fraction of mid cold clouds is due to small mean sizes of rain in the MP size distribution in the stratiform precipitation regions. The MP size distribution does not reproduce the climatological rain size in the stratiform precipitation. One of possible reasons is the problem of evaporation process in a single bulk microphysics in the stratiform precipitation.

To improve the statistical frequency and CFADs of the simulated clouds, we examined the effects of the size distributions of hydrometeors. First, the sensitivity of the snow size distribution was examined using several $M-D$ relationships. The snow size distribution affects the probability distributions of PTH in deep clouds. When the scheme of Field et al. (2005) is used, the bias of a too-high PTH is reduced, and the probability of PTH becomes closer to that of the TRMM observation. It is related to the bimodal size distribution and the $M-D$ relationship. The $M-D$ relationship affects the mean radar reflectivity of the CFADs.

Next, we found that the graupel size distribution affects the maximum radar reflectivity. The maximum radar reflectivity in the upper troposphere decreased rapidly when the $M-D$ relationship of lump graupel in Locatelli and Hobbs (1974) was applied.

Third, from the sensitivity to the rain size distributions, we found that the frequency of shallow, congestus, and mid-cold clouds can be modified. The method of ZH08 reproduces a better representation of the size distribution of the stratiform precipitation. However, the frequency of shallow clouds is increased. Therefore, we introduced a combined parameterization that uses different rain size distributions for convective and stratiform precipitation. The results show that this quantitatively improves the frequency of cloud categories in the joint histogram. However, there are overestimations of radar reflectivities below altitude of 5 km. One of possible reasons is the horizontal resolution; we used about 3 km grid space for the simulation. It is known that vertical mass flux is overestimated around this resolution because of underestimation of detrainment (Bryan and Morrison 2012; Caine et al. 2013; Weverberg et al. 2013). The other reason might be related to autoconversion and accretion of liquid process, since similar overestimation of radar reflectivities is seen in congestus and shallow clouds.

The modification of microphysics affects the dynamics especially for vertical wind distribution in the upper altitude. Figure 2.16a shows probability distribution of vertical velocity at 10 km altitude; MODI has relatively high frequency of strong updraft velocity over 15 m s^{-1} than CON and CON2. We speculate that it is related to the weakening of precipitation flux with reduced graupel and smaller snow size. These effects are more dominant at high altitudes around 10 km than the lower levels.

Vertical profiles of the domain average temperature have differences of MODI between CON and CON2 (Fig. 2.16b). The ice nucleation and reduction of graupel has strong effects on the average vertical profile of temperature. It is related to the deposition and sublimation process of snow in CON2; the condensation heating is larger above 10 km by high relative humidity with respect to ice and abundant snow, whereas sublimation cooling is larger than CON near 6 km.

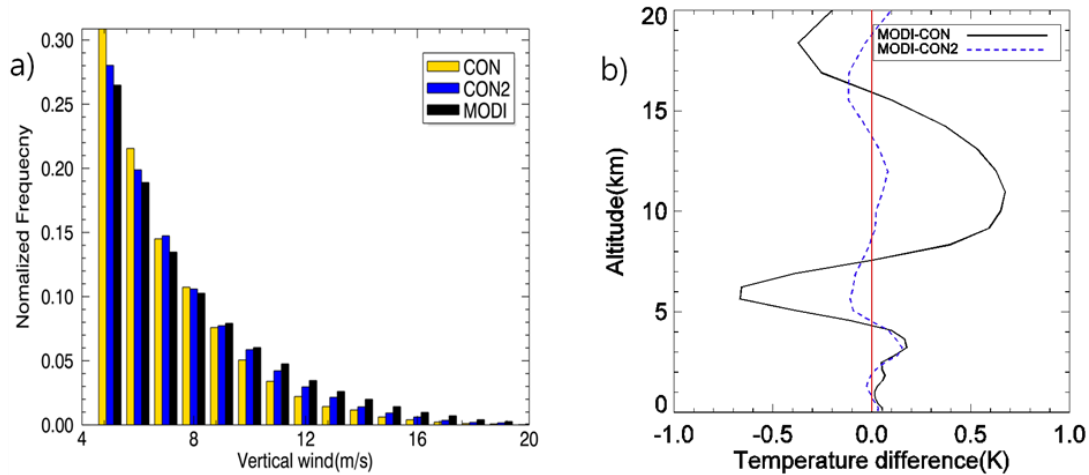


Fig 2.16: a) Normalized frequency of vertical winds for the CON, CON2 and MODI, and b) vertical profiles of averaged temperature differences of MODI with CON and CON2.

Table 2.4. Domain and temporal averages of OLR for 7days among CON, CON2, MODI, and daily NOAA OLR.

Experiment	CON	CON2	MODI	NOAA OLR
OLR	257.4 Wm ⁻²	242.9 Wm ⁻²	239.1 Wm ⁻²	239.6 Wm ⁻²

We compare the domain and temporal averaged OLR among CON, CON2, MODI, and daily NOAA OLR for 7 days in the analysis domain (Table 2.4). This shows that OLR is reduced by more than 15 W m⁻² in CON2 and MODI in comparison with CON, and it becomes closer to the observation. It is because of nucleation and reduction of graupel. The modified size distributions affect decrease of almost 4 W m⁻² OLR than CON2; it is related to the snow size distribution parameterization; smaller size of snow has more residence time in FS05 than a constant N_{0s} .

Table 2.5. Average ratio of convective/stratiform precipitation among CON, CON2, and MODI.

Experiment	CON	CON2	MODI
Percentages	26.8 %	24.1 %	21.5 %

Finally, we investigated average ratio of convective/stratiform precipitation (Table 2.5). We defined mesoscale convective precipitation systems defined as larger 1225 km² rainy area with over 1 mm hr⁻¹ precipitation. We divide convective precipitation considered as over 20 mm hr⁻¹ and the other areas as stratiform precipitations. The average ratio of convective/stratiform precipitation are reduced from 24.1 % of CON2 to 21.5 % by MODI. It means the stratiform precipitation increases in MODI.

In this study, we focused on the Central Pacific and got better results like joint histogram, CFADs, and OLR comparing observations. There are differences of microphysical characteristics in different locations of the ocean. In the future, we intend to expand the global simulation for evaluations with a several km homogenous resolution in order to evaluate these modifications in all area of the ocean. We also would compare other satellites such as Cloudsat and CALIPSO.

3 Analysis of a global simulation

W. Roh and M. Satoh

(Under preparation for publication in *Journal of the Atmospheric Sciences*)

3.1 Introduction

As the computational speed and memorial storage resource rapidly increase, global cloud system resolving models (GCSRMs) are available with a several kilometer mesh to reproduce realistic cloud systems over the globe. The GCSRMs could simulate deep convective systems without cumulus parameterization. They consider interactions from regional to large scale processes. In the previous chapter, the cloud systems over the specific tropical open ocean are evaluated using the TRMM data. The purpose of this chapter is to investigate how the modified microphysics scheme in chapter 2 simulates cloud systems in the other tropical regions and mid-latitude areas. The cloud structures over the globe are evaluated using a global cloud resolving model in this chapter.

There are some studies to evaluate precipitations and cloud properties of GCSRM simulations using satellite data. Sato et al. (2008) studied the characteristics of diurnal precipitations over the entire tropical region using a TRMM satellite data. Hashino et al. (2013) examined the vertical structures of clouds of a GCSRM with a 3.5 km horizontal mesh of latitude 82S– 82N using merged CloudSat and CALIPSO data and retrieved microphysics data based on Hagihara et al. (2010). Most of GCSRM studies are aimed at comparisons with numerical simulations using a single microphysics and observation because of the heavy requirements in terms of computation time for the sensitivity tests of microphysics. Many evaluation studies using different microphysics focus on the local domain based on field campaigns (Matsui et al. 2009; Vable et al. 2010; Powel et al. 2012). For example, Matsui et al. (2010) evaluated cloud properties in only two tropical regions such as the Amazon (TRMM LBA) and Western Pacific area (KWAJEX) using different microphysics schemes. Satoh et al. (2010) suggested the use of a regional version of a CSRM with the same physic

schemes and dynamics as those of a GCSRM to evaluate and improve microphysics schemes and obtain better cloud properties in GCSRM simulations.

In this chapter, the microphysics modified in the previous chapter was tested for global regions using a GCSRM. In section 3.2, the experimental design and observational data are described. In section 3.3, the horizontal distributions of TBB and accumulated precipitations are evaluated among observations, CON, and MODI. In section 3.4, we compare the vertical structure of the tropical cyclone Fengshen using TRMM PR and CloudSat. In section 3.5, T3EF results in the total tropical regions and some middle latitude areas are evaluated. The CloudSat data is used for comparisons in section 3.6. Summary and conclusions are given in section 3.7.

3.2 Experimental designs and data

The GCSRM simulation was carried out using a global version of NICAM with 3.5 km horizontal resolution, courtesy of Dr. Nasuno in the JAMSTEC, using the supercomputer Earth simulator. The integration time is from 12 UTC 15 to 12 UTC 18 June 2008. The first day is used for the spin up time. The 2 days simulations are analyzed from 12 UTC 16 June to 12 UTC 18 June 2008. The NICAM simulations were initialized with the ECMWF YOTC (Year of Tropical Convection) data with a 0.5 degree resolution for winds, temperature, relative humidity, and geopotential data. Furthermore, the sea surface temperature is calculated with a slab ocean scheme and nudged to Reynolds weekly SST at 5-day relaxation time, but other variables were integrated without the nudging process. The land surface model is the bucket model. Other physics schemes and vertical resolutions are the same as in the previous chapter. We tested two microphysics schemes; the first is the original NSW6 (same as CON in chapter 2), and the second is the modified NSW6 based on chapter 2 (same as MODI in chapter 2). We also use vertical profiling data of 95 GHz radar reflectivities in 2B-GEOPROF CloudSat data with 1 km horizontal resolution for additional analysis (Stephens et al. 2002). The CloudSat data is more sensitive to small cloud ice particles and snow than the TRMM data due to the smaller minimum detectable signal and higher

wavelength. Therefore, it is useful to analyze the vertical structures of non-precipitating ice phased clouds using the CloudSat data.

3.3 Horizontal distributions of the TBB and accumulated precipitations

The observed 11 μm TBBs are compared to the TBBs simulated with CON and MODI on 12UTC 18 June (Fig. 3.1). Both simulations have similar horizontal distributions compared to observations. A long convective band exists in the Pacific Ocean near the equator. The deep clouds are well simulated near the equator in Africa and on the American continent. The tropical Fengshen is located near the Philippines in observation and both simulations reproduced it. In general, MODI produces a larger size of upper clouds than CON.

Figure 3.2 shows the accumulated precipitations of TRMM 3B42, CON, and MODI for two days simulations. The precipitation locations are close to those of the lower TBB distributions in Figure 3.1. The locations of two simulated precipitations are comparable to observations, but the accumulated precipitation sizes are overestimated. Interestingly, both simulated precipitation distributions are very similar. It means that the large-scale precipitation distribution is not so sensitive to microphysics for a few days simulation. The total amount of accumulated precipitations in the simulations is overestimated compared to observation (Fig. 3.3). In particular, the difference is largest between the observation and simulations near 8 degrees in the tropical region. In chapter 2, horizontal distributions of the accumulated precipitation are changed by the modification of the microphysics scheme. However, Fig 3.3 shows that the modification of the microphysics scheme does not affect the horizontal distribution and total amount of precipitation on a global scale.

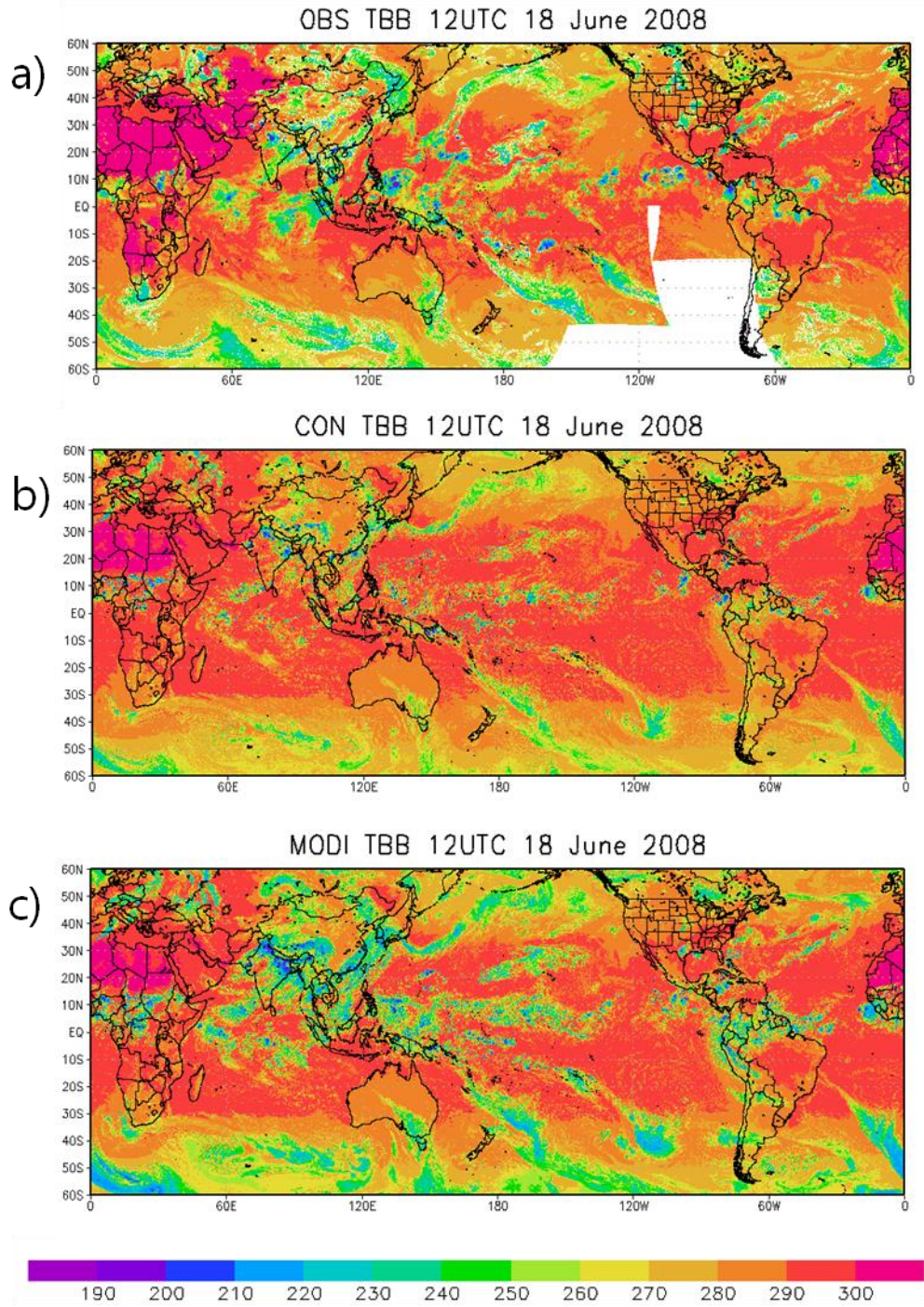


Fig. 3.1: Comparisons of the horizontal distribution of $11\mu\text{m}$ TBB from the observation (top) and the CON simulation (middle), and MODI simulation (bottom) by NICAM at 12 UTC 18 June 2008.

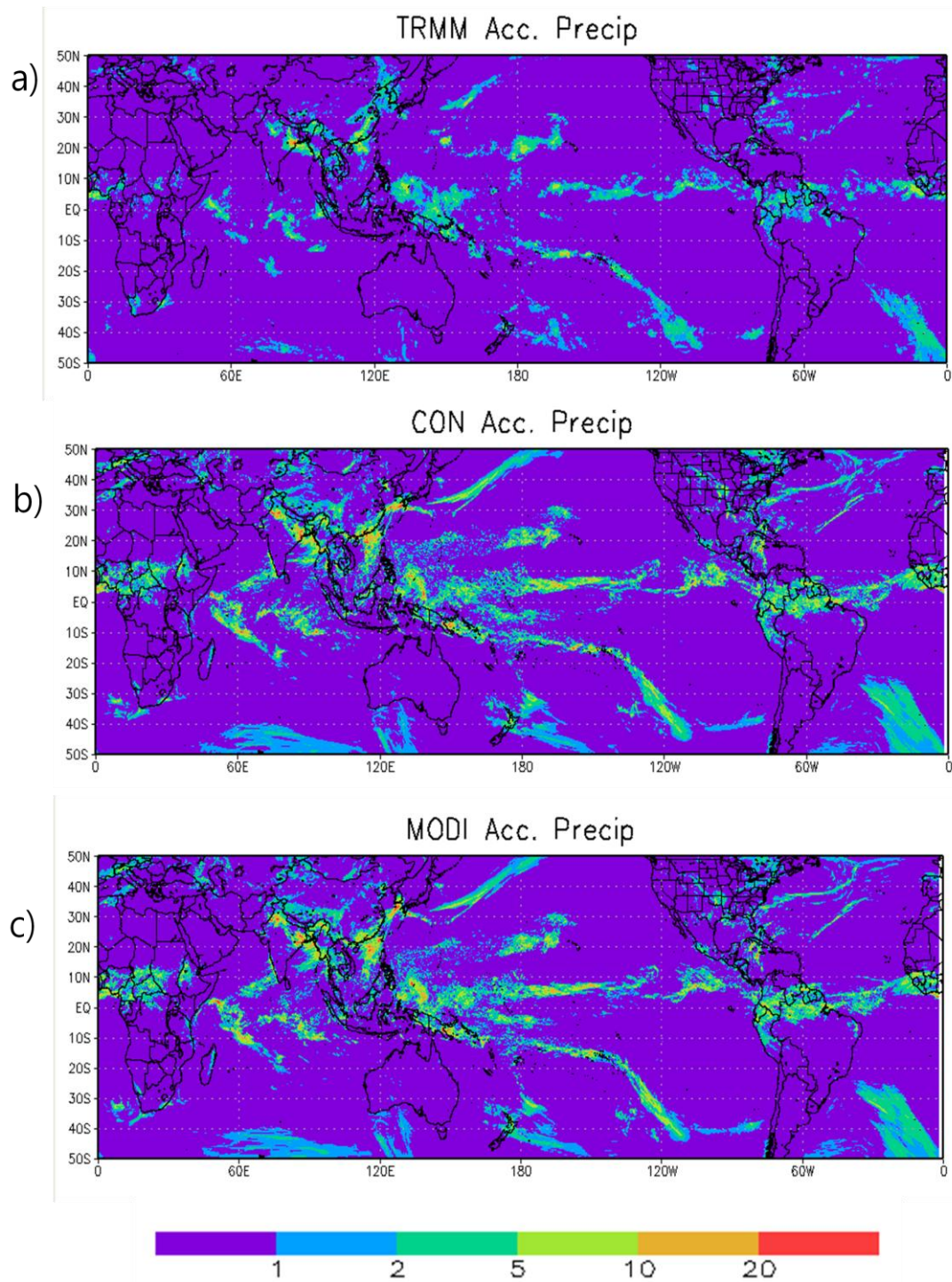


Fig. 3.2: Comparisons of the horizontal distribution of the accumulated precipitations from TRMM 3B42 (top) and the CON simulation (middle), and MODI simulation (bottom) by NICAM from 12UTC 16 to 12 UTC 18 June 2008.

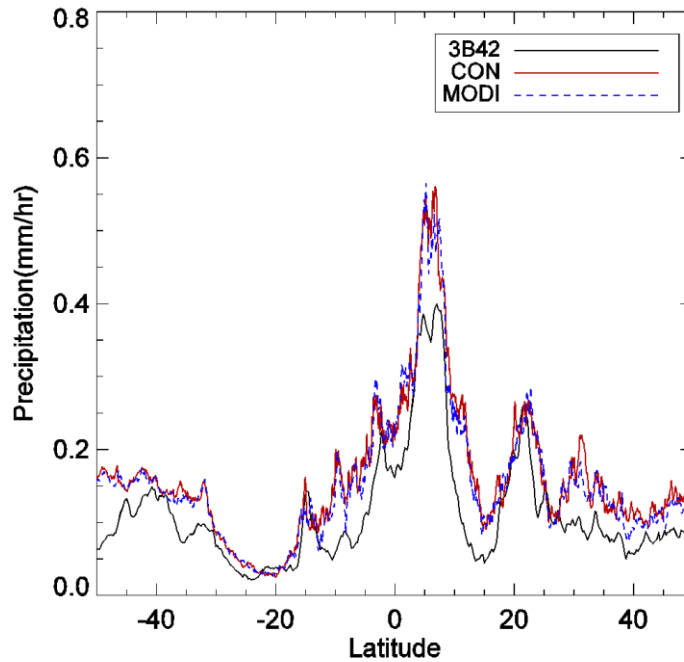


Fig. 3.3: Zonal averaged accumulated precipitations for the TRMM 3B42 observation, CON, and MODI for the 2 day simulations.

3.4 A case study of the tropical cyclone Fengshen

A tropical cyclone is one type of clouds and precipitation systems of mesoscale convective systems, which have convective and stratiform precipitations. It is easier to take a tracking and direct distinction between the model and observation than typical MCSs. First, we examined the tropical cyclone Fengshen by directly comparing the vertical profiles in order to understand the differences in simulated signals. Figure 3.4 shows the observed 11 μm TBB and the cross-section of 13 GHz radar reflectivities at 17 UTC 19 June for TC Fengshen. We have only 3 days simulations, and compared them to the observations at 12UTC 18 June, which is the closest date data to the observation. CON and MODI simulated a more isolated precipitation pattern than the observation. Hashino et al. (2013) also reported that a global NICAM reproduces more isolated convective cells and less spread of detrainment than the observation. CON shows that the precipitation systems are more scattered and that the frequencies of radar reflectivities over 10 km heights are higher compared to TRMM data.

The 13 GHz of radar reflectivities of TRMM observations shows that most of the maximum heights of deep convective systems are less than 10 km. The MODI shows that precipitation systems are well organized and better cross section profiles having low frequencies of signals over 10 km like observation.

Second, we compare the vertical radar reflectivity profiles of 95 GHz of CloudSat on 23 UTC 19 June with simulations at 12 UTC 18 June (Fig. 3.5). The 95 GHz signals capture a larger fraction of cold clouds over 5 km than the TRMM PR. It is able to investigate anvil cloud characteristics. The CloudSat observation shows maximum radar reflectivities larger than 10 dBZ from 4 to 10 km altitude, which related to precipitation particles. However, the radar reflectivities of CON are underestimated due to the strong attenuation of upper clouds. MODI shows larger radar reflectivities than CON with weaker attenuations. The precipitation systems are well organized like observation compared with CON like TRMM PR results.

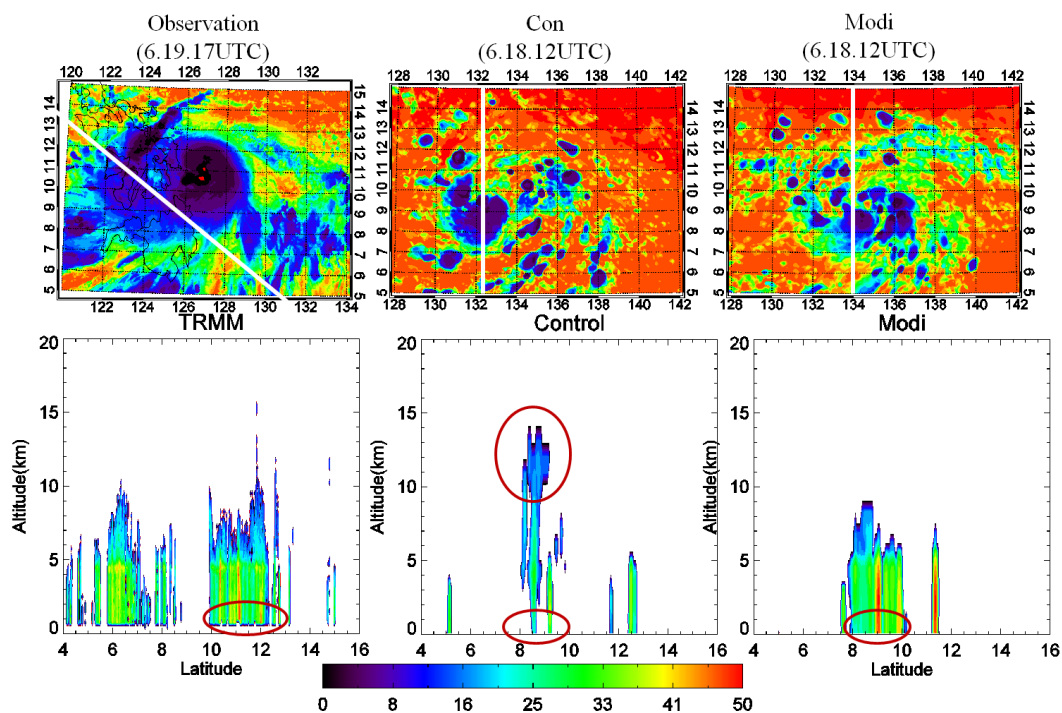


Fig. 3.4: The horizontal distributions of TBB (upper) and vertical cross sections of 13 GHz radar reflectivities (bottom) in the tropical cyclone Fengshen for TRMM (left), CON (middle), and MODI (right). White curves indicate the cross section line below the figures.

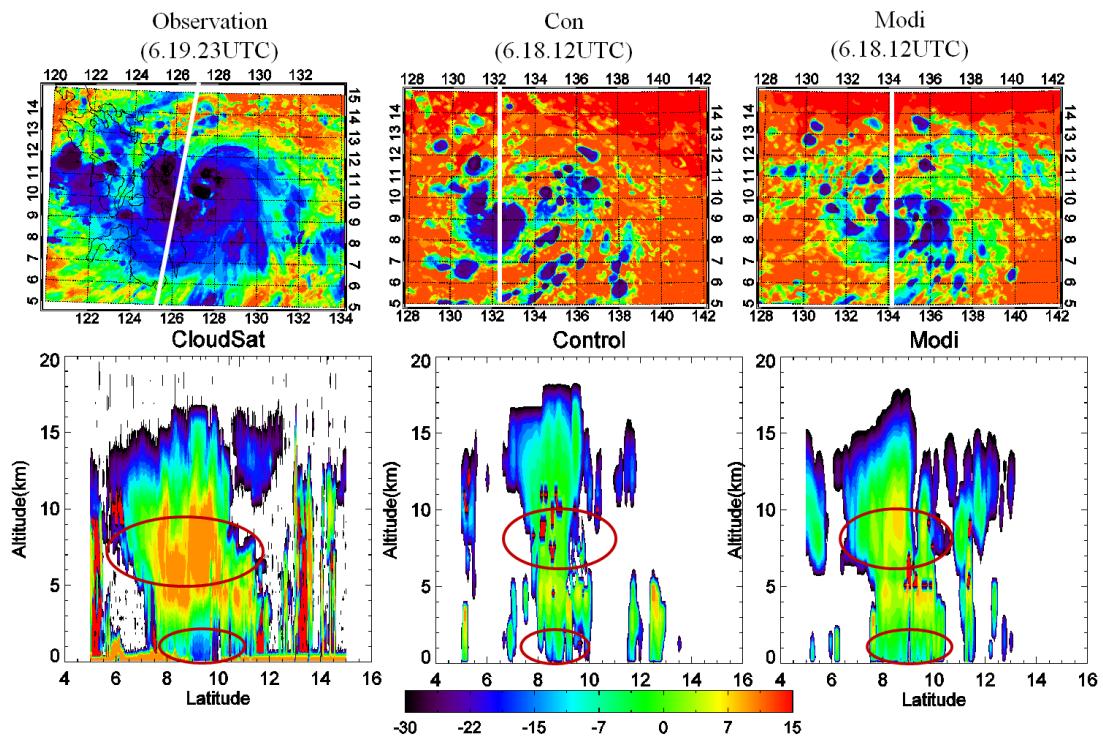


Fig. 3.5: The horizontal distributions of TBB (upper) and vertical cross section of 95 GHz radar reflectivities (bottom) in the tropical cyclone Fengshen for CloudSat (left), CON (middle), and MODI (right). White curves indicate the cross section line below the figure.

3.5 T3EF analysis in the global domain

In chapter 2, the analysis domain is limited to the central Pacific Ocean about joint histograms and CFADs of deep clouds. We expanded the evaluation to the entire tropical region in order to investigate how the previous modified microphysics scheme using a regional CSRMM is applicable to other regions. Masunaga and Kummerow (2006) analyzed regional and temporal variability using the joint histogram between TBBs and echo top heights in the tropical area using TRMM and NCEP reanalysis data. They found that the effect of SST and larger scale forcing affects the joint histogram structure. For example, the increase of frequencies of shallow precipitation is accompanied by a decrease of SST.

Figure 3.6 shows the joint histogram of TRMM, CON, and MODI for the total tropical area (20S – 20N). The results of MODI are improved compared to CON comparing to TRMM almost similarly to those obtained for the central Pacific case in chapter 2. However, the ratio of deep clouds in MODI is underestimated compared to observation. The CFADs of deep clouds for the entire tropical region are also similar in structure as described in chapter 2 (Fig. 3.6). CON shows a better statistics of deep clouds than MODI, whereas MODI reproduces closer statistics of shallow and mid-cold clouds than the observation (Table 3.1).

Table 3.1. Frequencies of cloud types for the TRMM, CON, and MODI over the entire tropics.

Experiment	Shallow (%)	Congestus (%)	Mid-cold (%)	Deep (%)
TRMM	17.1	18.1	27.9	24.2
CON	37.3	23.6	5.6	23.2
MODI	24.1	26.3	26.3	14.4

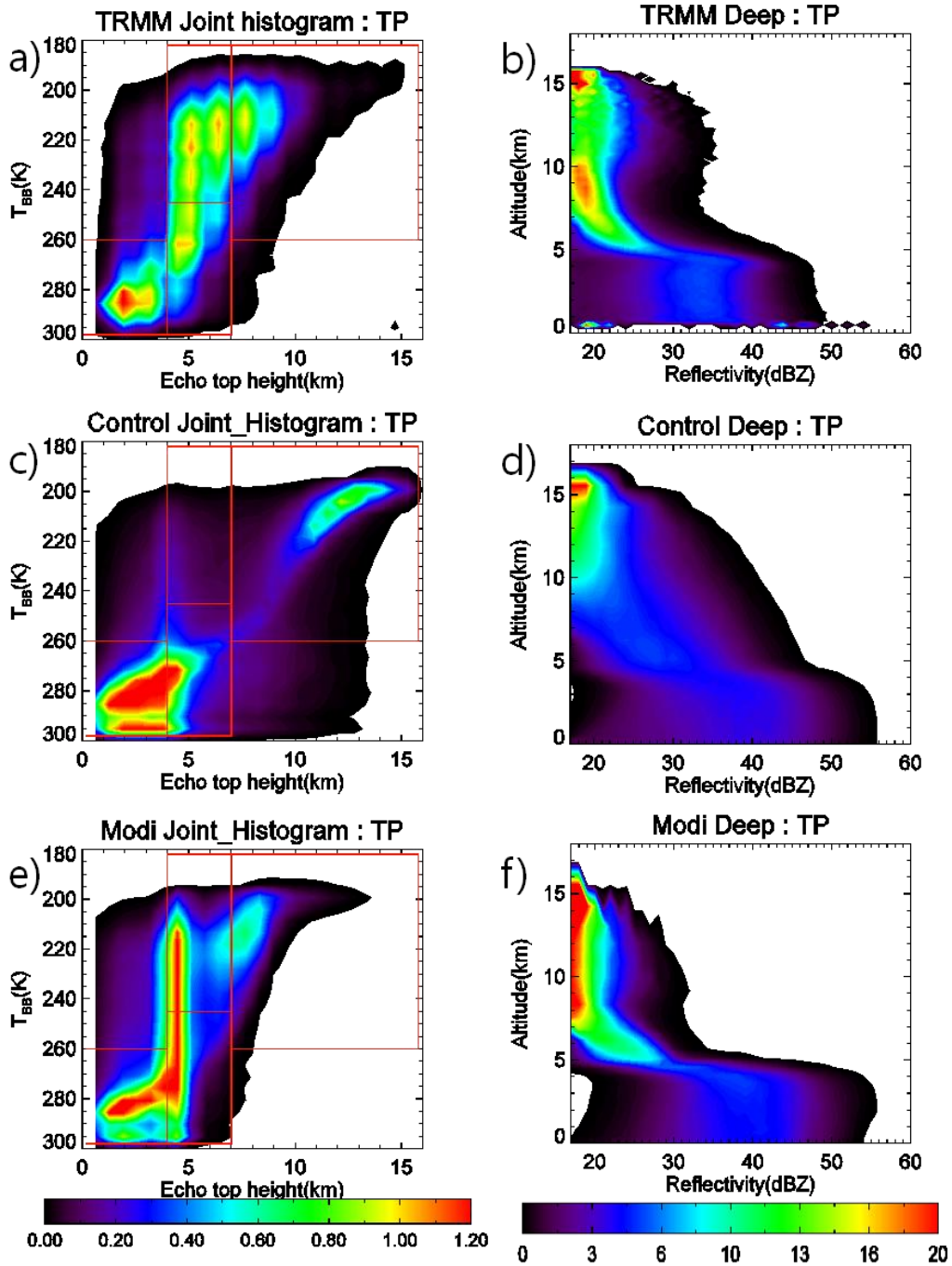


Fig. 3.6: The joint histogram of PTH and TBB (left) and CFADs of deep clouds (right) for the TRMM observation (top), CON (middle), and MODIS (bottom) for the 2 day simulation over the entire tropics.

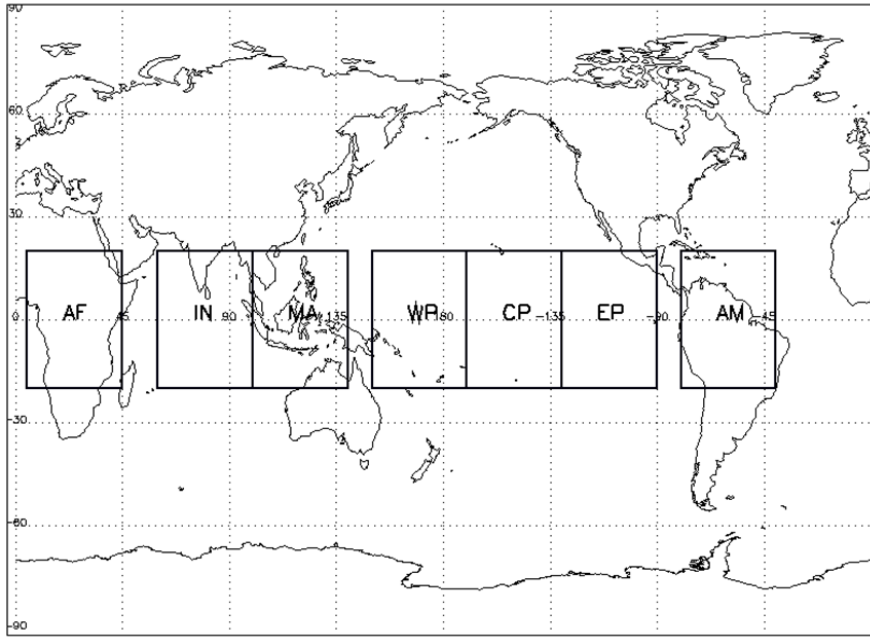


Fig. 3.7: Seven tropical regions selected for analysis: Africa (AF), Indian Ocean (IN), Maritime Continent (MA), Western Pacific (WP), Central Pacific (SP), Eastern Pacific (EP), and America (AM).

We subdivided the global data into seven tropical regions to investigate the regional differences in joint histograms, representative of the characteristics of tropical regimes (Figure 3.7). Figure 3.8 and 3.9 show the joint histograms of Africa (AF), Indian Ocean (IN), Maritime Continent (MA), Western Pacific (WP), Central Pacific (SP), Eastern Pacific (EP), and America (AM). The general feature of regional differences shows a high frequency of deep clouds in land areas such as AF, MA, and AM in the observation. The simulations reproduce similar characteristics except for AF, where shallow clouds are dominant. There is a predominance of shallow clouds in ocean areas in observation. We investigate the reason for this with respect to regional differences between cloud systems. We divide the land and ocean areas and the dependency of SSTs over the ocean.

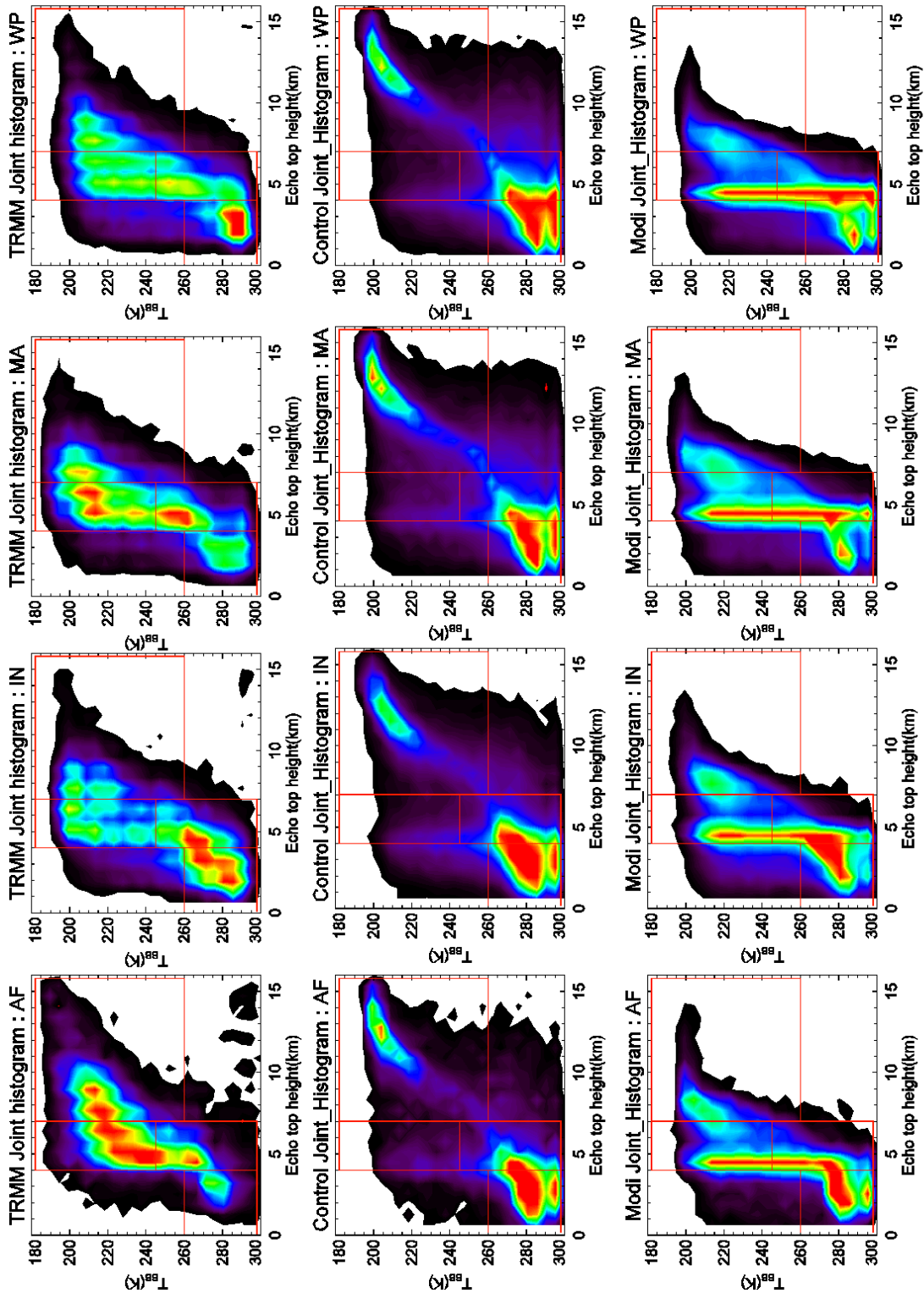


Fig. 3.8: The joint histogram of PTH and TBB of TRMM (left), CON (middle), and MODIS (right) for Africa (AF), Indian Ocean (IN), Marine continental areas (MA), and Western Pacific (WP).

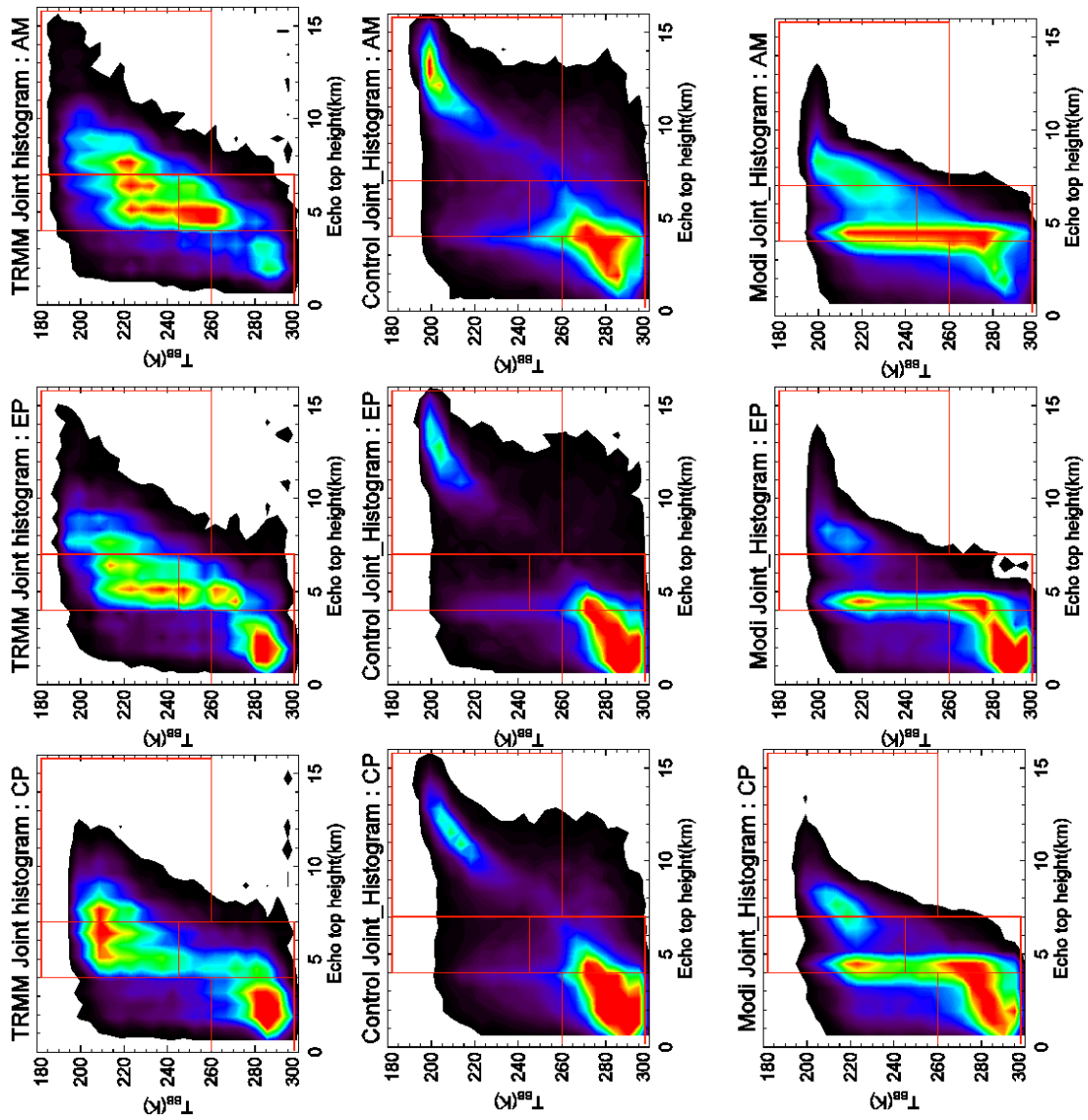


Fig. 3.9: The joint histogram of PTH and TBB of TRMM (left), CON (middle), and MODI (right) for Central Pacific (CP), Eastern Pacific (EP), and America (AM).

We divided the land and ocean areas in tropics to investigate dependency on surface conditions (Fig. 3.10). The joint histogram of ocean area has more shallow precipitation clouds than the land area, which corresponds to the KWAJEX case in the Matsui et al. (2009), whereas the congestus, mid-cold, deep clouds have more frequencies than shallow clouds in the land areas. The strongest convective systems with 16 km echo top height occurred in land areas rather than in ocean areas. These contrasts between the land and ocean areas are found in the results of the modified microphysics. However, CON does not show clear contrasts between them comparing observation and MODI. However, MODI overestimates the fraction of congestus compared to observations. The CFADs of land and ocean areas do not show the same clear gap of structure in the observations (Fig. 3.11). Maximum radar reflectivities in land areas are larger than in ocean areas due to stronger convective systems. MODI shows better structures of CFADs, whereas maximum radar reflectivities are slightly underestimated. One of the probable causes of the underestimation of maximum radar reflectivities is that MODI simulates the small graupel but not the hail. The convective systems in extreme precipitation cases accompany large ice particles with high density like hails. However, MODI does not have hail categories to reproduce these extreme cases.

We investigate the effects of SSTs on the characteristics of the joint histogram structures over ocean areas following Masunaga et al. (2004). According to Masunaga and Kummerow (2006) and Masunaga et al. (2005), shallow precipitation in the joint histograms is linked to the SST range. Both simulations show that the frequencies of shallow precipitations are sensitive to the SST range (Fig. 3.12). It shows a general trend that shallow clouds have the highest probability of occurrence for relatively cold SSTs, while deep convective events take their place for warmer SSTs in previous studies.

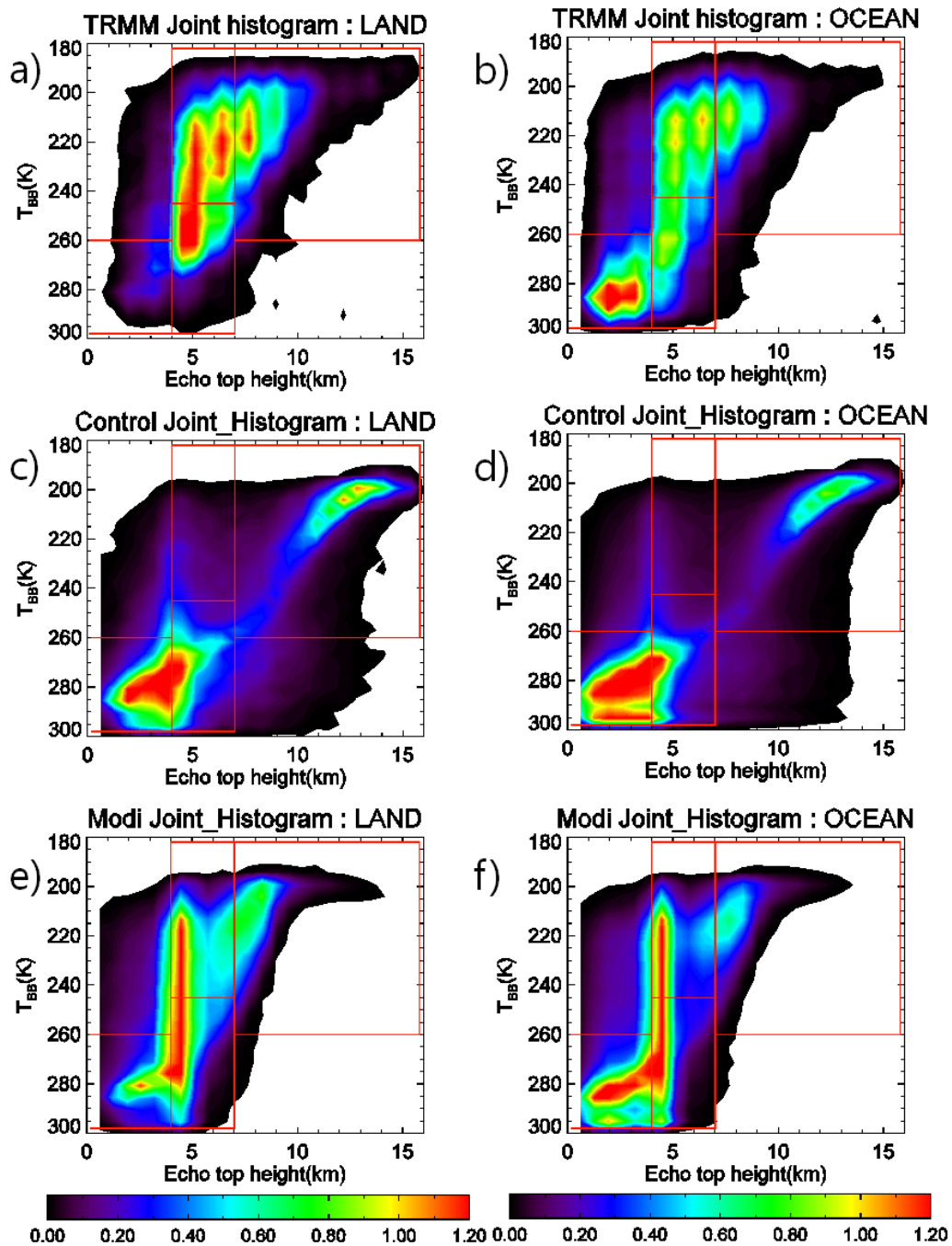


Fig. 3.10: The joint histogram of PTH and TBB over land areas (left) and ocean areas (right) for the TRMM observation (top), CON (middle), and MODI (bottom) for the 2 day simulations.

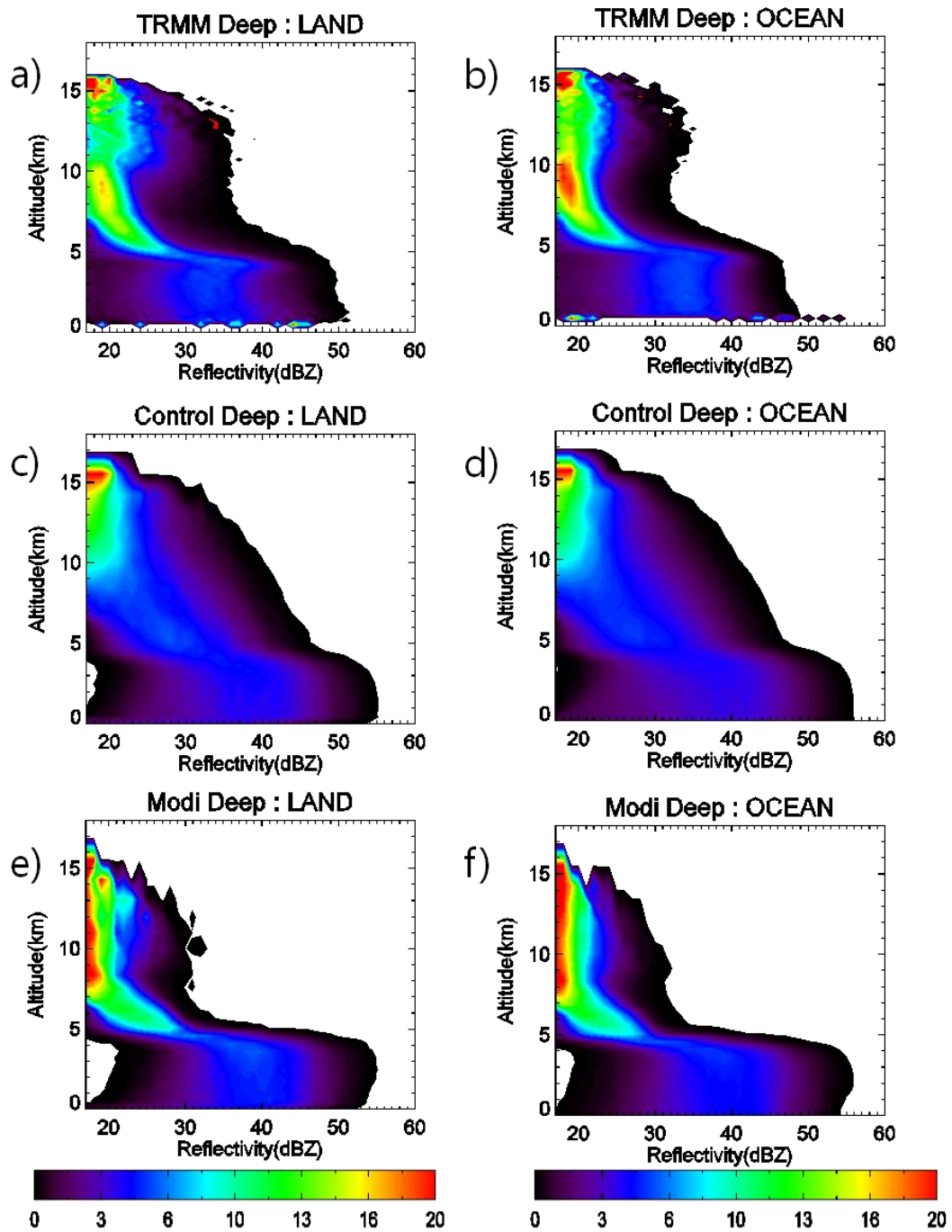


Fig. 3.11: The CFADs of deep clouds over land areas (left) and ocean areas (right) for the TRMM observation (top), CON (middle), and MODI (bottom) for the 2 day simulations.

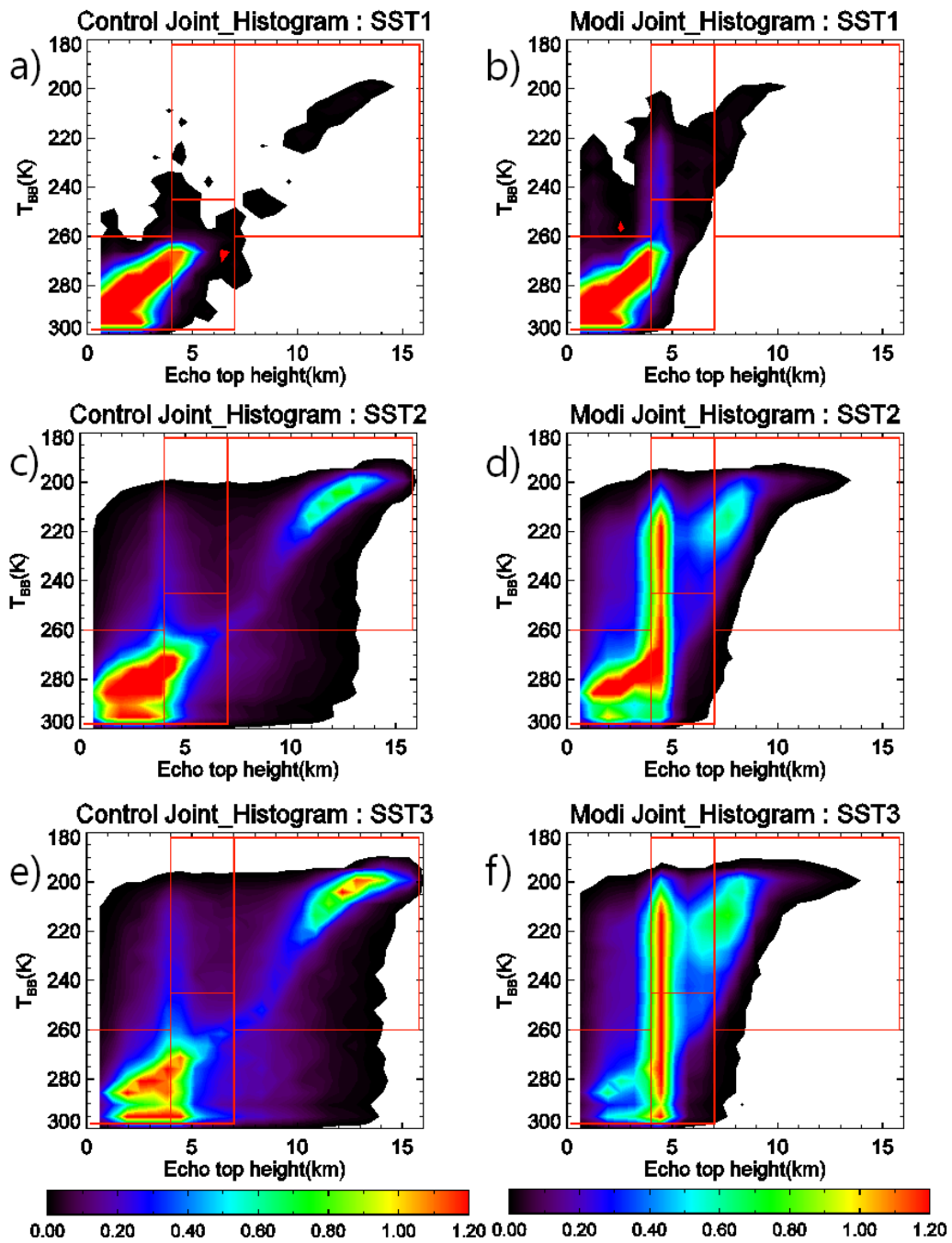


Fig. 3.12: The joint histogram of PTH and TBB of CON (left) and MODI (right) for SST1 (SST < 26°C) (top), SST2 (26°C < SST < 29°C) (middle), and SST3 (SST > 29°C) (bottom) for the 2 day simulations.

There are few studies about the joint histogram using TRMM at middle latitudes. The reason for this is the limitation of the observed range for middle latitudes TRMM data, which include only 36S – 36N degrees. We define the two following middle latitude areas: the southern part (20S – 36S) and the northern part (20N – 36N). In our case, there is a difference in seasons: the northern part is in the summer and the southern part is in the winter. We found that the joint histogram structure is sensitive to the seasonal differences and that this is related to the tropopause height and melting layer height (Fig. 3.9). NICAM reproduces a realistic tropopause height and it simulated the realistic minimum TBB in CON and MODI. The minimum TBB in the northern part is almost 190 K and the minimum TBB in the southern part is 210 K in the observation and in the two simulations. The cloud structure in the northern part is similar to the structure of the tropical results. The minimum TBB and the maximum echo top heights are reduced in the southern part compared to the results in the tropical and northern parts. It is speculated that categorization relies on the tropopause and melting layer height. The lower tropopause and melting layer height shrink diagrams, restrict maximum echo top heights, and lower TBBs.

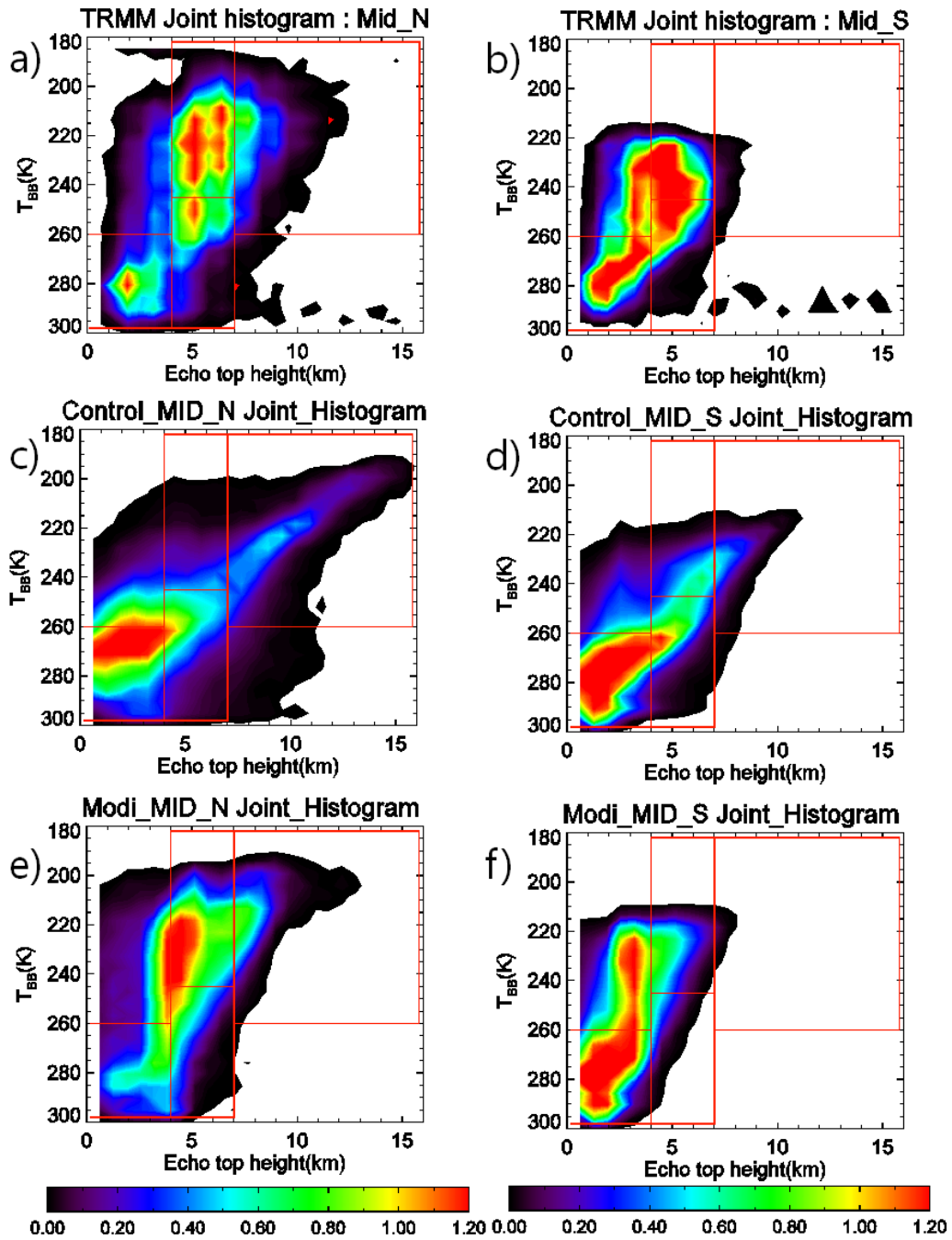


Fig. 3.13: The joint histogram of PTH and TBB over the northern part (20N – 36N) and southern part (36S – 20S) for the TRMM observation (top), CON (middle), and MODI (bottom) for the 2 day simulations.

3.6 Comparisons with CloudSat

We made an additional analysis using CloudSat following Masunaga et al. (2008). They used the two thresholds echo top height of radar reflectivities such as -28 dBZ and 10 dBZ echo top height devised by Stephens and Wood (2007), instead of TBBs and TRMM echo top height. Masunaga et al. (2008) evaluated the cloud properties using this histogram for the dry and wet phases of a MJO system with a microphysics scheme by Grabowski et al. (1998). They found that NICAM does not reproduce the high frequency of 94 GHz radar reflectivities over 6 km. The reason is that 94 dBZ signals tend to be attenuated by ice particles than the lower frequency active sensors of TRMM PR. Thus, it is insensitive to shallow precipitation clouds, overlapped anvil clouds, or thick cirrus clouds. Figure 3.14 show that the structure of the joint histogram by CloudSat is similar structure to that of TBB and TRMM PR, but the fraction of the shallow precipitation is lower than the TRMM joint histogram. The CON with the NSW6 microphysics scheme (Tomita et al. 2008a) shows a closed histogram shape as shown in Masunaga et al. (2008). MODI shows a larger fraction of deep clouds than CON, but mid-cold clouds are overestimated. The CFADs show a clear difference between CON and MODI. CON does not produce radar reflectivities of less than -20 dBZ above 10 km in altitude. A large fraction of the frequencies in observation and MODI are between -28 to -20 dBZ. CON shows weaker maximum radar reflectivities due to the attenuation. However, MODI shows maximum radar reflectivities near 10 km and melting layers near 5 km. The attenuated CFAD radar reflectivities in CON are accompanied by low frequencies of mid-cold and deep clouds. MODI has two peaks of radar reflectivities profiles above 5 and 10 km altitude in CFADs (Fig 3.14f). It corresponds to the two discrete high frequencies at 5 and 10 km in joint histograms (Fig 3.14e). However, CloudSat does not show the clear two peaks in the MODI simulation.

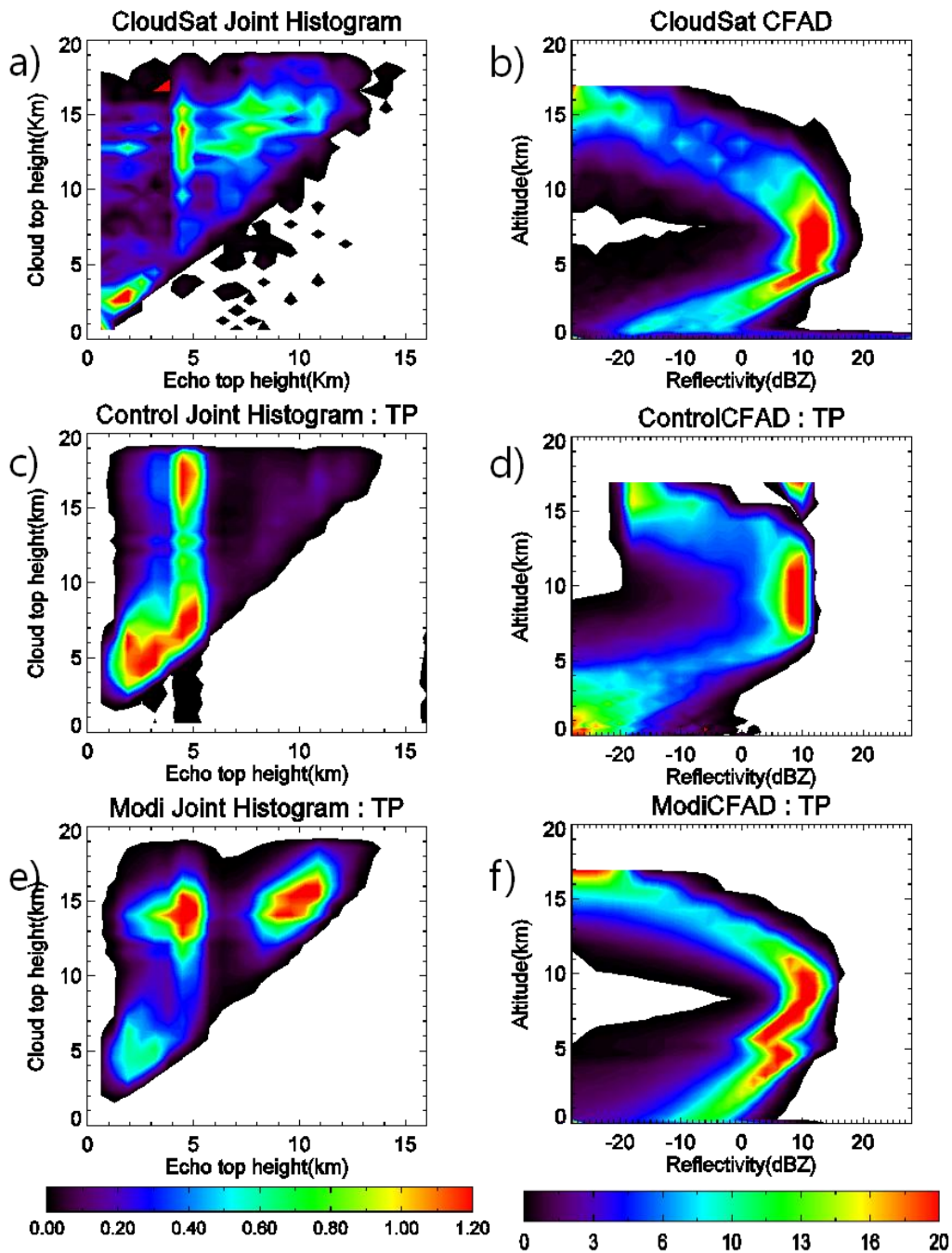


Fig. 3.14: The joint histogram of PTH and CTH calculated from 95GHz radar reflectivities (left) and CFADs of deep clouds of 95GHz radar reflectivities (right) over whole of tropics for the TRMM observation (top), CON (middle), and MODI (bottom) for the 2 day simulations.

3.7 Summary and conclusion

The improved microphysics with a regional cloud system resolving model is tested with a global cloud system resolving model for the entire tropical region and limited middle latitudes covered by TRMM. CON and MODI simulate a realistic horizontal distribution of clouds comparing observed the 11 μm TBB. However, The MODI simulation reproduces larger cloud systems than the CON experiment. The locations of accumulated simulated precipitations are well reproduced compared to TRMM 3B42 data, although the simulations overestimated the accumulated precipitation sizes and amounts. On the large scale, the accumulated precipitation distribution is not sensitive to the modification of the microphysics scheme. The cross section of tropical cyclone Fengshen is evaluated in CON and MODI using TRMM and CloudSat. The clouds of CON are more isolated than MODI. The simulated vertical profiles of 13.8 GHz and 94 GHz signals reduced some biases of radar reflectivities, such as the overestimation of 13.8 GHz radar echo top heights, and the underestimation of 94 GHz maximum radar reflectivity.

The joint histogram of TBB and PTH and CFADs of deep clouds over the entire tropics are similar to the regional results described in chapter 2. The joint histogram of MODI shows similar features to that in Part 2. The fraction of mid-cold and shallow clouds is improved in MODI compared to observations, whereas the fraction of deep clouds is underestimated. The regional differences are found in the tropic. The difference originates from the surface condition of the land and ocean area in the observation; the fraction of shallow clouds is lower in the land areas than in the oceans. The pattern of contrast between land and ocean is similar to observation for both simulations, although the contrast is more evident in MODI than in CON.

Seasonal differences between the southern and northern middle latitudes are found in observation. The joint histogram of the southern part in the winter season is shrank compared to the tropics and the northern part in boreal summer season. We speculate that the differences of tropopause heights and melting layers lead to the seasonal difference in the

joint histogram. We found that the simulation results clearly reproduced the seasonal difference in the joint histogram, similar to the observation.

Finally, an additional analysis using the 94 GHz signals of CloudSat was carried out. The results of this analysis show that MODI improves the joint histogram and CFADs calculated for 94 GHz radar reflectivities.

These results show that the improvement of microphysics scheme in the specific region of the central Pacific Ocean proposed by this study is capable to able to reproduce statistically realistic vertical structures over other areas not only in the tropics but also in the mid latitudes. The results also showed that the simulated CloudSat signals were better when the scheme is improved by using the TRMM data.

4 Remaining Issues

4.1 Introduction

In chapters 2 and 3, the improvement and evaluation of microphysics were studied using satellite data and a satellite simulator. However, cloud properties affect other microwave signals, OLR, and effective radius. In chapter 4, to investigate the effect of cloud properties on other microwave signals, OLR, and effective radius, we introduce the results of additional analyses and discuss about the remaining aspects with the improved microphysics.

T3EF is a three-steps method; we focus only on two of these steps: construction of a joint histogram and the CFADs of deep clouds. In this chapter, we discuss the cumulative probability distribution of polarization corrected 85 GHz microwave signal results for simulations and observation. Low frequency microwave channels such as 19 and 37 GHz are useful to assess surface precipitations in remote sensing. Relatively high frequency microwave channels such as 85 GHz are sensitive to high-density ice particles and small ice particles (Liu and Curry 1996). Matsui et al. (2009) added an additional step for evaluation of the graupel or precipitation ice particles amounts.

OLR is important for the atmospheric energy budget. Clouds play a role on the energy budget both through long and short wave radiations. It is known that OLR is sensitive to high clouds, but relatively insensitive to lower clouds. The latter have cooling effects via reflection of the solar radiation.

Inoue et al. (2008) studied cloud sizes of deep convection simulation of a GCSRM result (Miura et al. 2007) using simulated OLR and observed TBB over the western Central Pacific. The results are close to the MTSAT satellite and NOAA OLR data. It is known that OLR is sensitive to the microphysics scheme. For example, Iga et al. (2007) found that the OLR is dependent on the fall speed of snow. The latitudinal profile of OLR uniformly decreases due to the decrease of the fall speed of snow. These results are similar to other CRMs and GCMs (Wu et al. 1999; Jakob 2002); these studies reported that the OLR is sensitive to the fall speed

of cloud ice. Satoh and Matsuda (2009) investigated the effects of microphysics on high clouds and OLR. Kodama et al. (2010) showed that the high cloud properties and OLR depend on the autoconversion process from cloud ice to snow using CALIPSO data. We found that the global results of OLR are underestimated comparing with NOAA daily OLR data. We discuss how to improve the OLR results in this chapter.

We focused on the size distribution of precipitation particles which is directly related to the sizes of hydrometeors, expressed by their effective radius. The effective radius is associated to the radiation transfer for scattering and absorption processes in clouds and is defined as

$$r_e = \frac{\int_0^\infty r n(r) \pi r^2 dr}{\int_0^\infty n(r) \pi r^2 dr}, \quad (4.1)$$

where r is the cloud radius and $n(r)$ is the number size distribution of the cloud. The effective radius of cloud ice has more uncertainty than the effective radius of cloud water due to non-spherical shapes. In this chapter, we simply assume the spherical shape of cloud ice, snow, and graupel.

The effective radius is retrieved base on the assumption of size distribution and mass dimension relationship. There is some observation data retrieved from satellite data such as CloudSat, CALIPSO and MODIS data (e.g., Nakajima and King, 1990; Wood, 2008; Hagihara et al. 2010). We compare the retrieved effective radius and simulated effective radius of two simulation results.

The data used is explained in section 4.2. In section 4.3, 85 GHz microwave signal results are evaluated and discussed. The zonal averaged OLR are described in section 4.4. The effective radius is evaluated from the retrieved effective radius in section 4.5. The conclusion and discussion are summarized in section 4.6.

4.2 Data

The TMI 85.5-GHz dual-polarization microwave brightness temperature from TRMM 1B11 (Kummerow et al. 1998) is used to construct cumulative probability distributions of polarization corrected brightness temperature (PCT85). PCT85 is introduced by (Kidd 1988) in order to compensate for the inhomogeneity of surface emissivity:

$$\text{PCT85} = T_{85V} + a(T_{85V} + T_{85H}), \quad (4.2)$$

where T_{85V} and T_{85H} are the brightness temperatures from the vertical and horizontal polarization channels at 85 GHz, respectively, and $a=0.8$, which ensures that the inhomogeneity in surface emission.

NOAA daily interpolated OLR data is used for comparison with OLR properties (Liebmann and Smith 1996). This data is filled with temporal and spatial interpolation with 2.5 degree horizontal resolution.

Hagihara et al. (2010) developed cloud masks, particle type, and cloud microphysical information data from combined CloudSat/CALIPSO data set (herein Hagihara data). The data is constructed by regriding CALIOP 532 and 1064 nm attenuated backscattering coefficients into the sampling volume of the CPR 94 GHz radar reflectivity. The Hagihara data is based on the Okamoto et al. (2003) algorithm. Okamoto et al. (2003) developed the retrieval algorithm based on the differences in effective radius between radar and lidar with the same ice water content. The effective radius is retrieved from two look-up tables made by radar reflectivities from CloudSat and back-scattering coefficients from CALPSIO. The altitude of the grid centers ranges from 120 to 19,800 m in the Hagihara data.

The effective radius data is also used from MODIS level 2 granule cloud products onboard Terra platforms. The effective radius and cloud optical depth are retrieved based on the reflected radiations at two wavelength bands for warm clouds (King et al. 1992). The ice effective radius is needed for crystal shapes and habits information, as it makes for the discrepancy between the observation and simulation. The latest MODIS product, collection 5 data, is used in this study (Yang et al. 2007).

4.3 The cumulative probability distributions of PCT85

Figure 4.1 shows the cumulative probability distributions of PCT85 among CON, MODI, and observation for shallow, congestus, mid-cold, and deep clouds. The cumulative probability distributions of PCT85 for shallow and congestus in both CON and MODI are in good agreement with observation. However, the mid-cold and deep clouds have a strong depression in simulations in contrast with TRMM observations. The distributions of MODI for mid-cold and deep clouds are similar to observations. Overall, the cumulative probability distributions of PCT85 for mid-cold and deep clouds are not sensitive compared to previous result such as the joint histograms and CFADs of deep clouds.

The possible reasons may be as follows. First, it could be due to an overestimation of the scattering of rain. According to Biggerstaff et al. (2005), the rain and cloud water are not sensitive to 85GHz microwave signals. Figure 4.1 shows the effects of ice phase particles (e.g. cloud ice, snow, graupel) and water phase particles (e.g. cloud water and rain). We tested the effects of ice and water phase on the distribution of the PCT85 using sensitivity tests by turning off these hydrometeors. We found that the main depression sources are ice phase hydrometeors, but liquid phase hydrometeors also have depression for PCT85. It means that the rain and cloud water are sensitive to 85GHz microwave signals.

Second, it may be a result of an underestimation of melting layer effects. According to Oslon et al. (2001), when the bright band is present, the 85 GHz TBB increases. In this study, the melting layer effects are not considered, so it makes for lower TBB in the simulations.

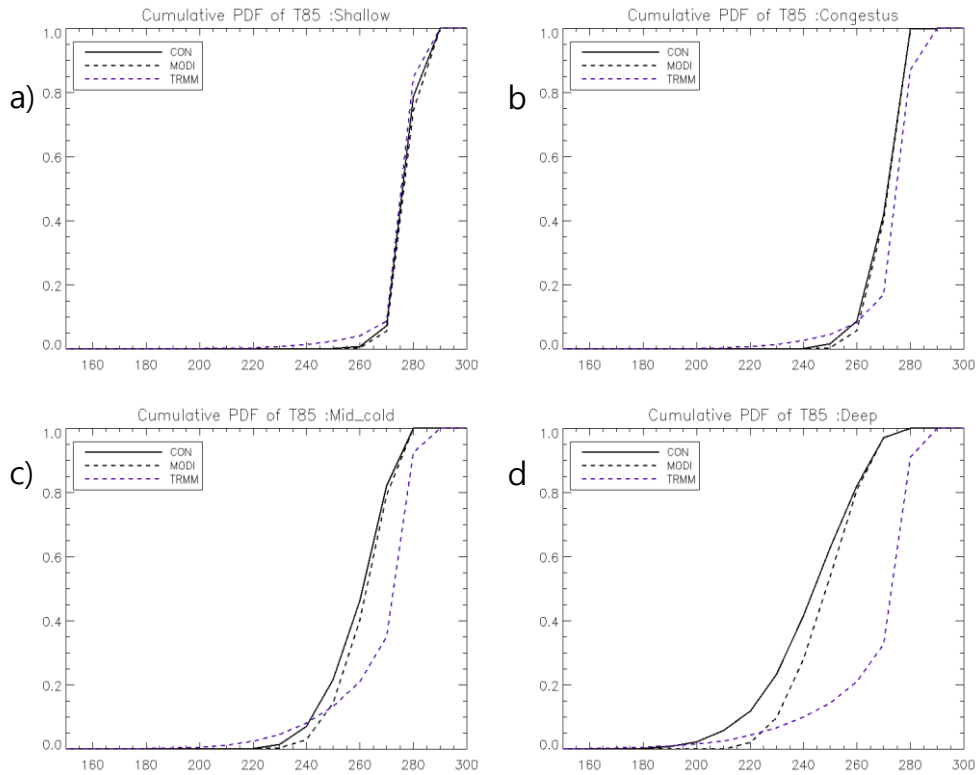


Fig. 4.1: The cumulative probability distributions of PCT85 for shallow clouds (a), congestus (b), mid-cold (c), and deep clouds (d) over the entire tropics.

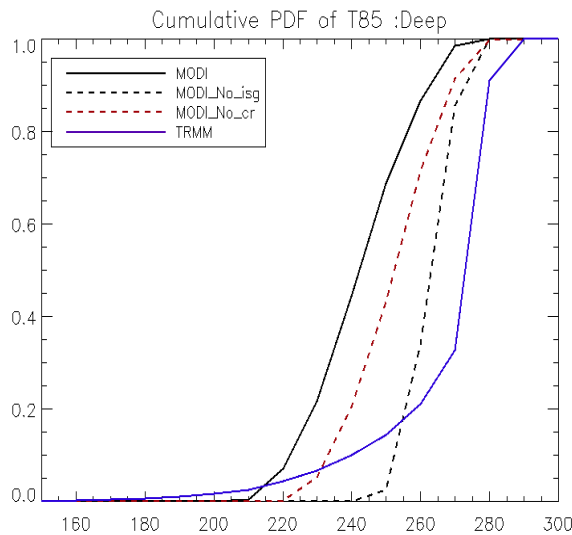


Fig. 4.2: The cumulative probability distributions of PCT85 for shallow deep clouds over the entire tropics for sensitivity test for no ice phased and no water phased hydrometeors.

4.4 OLR

We compare the zonal averaged OLR between NOAA daily data, CON, and MODI (Fig. 4.3). The OLR of CON reproduces the larger OLR of almost 10 Wm^{-2} , whereas the OLR of MODI is lower compared to observation, at almost 5 Wm^{-2} (Table 4.1). The underestimation of MODI is dominant over the tropic and northern hemisphere. Both simulations overestimate the OLR near southern pole areas from 70S to 90S. There are some solutions to resolve the OLR underestimation problem. The first one is to change the fall speed of snow or to introduce the fall speed of cloud ice. In this study, we did not consider the terminal velocity of cloud ice. When we took into account the terminal velocity of cloud ice based on Heymsfield and Donner 1990 using a regional NICAM, the terminal velocity was calculated as

$$V_{ti} = 3.29(\rho q_i)^{0.16}, \quad (4.3)$$

where ρ is air density in kg m^{-3} , q_i is mixing ratio of cloud ice in kg kg^{-1} and V_{ti} in m s^{-1} . It increases the approximate 10 Wm^{-2} of the domain average OLR of tropical central Pacific areas.

Second, the autoconversion process of cloud ice affects the OLR according to Kodama et al. (2010). The autoconversion process, P_{SAUT} is expressed as

$$P_{SAUT} = \beta(q_i - q_{icrt}) \quad \text{for } q_i > q_{icrt}, \quad (4.4)$$

$$P_{SAUT} = 0 \quad \text{for } q_i < q_{icrt} \quad (4.5)$$

where $\beta = 10^{-3} \exp(\gamma_{\text{saut}} (T - T_0))$, $\gamma_{\text{saut}} = 0.025$, T is the temperature, $T_0 = 273.15 \text{ K}$, and q_{icrt} is the critical value of the autoconversion. The q_{icrt} means starting mixing ratio of collision and coalescence process among cloud ices. It is difficult to determine the appropriate value. They found the autoconversion process in a GCSRМ change significantly from 187 to 266 W m^{-2} of latitudinal mean OLR (Kodama et al. 2010, Table 3).

Third, the radiation scheme has a fixed effective radius for both cloud ice and snow, in order to cut down calculation time. When we change these default values, we expect to get

the increased OLR.

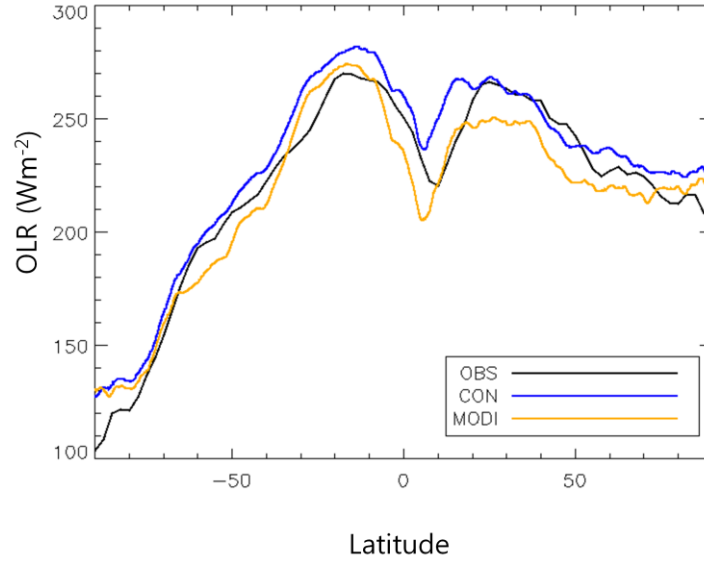


Fig. 4.3: Zonal averaged OLR for the NOAA daily observation, CON, and MODI for the 2 day simulations.

Table 4.1. Global and temporal averages of OLR for 2days among CON, MODI, and daily NOAA OLR.

Experiment	CON	MODI	NOAA OLR
OLR	229.1 W m ⁻²	215.4 W m ⁻²	220.7 W m ⁻²

4.5 Evaluations of effective radius

The effective radiuses are analyzed using the Hagihara data and MODIS data. Figure 4.4 shows the CFAD of effective radius of the Hagihara data versus simulated effective radiuses. In observation, the range of effective radius is concentrated near $80 \mu\text{m}$ over 13 km and the effective radius increased to $150 \mu\text{m}$ near 6 km of altitude. The peak of effective radius is located at 8 km and both simulation reproduce the same pattern of observation. However, CON shows that the CFADs are discrete near 12 km altitude, and that the effective radius is overestimated, almost 2 times more compared to the observation. MODI has a continuous distribution similar to the observation of CFADs. The maximum effective radius is overestimated at $300 \mu\text{m}$ near 8 km . The effective radiuses of the two simulations are underestimated for altitudes lower than 5 km .

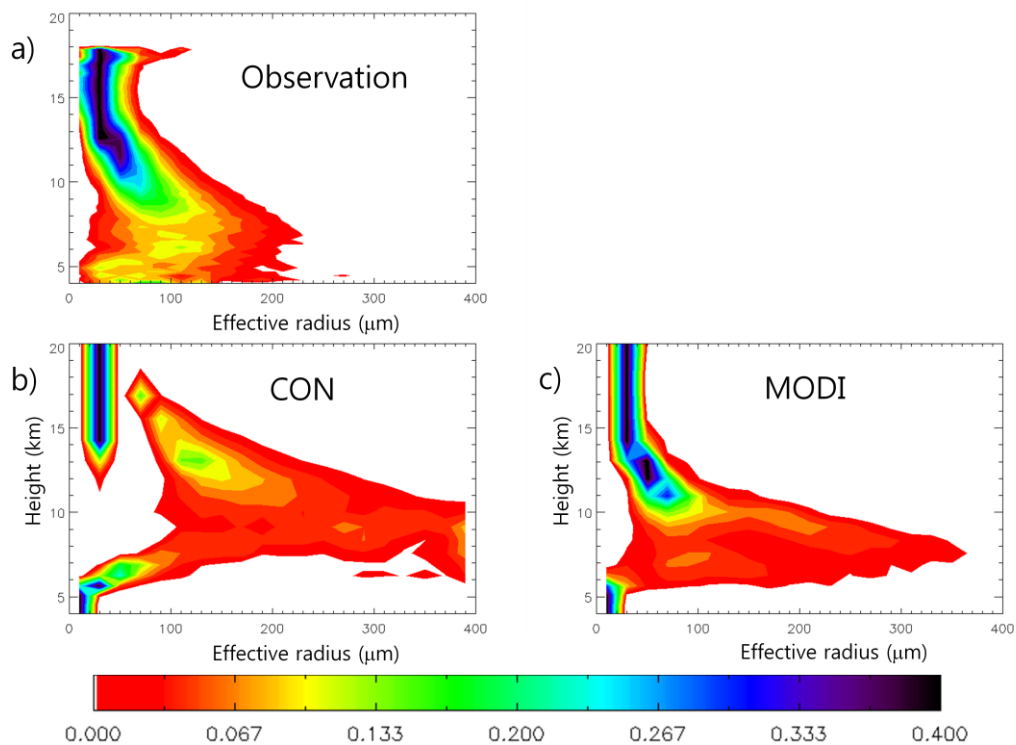


Fig. 4.4: The CFADs of effective radius of Hagihara data (a), and CON (b), and MODI (c) over the entire tropics for the 2 day simulations.

Second, we evaluate the effective radius using MODIS data. The MODIS data is only capable to detect the effective radius of the upper layer of clouds. The effective radius of MODIS shows that the effective radius increases as the TBB increases. The standard deviation is increased from 270 K to 300 K. Both simulations do not show these kinds of patterns due to mono-size destitution of cloud ice. According to Yuan and Li (2010), this dependence of TBB originates from temperature, humidity and cloud freezing height of cloud ice in the thermodynamic view. The homogeneous nucleation process of cloud ice and the updraft velocity also affect it. We focused on the size distribution of precipitation hydrometeors, so it is insensitive to the upper clouds' effective radius. Future improvements of microphysical processes are required that could take into consideration for the size distribution of cloud ice and cloud water including nucleation, sedimentation, and collection process.

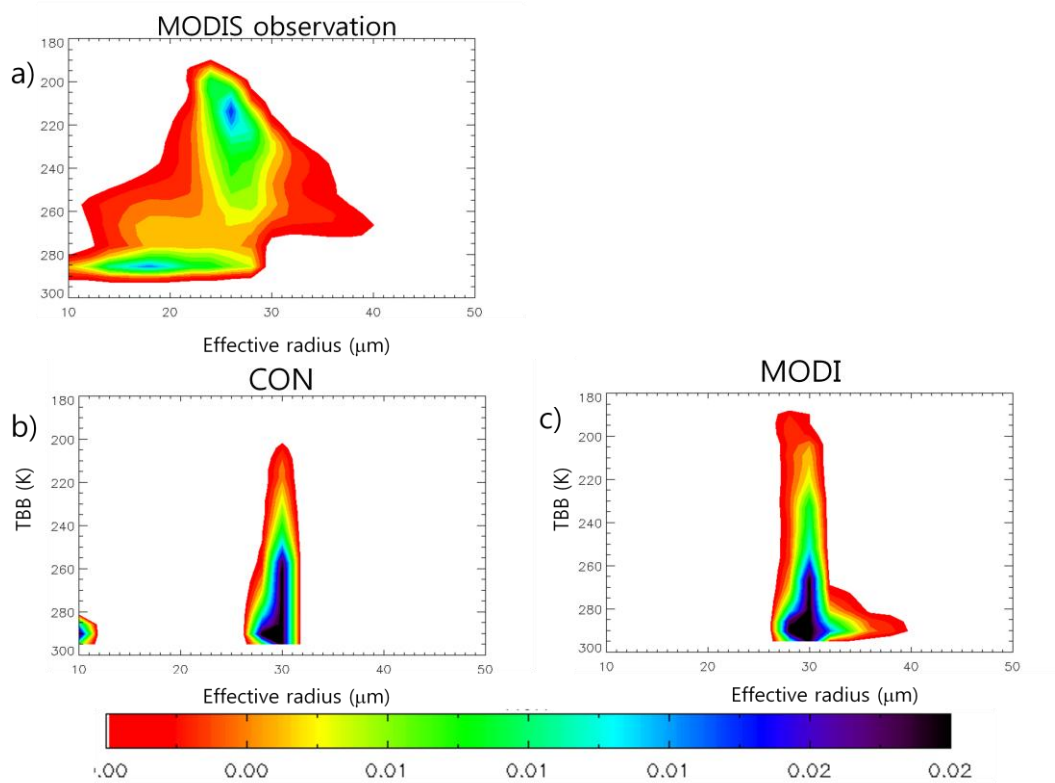


Fig. 4.5: The joint histogram of effective radius and TBB of MODIS data (a), and CON (b), and MODI (c) over the entire tropics for the 2 day simulations.

4.6 Summary and conclusion

In this chapter, we presented additional analysis about PCT85, OLR, and effective radius using two different microphysics schemes.

We performed the third step of T3EF, which includes construction of the cumulative probability distributions of PCT85. The results show a similar distribution of shallow and congestus clouds compared to simulations and observation. Both microphysics schemes underestimate the PCT85 in mid-cold and deep clouds. We speculate that the overestimation of liquid phase hydrometeors and the lack of consideration for the melting layer effect are possible reasons.

We evaluated the observed OLR with coarse temporal and spatial resolutions. The longitudinal average OLR of MODI underestimates the observed one compared to the CON results. We think that other microphysical processes are needed to improve the OLR, such as taking into account cloud ice fall speed and the autoconversion process from cloud ice to snow, since the radiation scheme has fixed parameters for snow and cloud ice. It is also needed to check the results.

Finally, we assess the vertical distribution of effective radius and the effective radius in upper clouds using Hagihara and MODIS data. The vertical distribution of effective radius in MODI is improved compared to CON. The upper part of the effective radius is similar to that of CON and it does not show the temperature dependence of TBB like the observation.

We attempted to improve the cloud statistics based on the precipitating hydrometeors. However, it is the limitation about improvement of PCT85 and the effective radius in the upper part. It is believed to improve the results by improvement of a satellite simulator and advanced microphysics. Additionally, the cloud and precipitation systems are likely to be also affected by various factors such as grid configurations, convective initiation, and turbulence parameterizations. We are looking forward to investigate the effect of these components in the future.

5 General conclusions

The mesoscale convective systems are important for the study about vertical structures in mesoscale convective systems of tropical precipitation clouds. The single moment bulk microphysics of a cloud system resolving model is evaluated and improved with a satellite simulator.

We evaluated the cloud properties such as horizontal cloud size distributions and precipitation cloud statistics base on Matsui et al. (2009) over the tropical Pacific Ocean for 30 days. We found the biases in cloud statistics using the brightness temperature and precipitating cloud top height based and CFADs on the TRMM satellite data. We focus on the improvement of microphysics based on the precipitation hydrometeor size distribution. We found that the size distributions of precipitating hydrometeors have an impact on the joint histogram and CFADs of deep convective systems according to several sensitivity tests.

Before the sensitivity tests, the ice nucleation and ice deposition process were introduced and the accretion process of graupel with snow and cloud ice was turned off, these modifications increased snow amount and reduced graupel amount. The physical bases are more compressive cloud ice physical process and the reduction of unrealistic graupel amount than the old method. The horizontal distribution of the accumulated precipitation is well organized in the tropical open ocean. The increased snow makes the more stratiform precipitation and anvil clouds. And it reproduced the close OLR to observation than an old method. However, these approaches did not improve the bias of T3EF.

First, the parameterization of the snow size distribution was evaluated. It is affected by the aggregation/autoconversion processes. It affects the distributions of the frequencies of deep clouds in the joint histogram. While the exponential size distribution with fixed N_0 reproduces large size of snow in the upper troposphere in the control run and it does not consider aggregation processes, the Field et al. (2005) method reduced positive bias in the joint histogram, which have the bimodal distribution representing the physics relating to

aggregation (exponential part) and diffusional growth or loss and possibly including the effects of new particle production (power law part). The Mass-dimension relationship for snow affects the average radar reflectivity of the CFADs in deep clouds.

The maximum radar reflectivity is affected by riming and the density of graupel. The increased N_0 of graupel reproduced the realistic maximum radar reflectivity of CFADs in a regional CSRM. However, there is the underestimation of maximum radar reflectivity of CFAD in comparison with the TRMM data over the whole tropic.

Taking into account difference of rain size distributions between the convective and stratiform precipitation, we improve the fraction of frequencies related to stratiform precipitation clouds in the joint histogram. The MP distribution represents only superior size distributions in the convective and shallow precipitation cases, while there are limitations to represent them in the stratiform precipitation which compared with Tokay and Short (1996). The new method used the two different approaches for stratiform and the other precipitations. It would reproduce the more realistic climatological size distribution of rain. However, it is necessary to refine the criterion between convective precipitation and stratiform precipitation. We found the preferable size distributions comparing TRMM and these size distributions reproduce the improved cloud statistics, accumulated precipitation and OLR comparing observations.

The analysis of two different microphysics schemes is expanded using a GCSRM over the whole of tropics and middle latitude covered by TRMM. The distributions of $11 \mu\text{m}$ brightness temperature are different between the two microphysics schemes, whereas both microphysics reproduced almost the same accumulated precipitation distributions. Regional differences are found in simulations and observations in the joint histogram. The improved microphysics shows better results for the joint histogram and CFADs of deep clouds in the tropical region and even in middle latitude areas, whereas mid-cold clouds are increased compared to the control run.

Additional analyses are performed on the 85 GHz microwave signals, OLR, and effective radius. The improved microphysics has little impact on the cumulative probability

distribution of PCT85. Furthermore, OLR is underestimated in the improved microphysics compared to the NOAA daily OLR. The vertical distributions of effective radius in the modified microphysics are better than in the control run. The effective radius in the upper part of clouds has a big gap between simulations and observations and it does not contain observed features depending on brightness temperature.

The satellite data are used to investigate precipitation and cloud properties. This study aimed to improve the statistics of precipitation clouds based on the T3EF, we successfully show that the improvement of microphysics in the regional scale is capable to advance the results of global cloud simulations. However, the TRMM data has limitation of coverage from 36S to 36N. The Global Precipitation Measurement (GPM) mission started to provide the next generation global observations of rain and snow based on the success of the TRMM, the GPM concept centers on the deployment of a “Core” satellite carrying an advanced radar and radiometer system to measure precipitation from space and serve as a reference standard to unify precipitation measurements from a constellation of research and operational satellites. The GPM Core Observatory consists of a Ka band precipitation radar operating at 35.5 GHz and a Ku band precipitation radar operating at 13.6 GHz having an almost same frequency of the TRMM PR data (13.8 GHz). The GPM Core Observatory extends coverage to higher latitudes to provide a global view of precipitation. Recently, the GPM Core Observatory launched on 27 February 2014 and the data would be available soon for scientific researches. If these data were used, it would be possible to evaluate and investigate the cloud statistics in higher latitudes using T3EF.

There are more advanced microphysics schemes, such as multi-moment or bin microphysics schemes that reproduce diverse size distributions. However, to interpret the results of such advanced schemes comparing the satellite data, we need to understand how the size distributions of hydrometeors affect radiances from the cloud properties in numerical simulations. In fact, we found that the parameters assumed in the single-moment microphysical scheme control the cloud and precipitation properties in this study.

However, a single moment scheme has limitation to represent explicitly comprehensive

microphysical processes such as aerosol indirect effects and aggregation. The double-moment scheme is now implemented in a global cloud system resolving model. We would expand to evaluate a global cloud system resolving simulations with a single and double moment microphysics scheme using TRMM and CloudSat. Comparisons of microphysics schemes of differing complexity will reveal further important factors in the size distributions using the methods proposed in this study. The double moment and bin microphysics do not need to parameterization of size distribution like a single bulk microphysics. The method is more physical base than a single moment scheme. However, it is difficult to interpret the results because there are more freedoms to control size distribution by many microphysical processes. We think the first step of improving approaches in bin or double moment schemes is to look for the poor physical process, which could not reproduce the climatological ranges of simulated average size distribution in the satellite's point of view by sensitivity tests of microphysical parameters. If the results were not better than a single moment scheme, they would be compared by size distribution in a single moment scheme and investigated by sensitivity tests of physical processes. We believe these studies would give the information and criterion of climatological size distributions in order to evaluate them of the more advance microphysics for a long-term and large scale simulation.

In the future, the evaluation would be expanded to investigate non-spherical shapes of ice phased hydrometeors. The cloud ice, snow, and graupel have non-spherical shapes in the real world. There are some uncertainties of the radiative properties such as scattering and emission depending on shapes of ice phase hydrometeors. We would implement the parameterization of non-spherical shape assumptions in ice phase particles and investigate the radiative effect on them. The results would be evaluated with the depolarization ratio data of the CALIPSO data, because these data have the information of 2D and 3D shapes of ice particles (Yoshida et al. 2010).

References

- Blossey, P. N., C. S. Bretherton, J. Cetrone, and M. Kharoutdinov, 2007: Cloud-resolving model simulations of KWAJEX: Model sensitivities and comparisons with satellite and radar observations. *J. Atmos. Sci.*, **64**, 1488–1508.
- Bodas-Salcedo, A., M. J. Webb, S. Bony, H. Chepfer, J.-L. Dufresne, S. A. Klein, Y. Zhang, R. Marchand, J. M. Haynes, R. Pincus, and V. O. John, 2011: COSP satellite simulation software for model assessment. *Bull. Amer. Meteor. Soc.*, **91**, 1023–1043.
- Bohren, C. F., and L. J. Battan, 1982: Radar backscattering of microwaves by spongy ice spheres. *J. Atmos. Sci.*, **39**, 2623–2628.
- Bryan, G. H., and H. Morrison, 2012: Sensitivity of a simulated squall line to horizontal resolution and parameterization of microphysics. *Mon. Wea. Rev.*, **140**, 202–225.
- Caine, S., T. P. Lane, P. T. May, C. Jakob, S. T. Siems, M. J. Manton, and J. Pinto, 2013: Statistical assessment of tropical convection-permitting model simulations using a cell-tracking algorithm. *Mon. Wea. Rev.*, **141**, 557–581.
- Carbone, R. E., J. D. Tuttle, D. A. Ahijevych, and S. B. Trier, 2002: Inferences of predictability associated with warm season precipitation episodes. *J. Atmos. Sci.*, **59**, 2033–2056.
- Cheng, W. Y. Y., and W. R. Cotton, 2004: Sensitivity of a cloud-resolving simulation of the genesis of a mesoscale convective system to horizontal heterogeneities in soil moisture initialization. *J. Hydrometeorol.*, **5**, 934–958.
- Chepfer, H., S. Bony, D. Winker, M. Chiriaco, J. L. Dufresne, and G. Seze, 2008: Use of CALIPSO lidar observations to evaluate the cloudiness simulated by a climate model. *Geophys. Res. Lett.*, **35**, L15704.
- Chepfer, H., and Coauthors, 2010: The GCM-Oriented CALIPSO Cloud Product (CALIPSO-GOCCP). *J. Geophys. Res.*, **115**, D00H16.
- Clark, T. L., 1973: Numerical Modeling of Dynamics and Microphysics of Warm Cumulus Convection. *J. Atmos. Sci.*, **30**, 857–878.

- Cohen, C., and E. W. McCaul, 2006: The sensitivity of simulated convective storms to variations in prescribed single-moment microphysics parameters that describe particle distributions, sizes, and numbers. *Mon Wea. Rev.*, **134**, 2547-2565.
- Dawson, D. T., M. Xue, J. A. Milbrandt, and M. K. Yau, 2010: Comparison of Evaporation and Cold Pool Development between Single-Moment and Multimoment Bulk Microphysics Schemes in Idealized Simulations of Tornadoic Thunderstorms. *Mon. Wea. Rev.*, **138**, 1152-1171.
- Delanoe, J., R. J. Hogan, R. M. Forbes, A. Bodas-Salcedo, and T. H. M. Stein, 2011: Evaluation of ice cloud representation in the ECMWF and UK Met Office models using CloudSat and CALIPSO data. *Q. J. R. Meteorol. Soc.*, **137**, 2064–2078.
- Fabry, F., and W. Szyrmer, 1999: Modeling of the melting layer. Part II: Electromagnetic. *J. Atmos. Sci.*, **56**, 3593–3600.
- Field, P. R., R. J. Hogan, P. R. A. Brown, A. J. Illingworth, T. W. Choullarton, and R. J. Cotton, 2005: Parametrization of ice-particle size distributions for mid-latitude stratiform cloud. *Q. J. R. Meteorol. Soc.*, **131**, 1997–2017.
- Garnett, J. M., 1904: Colours in Metal Glasses and in Metallic Films. *Proceedings of the Royal Society of London*, **73**, 443-445.
- Gilmore, M. S., J. M. Straka, and E. N. Rasmussen, 2004: Precipitation uncertainty due to variations in precipitation particle parameters within a simple microphysics scheme. *Mon. Wea. Rev.*, **132**, 2610–2627.
- Guichard, F., and Coauthors, 2004: Modelling the diurnal cycle of deep precipitating convection over land with cloud-resolving models and single-column models. *Q. J. Roy Meteor Soc.*, **130**, 3139-3172.
- Gunn, K. L. S., and J. S. Marshall, 1958: The distribution with size of aggregate snowflakes. *J. Meteorol.*, **15**, 452–461.
- Hagihara, Y., H. Okamoto, and R. Yoshida, 2010: Development of a combined CloudSat-CALIPSO cloud mask to show global cloud distribution. *J. Geophys. Res.*, **115**, 1984–2012.

- Ham, S. H., B. J. Sohn, S. Kato, and M. Satoh, 2013: Vertical structure of ice cloud layers from CloudSat and CALIPSO measurements and comparison to NICAM simulations. *J. Geophys. Res.*, **118**, 9930-9947.
- Hashino, T., and G. J. Tripoli, 2007: The spectral ice habit prediction system (SHIPS). part 1: Model description and simulation of the vapor deposition process. *J. Atmos. Sci.*, **64**, 2210-2237.
- Hashino, T., M. Satoh, Y. Hagihara, T. Kubota, T. Matsui, T. Nasuno, and H. Okamoto 2013: Evaluating cloud microphysics from NICAM against CloudSat and CALIPSO. *J. Geophys. Res.*, **118**, 7273–7292.
- Heymsfield, A. J., P. Field, and A. Bansemer, 2008: Exponential size distributions for snow. *J. Atmos. Sci.*, **65**, 4017–4031.
- Hong, S.-Y., J. Dudhia, and S.-H. Chen, 2004: A revised approach to ice microphysical processes for the bulk parameterization of clouds and precipitation. *Mon. Wea. Rev.*, **132**, 103–120.
- Hong, S. Y., K. S. S. Lim, Y. H. Lee, J. C. Ha, H. W. Kim, S. J. Ham, and J. Dudhia, 2010: Evaluation of the WRF double-moment 6-class microphysics scheme for precipitating convection. *Adv Meteorol.*, Article ID 707253
- Houze, R. A., P. V. Hobbs, P. H. Herzegh, and D. B. Parsons, 1979: Size distributions of precipitation particles in frontal clouds. *J. Atmos. Sci.*, **36**, 156–162.
- Houze Jr, R. A., 1994: *Cloud dynamics*. Vol. 53, Academic press.
- Houze, R. A., S. S. Chen, D. E. Kingsmill, Y. Serra, and S. E. Yuter, 2000: Convection over the Pacific warm pool in relation to the atmospheric Kelvin-Rossby wave. *J. Atmos. Sci.*, **57**, 3058-3089.
- Iga, S. I., H. Tomita, Y. Tsushima, and M. Satoh, 2011: Sensitivity of Hadley Circulation to Physical Parameters and Resolution through Changing Upper-Tropospheric Ice Clouds Using a Global Cloud-System Resolving Model. *J Climate*, **24**, 2666-2679.
- Iguchi, T., T. Nakajima, A. P. Khain, K. Saito, T. Takemura, and K. Suzuki, 2008: Modeling the influence of aerosols on cloud microphysical properties in the east Asia region using

- a mesoscale model coupled with a bin-based cloud microphysics scheme. *J. Geophys. Res.*, **113**, D14215.
- Inoue, T., M. Satoh, H. Miura, and B. Mapes, 2008: Characteristics of cloud size of deep convection simulated by a global cloud resolving model over the western tropical pacific. *J. Meteorol. Soc. Jpn.*, **86**, 1–15.
- Inoue, T., M. Satoh, Y. Hagihara, H. Miura, and J. Schmetz, 2010: Comparison of high-level clouds represented in a global cloud system-resolving model with CALIPSO/CloudSat and geostationary satellite observations. *J. Geophys. Res.*, **115**, D00H22.
- Janowiak, J. E., R. J. Joyce, and Y. Yarosh, 2001: A real-time global half-hourly pixel-resolution infrared dataset and its applications. *Bull. Amer. Meteor. Soc.*, **82**, 205–217.
- Khain, A., and B. Lynn, 2009: Simulation of a supercell storm in clean and dirty atmosphere using weather research and forecast model with spectral bin microphysics. *J. Geophys. Res.*, **114**, D19209.
- Khairoutdinov, M., and Y. Kogan, 2000: A new cloud physics parameterization in a large-eddy simulation model of marine stratocumulus. *Mon. Wea. Rev.*, **128**, 229–243.
- King, M. D., Y. J. Kaufman, W. P. Menzel, and D. Tanre, 1992: Remote-Sensing of Cloud, Aerosol, and Water-Vapor Properties from the Moderate Resolution Imaging Spectrometer (Modis). *Ieee Tran. Geosci. Remote Sens.*, **30**, 2-27.
- Knight, C. A., W. A. Cooper, I. R. Breed, I. R. Paluch, P. L. Smith, and G. Vali, 1982: *Microphysics*. Vol. 1, Colorado Associated University Press in association with the National Center for Atmospheric Research.
- Kodama, C., A. T. Noda, and M. Satoh, 2012: An assessment of the cloud signals simulated by NICAM using ISCCP, CALIPSO, and CloudSat satellite simulators. *J. Geophys. Res.*, **117**, D12210.
- Kummerow, C., W. Barnes, T. Kozu, J. Shiue, and J. Simpson, 1998: The Tropical Rainfall Measuring Mission (TRMM) sensor package. *J. Atmos Ocean Tech*, **15**, 809-817.
- Lang, S. E., W.-K. Tao, R. Cifelli, W. Olson, J. Halverson, S. Rutledge, and J. Simpson, 2007: Improving simulations of convective systems from TRMM LBA: easterly and westerly

- regimes. *J. Atmos. Sci.*, **64**, 1141–1164.
- Lang, S. E., W.-K. Tao, X. Zeng, and Y. Li, 2011: Reducing the biases in simulated radar reflectivities from a bulk microphysics scheme: tropical convective systems. *J. Atmos. Sci.*, **68**, 2306–2320.
- Li, X., W.-K. Tao, A. P. Khain, J. Simpson, and D. E. Johnson, 2009: Sensitivity of a cloud-resolving model to bulk and explicit bin microphysical schemes. Part II: Cloud microphysics and storm dynamics interactions. *J. Atmos. Sci.*, **66**, 22–40.
- Li, Y., E. J. Zipser, S. K. Krueger, and M. A. Zulauf, 2008: Cloud-resolving modeling of deep convection during KWAJEX. Part I: Comparison to TRMM satellite and ground-based radar observations. *Mon. Wea. Rev.*, **136**, 2699–2712.
- Lim, K.-S. S., and S.-Y. Hong, 2010: Development of an effective double-moment cloud microphysics scheme with prognostic cloud condensation nuclei (CCN) for weather and climate models. *Mon. Wea. Rev.*, **138**, 1587–1612.
- Lin, Y.-L., R. D. Farley, and H. D. Orville, 1983: Bulk parameterization of the snow field in a cloud model. *J. Clim. Appl. Meteor.*, **22**, 1065–1092.
- Lin, Y. L., and B. A. Colle, 2011: A new bulk microphysical scheme that includes riming intensity and temperature-dependent ice characteristics. *Mon Wea. Rev.*, **139**, 1013–1035.
- Locatelli J. D., and P. V. Hobbs, 1974: Fall speeds and masses of solid precipitation particles. *J. Geophys. Res.*, **79**, 2185–2197.
- Luo, Y., Y. Wang, H. Wang, Y. Zheng, and H. Morrison, 2010: Modeling convective-stratiform precipitation processes on a Mei-Yu front with the weather research and forecasting model: comparison with observations and sensitivity to cloud microphysics parameterizations. *J. Geophys. Res.*, **115**, D18117.
- Lynn, B. H., A. P. Khain, J. Dudhia, D. Rosenfeld, A. Pokrovsky, and A. Seifert, 2005: Spectral (Bin) microphysics coupled with a mesoscale model (MM5). Part I: Model description and first results. *Mon. Wea. Rev.*, **133**, 44–58.
- Maki, M., T. D. Keenan, Y. Sasaki, and K. Nakamura, 2001: Characteristics of the raindrop size distribution in tropical continental squall lines observed in Darwin, Australia. *J.*

- Appl. Meteorol.*, **40**, 1393–1412.
- Masunaga, H., and C. D. Kummerow, 2006: Observations of tropical precipitating clouds ranging from shallow to deep convective systems. *Geophys. Res. Lett.*, **33**, L16805.
- Masunaga, H., M. Satoh, and H. Miura, 2008: A joint satellite and global cloud-resolving model analysis of a Madden-Julian oscillation event: model diagnosis. *J. Geophys. Res.*, **113**, D17210.
- Masunaga, H., T. Matsui, W.-K. Tao, A. Y. Hou, C. D. Kummerow, T. Nakajima, P. Baur, W. S. Olson, M. Sekiguchi, and T. Y. Nakajima, 2010: Satellite data simulator unit : a multisensor, multispectral satellite simulator package. *Bull. Amer. Meteorol. Soc.*, **91**, 1625–1632.
- Matrosov, S. Y., 1992: Radar reflectivity in snowfall. *IEEE Trans. Geosci. Electron.*, **30**, 454–461.
- Matsui, T., X. Zeng, W.-K. Tao, H. Masunaga, W. S. Olson, and S. Lang, 2009: Evaluation of long-term cloud-resolving model simulations using satellite radiance observations and multifrequency satellite simulators. *J. Atmos. Oceanic Technol.*, **26**, 1261–1274.
- Milbrandt, J. A., and M. K. Yau, 2005: A multimoment bulk microphysics parameterization. Part II: A proposed three-moment closure and scheme description. *J. Atmos. Sci.*, **62**, 3065–3081.
- Milbrandt, J. A., M. K. Yau, J. Mailhot, and S. Belair, 2008: Simulation of an orographic precipitation event during IMPROVE-2. Part I: Evaluation of the control run using a triple-moment bulk microphysics scheme. *Mon. Wea. Rev.*, **136**, 3873–3893.
- Molthan, A. L., W. A. Petersen, S. W. Nesbitt, and D. Hudak, 2010: Evaluating the snow crystal size distribution and density assumptions within a single-moment microphysics scheme. *Mon. Wea. Rev.*, **138**, 4254–4267.
- Miura, H., M. Satoh, T. Nasuno, A. T. Noda, and K. Oouchi, 2007: A Madden-Julian oscillation event realistically simulated by a global cloud-resolving model. *Science*, **318**, 1763–1765.
- Morrison, H., J. A. Curry, and V. I. Khvorostyanov, 2005: A new double-moment

- microphysics parameterization for application in cloud and climate models. Part I: Description. *J. Atmos. Sci.*, **62**, 1665–1677.
- Morrison, H., G. Thompson, and V. Tatarskii, 2009: Impact of cloud microphysics on the development of trailing stratiform precipitation in a simulated squall line: Comparison of one- and two-moment schemes. *Mon. Wea. Rev.*, **137**, 991–1007.
- Nakajima, T., and M. D. King, 1990: Determination of the Optical-Thickness and Effective Particle Radius of Clouds from Reflected Solar-Radiation Measurements .1. Theory. *J. Atmos. Sci.*, **47**, 1878-1893.
- National Centers for Environmental Prediction/National Weather Service/NOAA/U.S. Department of Commerce, 2000: NCEP FNL Operational Model Global Tropospheric Analyses, continuing from July 1999. Research Data Archive at the National Center for Atmospheric Research, Computational and Information Systems Laboratory, Boulder, CO. [Available online at <http://rda.ucar.edu/datasets/ds083.2>.] Accessed 4 Jun 2011.
- Powell, S. W., R. A. Houze, A. Kumar, and S. A. McFarlane, 2012: Comparison of simulated and observed continental tropical anvil clouds and their radiative heating profiles. *J. Atmos. Sci.*, **69**, 2662-2681.
- Rao, T. N., D. N. Rao, K. Mohan, and S. Raghavan, 2001: Classification of tropical precipitating systems and associated Z-R relationships. *J. Geophys. Res.*, **106**, 17699–17711.
- Roh, W., and M. Satoh, 2014: Evaluation of Precipitating Hydrometeor Parameterizations in a Single-Moment Bulk Microphysics Scheme for Deep Convective Systems over the Tropical Central Pacific. *J. Atmos. Sci.*, **71**, 2654-2673.
- Rutledge, S. A., and P. V. Hobbs, 1984: The Mesoscale and Microscale Structure and Organization of Clouds and Precipitation in Midlatitude Cyclones .12. A Diagnostic Modeling Study of Precipitation Development in Narrow Cold-Frontal Rainbands. *J. Atmos. Sci.*, **41**, 2949-2972.
- Satoh, M., T. Matsuno, H. Tomita, H. Miura, T. Nasuno, and S. Iga, 2008: Nonhydrostatic icosahedral atmospheric model (NICAM) for global cloud resolving simulations. *J.*

- Comput. Phys.*, **227**, 3486–3514.
- Satoh, M., and Y. Matsuda, 2009: Statistics on high-cloud areas and their sensitivities to cloud microphysics using single-cloud experiments. *J. Atmos. Sci.*, **66**, 2659–2677.
- Satoh, M., T. Inoue, and H. Miura, 2010: Evaluations of cloud properties of global and local cloud system resolving models using CALIPSO and CloudSat simulators. *J. Geophys. Res.*, **115**, D00H14.
- Seiki, T., and T. Nakajima, 2014: Aerosol Effects of the Condensation Process on a Convective Cloud Simulation. *J. Atmos. Sci.*, **71**, 833-853.
- Seiki, T., M. Satoh, H. Tomita, and T. Nakajima, 2014: Simultaneous evaluation of ice cloud microphysics and nonsphericity of the cloud optical properties using hydrometeor video sonde and radiometer sonde in situ observations. *J. Geophys. Res.*, **119**, 6681-6701.
- Simpson, J., C. Kummerow, W. K. Tao, and R. F. Adler, 1996: On the tropical rainfall measuring mission (TRMM). *Meteorol Atmos Phys*, **60**, 19-36.
- Soong, S. T., 1974: Numerical-Simulation of Warm Rain Development in an Axisymmetric Cloud Model. *J. Atmos. Sci.*, **31**, 1262-1285.
- Stith, J. L., J. E. Dye, A. Bansemer, A. J. Heymsfield, C. A. Grainger, W. A. Petersen, and R. Cifelli, 2002: Microphysical observations of tropical clouds. *J. Appl. Meteorol.*, **41**, 97–117.
- Stephens, G. L., and Coauthors, 2002: The cloudsat mission and the a-train - A new dimension of space-based observations of clouds and precipitation. *Bull. Am. Meteorol. Soc.*, **83**, 1771-1790.
- Suzuki, K., T. Nakajima, T. Y. Nakajima, and A. P. Khain, 2010: A study of microphysical mechanisms for correlation patterns between droplet radius and optical thickness of warm clouds with a spectral bin microphysics cloud model. *J. Atmos. Sci.*, **67**, 1126–1141.
- Takahashi, T., 1975: Electric Charge Life-Cycle in Warm Clouds. *J. Atmos. Sci.*, **32**, 123-142.
- Tao, W. K., J. Simpson, and M. Mccumber, 1989: An ice water saturation adjustment. *Mon. Wea. Rev.*, **117**, 231–235.

- Tokay, A., and D. A. Short, 1996: Evidence from tropical raindrop spectra of the origin of rain from stratiform versus convective clouds. *J. Appl. Meteorol.*, **35**, 355–371.
- Tomita, H., and M. Satoh, 2004: A new dynamical framework of nonhydrostatic global model using the icosahedral grid. *Fluid Dynamics Research*, **34**, 357–400.
- Tomita, H., H. Miura, S. Iga, T. Nasuno, and M. Satoh, 2005: A global cloud-resolving simulation: Preliminary results from an aqua planet experiment. *Geophys Res Lett*, **32**, L08805.
- Tomita, H., 2008a: New microphysical schemes with five and six categories by diagnostic generation of cloud ice. *J. Meteorol. Soc. Jpn.*, **86**, 121–142.
- Tomita, H., 2008b: A stretched icosahedral grid by a new grid transformation. *J. Meteorol. Soc. Jpn.*, **86**, 107–119.
- Thompson, G., P. R. Field, R. M. Rasmussen, and W. D. Hall, 2008: Explicit forecasts of winter precipitation using an improved bulk microphysics scheme. Part II: Implementation of a new snow parameterization. *Mon. Wea. Rev.*, **136**, 5095–5115.
- Van Den Heever, S. C., and W. R. Cotton, 2004: The impact of hail size on simulated supercell storms. *J. Atmos. Sci.*, **61**, 1596–1609.
- Van Weverberg, K., N. P. M. van Lipzig, and L. Delobbe, 2011: The impact of size distribution assumptions in a bulk one-moment microphysics scheme on simulated surface precipitation and storm dynamics during a low-topped supercell case in Belgium. *Mon. Wea. Rev.*, **139**, 1131–1147.
- Van Weverberg, K., A. M. Vogelmann, H. Morrison, and J. A. Milbrandt, 2012: Sensitivity of idealized squall-line simulations to the level of complexity used in two-moment bulk microphysics schemes. *Mon. Wea. Rev.*, **140**, 1883–1907.
- Van Weverberg, K., and Coauthors, 2013: The role of cloud microphysics parameterization in the simulation of mesoscale convective system clouds and precipitation in the tropical western pacific. *J. Atmos. Sci.*, **70**, 1104–1128.
- Varble, A., and Coauthors, 2011: Evaluation of cloud-resolving model intercomparison simulations using TWP-ICE observations: Precipitation and cloud structure. *J. Geophys.*

Res., **116**, D12206.

- Weisman, M. L., W. C. Skamarock, and J. B. Klemp, 1997: The resolution dependence of explicitly modeled convective systems. *Mon. Wea. Rev.*, **125**, 527-548.
- Winker, D. M., J. R. Pelon, and M. P. McCormick, 2003: The CALIPSO mission: Spaceborne lidar for observation of aerosols and clouds. *Third International Asia-Pacific Environmental Remote Sensing Remote Sensing of the Atmosphere, Ocean, Environment, and Space*, International Society for Optics and Photonics, 1-11.
- Yang, P., and Coauthors, 2007: Differences between collection 4 and 5 MODIS ice cloud optical/microphysical products and their impact on radiative forcing simulations. *Ieee Trans. Geosci. Remote Sens.*, **45**, 2886-2899.
- Yoshida, R., H. Okamoto, Y. Hagihara, and H. Ishimoto, 2010: Global analysis of cloud phase and ice crystal orientation from Cloud-Aerosol Lidar and Infrared Pathfinder Satellite Observation (CALIPSO) data using attenuated backscattering and depolarization ratio. *J. Geophys. Res.*, **115**, D00H32.
- Yuan, T. L., and Z. Q. Li, 2010: General Macro- and Microphysical Properties of Deep Convective Clouds as Observed by MODIS. *J. Climate*, **23**, 3457-3473.
- Zhang, G., M. Xue, Q. Cao, and D. Dawson, 2008: Diagnosing the intercept parameter for exponential raindrop size distribution based on video disdrometer observations: Model development. *J. Appl. Meteor. Climatol.*, **47**, 2983-2992.
- Zhou, Y. P., and Coauthors, 2007: Use of high-resolution satellite observations to evaluate cloud and precipitation statistics from cloud-resolving model simulations. Part I: South China sea monsoon experiment. *J. Atmos. Sci.*, **64**, 4309-4329.